

ABSTRACT

ARNEY, DAVID HARRISON. Flux Synthesis and Photocatalytic Activities of Metal Oxides. (Under the direction of Prof. Paul A. Maggard.)

Synthesis of new metal-oxides as photocatalysts for the production of hydrogen and oxygen from water has attracted recent interest as a potential route to renewable energy. Intense research efforts have been made to utilize the largest fraction of the solar spectrum and to develop working visible-light photocatalysts for the overall splitting of water. Despite recent progress, materials parameters such as particle size and morphology, stability, cost, efficiency, and appropriate band positions need to be optimized in order to make them more commercially applicable. My research efforts within this area have focused on the flux synthesis of several photocatalytic metal-oxides as an alternative synthetic method to vary particle size and morphology and subsequently study their effects on photocatalytic properties. Metal-oxides containing d^0 transition metals were selected (Ti, Nb, Ta) which exhibited either layered or bulk perovskite structures as viable candidates for investigation. Additionally, the visible-light photocatalytic properties were studied of metals with a filled d^{10} electron configuration such as Ag^+ , and filled s^2 orbitals such as Pb^{2+} , and which create higher energy valence bands and lower the bandgap sizes of the metal-oxides. Each metal-oxide was synthesized using flux methods and varied heating and cooling times, flux-to-reactant molar ratios, and the choice of flux, in order to modulate particle sizes, shapes, and surface areas. Particle morphologies and surface areas were then characterized by scanning electron microscopy (SEM) and BET measurements, and their optical absorption edges were measured using UV-Vis diffuse reflectance spectroscopy. Their photocatalytic properties were studied under either ultraviolet or visible-light irradiation in aqueous solutions with a

deposited platinum surface cocatalyst. Platinum deposition was examined by SEM in order to probe the active surface sites of the particles, and also to gain a deeper understanding of the electron migration pathways in both layered and bulk perovskite photocatalyst particles. The rates of photocatalytic activity were strongly influenced by the formation of surface microfeatures resulting from the use of flux synthesis. Observed particle nanosteps, edges, and grooves are believed to be the primary 'active sites' for the photocatalytic reduction of water into H₂. The results of these investigations led to new insights into the understandings and origins of photocatalysis in metal-oxides, and demonstrate the utility of flux-synthesis in fine-tuning particle sizes and morphologies for optimization of photocatalytic activity.

© Copyright 2011 by David Arney

All Rights Reserved

Flux Synthesis of Photocatalytic Transition Metal Oxides

by
David Harrison Arney

A dissertation submitted to the Graduate Faculty of
North Carolina State University
in partial fulfillment of the
requirements for the degree of
Doctor of Philosophy

Chemistry

Raleigh, NC

2011

APPROVED BY:

Dr. Paul A. Maggard
Committee Chair

Dr. Mike H. Whangbo

Dr. Stefan Franzen

Dr. James D. Martin

DEDICATION

I dedicate this work to my father, William Propst Arney, who passed away on December 18th, 2010. He always believed in me and encouraged me to keep working and try my best.

BIOGRAPHY

David Harrison Arney was born on May 28th, 1982, in Des Moines, Iowa. In the spring of 2000 he graduated from the American International School of Salzburg, Austria, and enrolled in Hampden-Sydney College in Virginia the following fall. In December of 2004 he graduated with a Bachelor of Science degree in Chemistry and Physics, with a concentration in Economics. In the summer of 2005, he joined Professor Paul. A. Maggard's research group at North Carolina State University and matriculated as a graduate student in the fall, where he currently works on flux synthesis of metal oxides as potential visible-light photocatalysts.

ACKNOWLEDGMENTS

The past five years has been no easy task and could not have been possible without the assistance of my advisor, Prof. Paul A. Maggard. I appreciate all the support and the patience he has given me throughout my journey. I'd also like to thank Prof. Jim Martin for his enthusiasm, inspiration, and education in solid state chemistry. After every lecture or chat with him I always felt driven to learn more about science. Also thank you to my committee members, Prof. Mike H. Whangbo, Prof. Stefan Franzen, for their advice and input. I'd also like to thank Chuck Mooney for his assistance using the SEM facility for microscopy data.

I'd like to thank all my labmates, Lindsay, Upendra, Xiaomeng, Andriy, Olena, and former labmates, Haisheng, Phani, Bangbo, and Digamber, for making the office fun and enjoyable. Group lunches, coffees, and good friendships really made everything worthwhile. In particular, I want to thank my friend and former roommate Robert Schmidt. We had some good times getting through school together.

Finally, thanks to my wonderful family for all their love and generosity over the years. You are the foundation of support I built my life upon.

TABLE OF CONTENTS

LIST OF TABLES.....	<i>vi</i>
LIST OF FIGURES.....	<i>vii</i>
CHAPTER 1. INTRODUCTION.....	1
PART 1. UV-ACTIVE PHOTOCATALYSTS.....	23
CHAPTER 2. NEW MOLTEN-SALT SYNTHESIS AND PHOTOCATALYTIC PROPERTIES OF $\text{La}_2\text{Ti}_2\text{O}_7$ PARTICLES.....	24
CHAPTER 3. PARTICLE SIZE CONTROL AND PHOTOCATALYTIC PRODUCTION OF H_2 FROM $\text{Na}_2\text{Ca}_2\text{Nb}_4\text{O}_{13}$ CRYSTALS GROWN FROM A MOLTEN FLUX.....	52
PART 2. VISIBLE-LIGHT ACTIVE PHOTOCATALYSTS.	78
CHAPTER 4. FLUX SYNTHESIS OF AgNbO_3 : EFFECT OF PARTICLE SURFACES AND SIZES ON PHOTOCATALYTIC ACTIVITY.....	79
CHAPTER 5. EFFECTS OF PARTICLE SURFACE AREAS AND MICROSTRUCTURES ON PHOTOCATALYTIC H_2 AND O_2 PRODUCTION OVER PbTiO_3	108
CHAPTER 6. SELECT Pt DEPOSITION AND PHOTOCATALYSIS OF MLaNb_2O_7 (M=Rb,Ag) PREPARED BY FLUX SYNTHESIS AND ION-EXCHANGE.....	135
CHAPTER 7. CONCLUSIONS.....	166

LIST OF TABLES

Table 2.1	Measured photocatalytic rates of hydrogen formation for $\text{La}_2\text{Ti}_2\text{O}_7$ prepared using a $\text{Na}_2\text{SO}_4/\text{K}_2\text{SO}_4$ flux and also by the solid-state method.....	39
Table 2.S1	Refined cell parameters for $\text{La}_2\text{Ti}_2\text{O}_7$ synthesized by different Flux-prepared conditions.....	47
Table 2.S2	Measured BET surface area of $\text{La}_2\text{Ti}_2\text{O}_7$ particles in $\text{m}^2 \text{g}^{-1}$	47
Table 3.1	Measured photocatalytic rates of H_2 formation for flux-prepared $\text{Na}_2\text{Ca}_2\text{Nb}_4\text{O}_{13}$ particles deposited with a 1% wt. Pt cocatalyst by photochemical deposition (PCD) and incipient wetness impregnation (IWI) methods.....	66
Table 3.S1	Refined cell parameters for $\text{Na}_2\text{Ca}_2\text{Nb}_4\text{O}_{13}$ prepared by NaCl and Na_2SO_4 flux methods.....	75
Table 4.1	Measured BET surface areas, and visible-light ($>420 \text{ nm}$) photocatalytic rates of H_2 formation, for AgNbO_3 particles prepared using different flux conditions and also by the solid-state method.....	95
Table 4.S1	Refined unit-cell parameters for AgNbO_3 samples synthesized by the flux method.....	102
Table 5.1	Measured photocatalytic rates of O_2 and H_2 formation for flux-prepared PbTiO_3 and also by the solid state method.....	124
Table 5.S1	Refined cell parameters for PbTiO_3 , synthesized by the flux method.....	131
Table 6.1	Measured photocatalytic rates of H_2 formation for flux-prepared $\text{RbLaNb}_2\text{O}_7$ and $\text{AgLaNb}_2\text{O}_7$ under UV and visible light irradiation ($>400 \text{ nm}$).....	153
Table 6.S1	Refined cell parameters for $\text{RbLaNb}_2\text{O}_7$ and $\text{AgLaNb}_2\text{O}_7$ after ion exchange.....	163
Table 7.1	Visibly-active metal oxide photocatalysts for H_2 or O_2 evolution in the presence of sacrificial reagents under visible-light irradiation. Adapted from reference 17.....	173

LIST OF FIGURES

Figure 1.1	A representative metal oxide particle (left) shown with a schematic drawing of the overall water splitting process (right). Electrons excited into the conduction band by incident light migrate to the surface to reduce water into H ₂ , while the vacant holes oxidize water to produce O ₂	18
Figure 1.2	The relative intensity solar spectrum of incident light on the surface of the Earth during typical peak-hour daylight. Adapted from reference 14.....	19
Figure 1.3	General factors influencing fine particle characteristics during a flux-synthesis reaction. Adapted from reference 34.....	19
Figure 1.4	SEM Images of Bi ₅ Ti ₃ FeO ₁₅ at varied heating times and temperatures. (a) 900°C for 1h, and (b) 1000°C for 20h.....	20
Figure 1.5	(a) A representative surface of a particle with a stepped feature and the general activation energy barrier (E _a) as a function of distance across the surface. At the location of the step, the energy barrier is lower and therefore a preferred ‘active site’ for particle adsorption and potential photocatalysis. (b) Classic Lennard-Jones diagram showing energies of the dissociation (D _{A-A}) of a molecule relative to the distance of the proposed active site of a particle’s surface showing both strong chemisorption and weak physisorption. E _d is denoted as the desorption energy, ΔH _a is the heat of adsorption, and ΔH _p is the heat of physisorption. Adapted from reference 37.....	21
Figure 1.6	Simple band schematic drawing of a photocatalytic metal-oxide particle (left), and the reduced bandgap size with the addition of filled bands arising from Ag ⁺ d ¹⁰ (middle) and Pb ²⁺ s ² orbitals.....	22
Figure 2.1	The PXRD of the La ₂ Ti ₂ O ₇ products prepared using (a) a 10:1 flux ratio heated for 10 h, (b) a 1:1 flux ratio heated for 1 h, (c) solid-state methods (1100 °C, 50 h), and compared to (d) the calculated theoretical pattern.....	40
Figure 2.2	SEM images of washed flux products for a 2:1 molar ratio of flux:La ₂ Ti ₂ O ₇ after reaction times of (A) 1h, (B) 2h, (C) 5h, and (D) 10h. The scale is 10μm. Figure 2.3. SEM images of washed flux products for a 10:1 molar ratio of flux:La ₂ Ti ₂ O ₇	41

Figure 2.3	SEM images of washed flux products for a 10:1 molar ratio of flux:La ₂ Ti ₂ O ₇ after reaction times of (A) 1h, (B) 2h, (C) 5h, and (D) 10h. The scale is 10μm.....	42
Figure 2.4	Comparison of the SEM images of the particle morphologies obtained from a flux reaction (left; 10:1 ratio and 1h reaction time) and from a solid-state preparation (right).....	43
Figure 2.5	Plots of UV-Vis diffuse reflectance, as % reflectance versus wavelength, for (A) a 5:1 flux:La ₂ Ti ₂ O ₇ ratio reacted for (a) 1h, (b) 2h, (c) 5h and (d) 10h, and (B) for the (a) solid-state sample and the flux samples of (b) 1:1 at 1h, (c) 2:1 at 2h, (d) 5:1 at 5h, and (e) 10:1 at 10h.	44
Figure 2.6	Photocatalytic formation of hydrogen versus time for flux-synthesized La ₂ Ti ₂ O ₇ prepared in a reaction time and flux:La ₂ Ti ₂ O ₇ ratio of (a) 10h and 10:1, (b) 5h and 5:1, (c) 1h and 10:1, and (d) 2h and 5:1.....	45
Figure 2.7	TOC Caption. Photocatalytic La ₂ Ti ₂ O ₇ platelet-shaped particles, with thicknesses down to <100nm, can be prepared in a single-step molten-salt flux reaction in only 1 – 10h. The platelet particle sizes can be varied as a function of reaction conditions, e.g. flux amount and reaction time, and which are shown to result in enhanced photocatalytic activities for hydrogen formation compared to a conventional solid-state preparation.....	46
Figure 2.S1	UV-Vis diffuse reflectance measurements, plotted as % reflectance versus wavelength, for flux:La ₂ Ti ₂ O ₇ ratios of 10:1, 5:1, 2:1 and 1:1 for reaction times of 1, 2, 5, and 10 hours.....	48
Figure 2.S2	EDS Spectra of La ₂ Ti ₂ O ₇ samples prepared a) with a 2:1 flux ratio for 1h, b) 2:1 flux ratio for 10h, c) 10:1 flux ratio for 1h, and d) by the solid-state method.....	49
Figure 2.S3	Structure of layered perovskite La ₂ Ti ₂ O ₇ . TiO ₆ octahedra are shown in grey, while La ³⁺ ions fill the interstitial sites. Space group Pna2 ₁	50
Figure 2.S4	FESEM images of La ₂ Ti ₂ O ₇ taken after a 1% deposition of a platinum cocatalyst by the photodeposition method. (A and B) 1:1 flux heated for 1h, (C and D) 10:1 flux heated for 1h. (Data added August 2010)....	51
Figure 3.1	Structure of Na ₂ Ca ₂ Nb ₄ O ₁₃ . NbO ₆ octahedra are shown in blue, Ca atoms shown in green, and Na atoms in yellow. Space Group Immm....	67

Figure 3.2	PXRD Patterns of $\text{Na}_2\text{Ca}_2\text{Nb}_4\text{O}_{13}$ prepared using (a) 5:1 NaCl flux ratio, (b) 5:1 Na_2SO_4 flux ratio and (c) 20:1 Na_2SO_4 flux ratio.....	68
Figure 3.3	FESEM Images of $\text{Na}_2\text{Ca}_2\text{Nb}_4\text{O}_{13}$ aggregate rods prepared from a NaCl flux.....	69
Figure 3.4	FESEM Images of $\text{Na}_2\text{Ca}_2\text{Nb}_4\text{O}_{13}$ platelet particles prepared from a Na_2SO_4 Flux.....	70
Figure 3.5	FESEM Images of the 20:1 Na_2SO_4 flux prepared $\text{Na}_2\text{Ca}_2\text{Nb}_4\text{O}_{13}$ sample deposited with a 1% Pt Cocatalyst by the PCD method.....	71
Figure 3.6	FESEM Images of the 5:1 Na_2SO_4 flux prepared $\text{Na}_2\text{Ca}_2\text{Nb}_4\text{O}_{13}$ sample with a 1% Pt cocatalyst deposited via IWI method.....	72
Figure 3.7	UV-Vis Diffuse Reflectance Measurements for $\text{Na}_2\text{Ca}_2\text{Nb}_4\text{O}_{13}$ prepared using a (a) 5:1 NaCl Flux, (b) 5:1 Na_2SO_4 flux, (c) 20:1 Na_2SO_4 flux, and (d) 20:1 NaCl flux molar ratio.....	73
Figure 3.8	Photocatalytic formation of hydrogen versus time for flux-prepared $\text{Na}_2\text{Ca}_2\text{Nb}_4\text{O}_{13}$ using a (a) 5:1 Na_2SO_4 flux, (b) 20:1 Na_2SO_4 flux, (c) 20:1 NaCl flux, and (d) 5:1 NaCl flux. Catalyst prepared with 1% wt Pt cocatalyst deposited by the PCD method.....	74
Figure 3.S1	EDX Spectra showing the elemental composition of $\text{Na}_2\text{Ca}_2\text{Nb}_4\text{O}_{13}$ prepared using a 5:1 Na_2SO_4 flux: $\text{Na}_2\text{Ca}_2\text{Nb}_4\text{O}_{13}$ molar ratio.....	76
Figure 3.S2	EDX Spectra showing the elemental composition of $\text{Na}_2\text{Ca}_2\text{Nb}_4\text{O}_{13}$ prepared using a 20:1 NaCl flux: $\text{Na}_2\text{Ca}_2\text{Nb}_4\text{O}_{13}$ molar ratio.....	77
Figure 4.1	Structure of AgNbO_3 with the unit-cell outlined; NbO_6 octahedra are blue, Ag atoms are yellow, and O atoms are shown in red.....	96
Figure 4.2	Calculated PXRD pattern for (a) NaNbO_3 and (b) AgNbO_3 , and the experimental PXRD data for AgNbO_3 prepared using (c) solid state methods (ANO std.), (d) 1:1 flux at 10h (ANO3), and (e) 3:1 flux at 10h (ANO9).....	97
Figure 4.3	Field-emission SEM images of flux-prepared AgNbO_3 particles using (a) 1:1 flux ratio at 1h (ANO1), (b) 1:1 flux ratio at 10h (ANO3), (c) 3:1 flux ratio at 1h (ANO7), and (d) 3:1 flux ratio at 10h (ANO9).....	98
Figure 4.4	Field-emission SEM images of a AgNbO_3 sample prepared by the solid-state method at 900°C for 12h.....	99

Figure 4.5	Experimental UV-Vis DRS data for flux-prepared AgNbO_3 using (a) 2:1 flux ratio at 10h (ANO6), (b) 1:1 flux ratio at 10h (ANO3), (c) 3:1 flux ratio at 10h (ANO9), and (d) prepared using the solid-state method.....	99
Figure 4.6	High-magnification field-emission SEM images of flux-prepared AgNbO_3 particles using (a, c) 1:1 flux ratio at 10h (ANO3), (b) 1:1 flux at 1h (ANO1) showing ~20nm stepped surface features, (d) 3:1 flux ratio at 1h (ANO7), and (e, f) 2:1 flux ratio at 10h (ANO6) that shows smooth surfaces.....	100
Figure 4.7	Field-emission SEM images of post photocatalysis-tested surfaces of the solid-state prepared AgNbO_3 sample.....	101
Figure 4.S1	EDX Spectra and calculated elemental compositions of AgNbO_3 samples prepared using a (a) 1:1 flux: AgNbO_3 ratio for 1h (ANO1) and a (b) 3:1 flux: AgNbO_3 for 10h (ANO9).....	103
Figure 4.S2	FESEM images of AgNbO_3 prepared from a 1:1 Na_2SO_4 flux heated for 1h after a 1% deposition of a platinum cocatalyst by the photodeposition method. (Data added August 2010).....	104
Figure 4.S3	FESEM images of AgNbO_3 prepared from a 3:1 Na_2SO_4 flux heated for 1h after a 1% deposition of a platinum cocatalyst by the photodeposition method. (Data added August 2010).....	105
Figure 4.S4	FESEM images of AgNbO_3 prepared by traditional solid state methods after a 1% deposition of a platinum cocatalyst by the photodeposition method. (Data added August 2010).....	106
Figure 4.S5	Partial Density of States Calculation for AgNbO_3 . The Fermi level has been normalized at zero. Calculation performed with CASTEP using a GGA-PBE functional plane wave ultrasoft pseudopotential method. (Data added May 2011).....	107
Figure 5.1	The PXRD Pattern of the PbTiO_3 products. (a) Calculated theoretical PbTiO_3 pattern, (b) solid state method (c) 1:1 NaCl Flux heated for 1 h, (d) 10:1 NaCl flux heated for 1 h, (e) 2:1 PbO flux heated for 1 h.....	125
Figure 5.2	UV-Vis Diffuse Reflectance Spectra of PbTiO_3 powders prepared via (a) Solid-State Methods, (b) 1:1 NaCl (PBO1), (c) 0.5:1 PbO (PBO4), (d) 1:1 PbO (PBO5), (e) 20:1 NaCl (PBO3), and (f) 10:1 NaCl (PBO2). Reflectance has been converted to absorbance by the Kubelka-Munk method.....	126

Figure 5.3	FESEM Images of (a,b) PBO1 and (c,d) PBO2 prepared at 1000°C for 1h using a NaCl molten flux in flux:PbTiO ₃ ratios of (a,b) 1:1 and (c,d) 10:1.....	127
Figure 5.4	FESEM Images of PBO6 prepared at 1000°C for 1h in a PbO molten flux with a flux:PbTiO ₃ molar ratio of 2:1.....	128
Figure 5.5	FESEM Images of the solid-state PbTiO ₃ prepared at 1000°C for 48h...	128
Figure 5.6	FESEM Images of PBO3 prepared in a 20:1 NaCl flux showing (a and b) bare particles before platinum photodeposition and (c and d) with a 1% wt. Pt photodeposited cocatalyst.....	129
Figure 5.7	FESEM Images of platinized PbTiO ₃ prepared (a) using a 1:1 NaCl Flux (PBO1) and (b) by traditional solid state methods (PBO std.).....	130
Figure 5.S1	EDX Spectra showing the elemental composition of PbTiO ₃ prepared using (a) solid state methods (PBO std.) and (b) 10:1 NaCl flux (PBO2).....	132
Figure 5.S2	Structure of PbTiO ₃ , classic perovskite. TiO ₆ octahedra are shaded in yellow, while Pb ²⁺ ions fill the interstitial sites.....	134
Figure 6.1	Structure of AgLaNb ₂ O ₇ with outlined unit cell. NbO ₆ octahedra are colored in yellow, La atoms are gold colored, and Ag atoms are green colored. Space Group I4 ₁ /acd.....	154
Figure 6.2	The powder X-ray diffraction (PXRD) patterns of the AgLaNb ₂ O ₇ products. (a) calculated theoretical AgLaNb ₂ O ₇ pattern, and AgLaNb ₂ O ₇ patterns prepared from (b) solid state methods, (c) 1:1 RbCl flux heated for 6h, (d) 1:1 RbCl flux heated for 24h, (e) 10:1 RbCl Flux heated for 1h. Inset shows calculated RbLaNb ₂ O ₇ patterns (1a) along with each corresponding prepared RbLaNb ₂ O ₇ pattern (b) solid state methods, (c) 1:1 RbCl flux heated for 6h, (d) 1:1 RbCl flux heated for 24h, (e) 10:1 RbCl flux heated for 24h.....	155
Figure 6.3	FESEM Images of (a) RbLaNb ₂ O ₇ prepared from solid state methods and (b) AgLaNb ₂ O ₇ after ion-exchange, and (c) RbLaNb ₂ O ₇ prepared with a 1:1 RbCl flux and (d) AgLaNb ₂ O ₇ after exchange (d).....	156
Figure 6.4	FESEM Images of (a and b) RbLaNb ₂ O ₇ prepared using a 10:1 RbCl flux and (c and d) AgLaNb ₂ O ₇ after the ion-exchange reaction.....	157

Figure 6.5	SEM Image and EDX spectra (Inset) showing elemental composition of platinum island (Spectrum 1) and bare $\text{RbLaNb}_2\text{O}_7$ surface (Spectrum 2).....	158
Figure 6.6	FESEM Images of a 5% wt. platinum photodeposition on the surface of flux-prepared $\text{RbLaNb}_2\text{O}_7$	159
Figure 6.7	FESEM Images of a 5% wt. platinum photodeposition on the surface of flux-prepared $\text{AgLaNb}_2\text{O}_7$	160
Figure 6.8	UV-Vis Diffuse Reflectance Spectra of (a) $\text{RbLaNb}_2\text{O}_7$ and (b) $\text{AgLaNb}_2\text{O}_7$ after the ion-exchange reaction. Reflectance has been converted to absorbance by the Kubelka-Munk method.....	161
Figure 6.9	Photocatalytic formation of hydrogen versus time for $\text{AgLaNb}_2\text{O}_7$ prepared by (a) solid state methods, (b) 5:1 RbCl flux heated for 6h, (c) 1:1 RbCl flux heated for 24h, (d) 5:1 RbCl flux heated for 24h, (e) 1:1 RbCl flux heated for 6h.....	162
Figure 6.S1	EDX Spectra showing the elemental composition of flux-prepared $\text{RbLaNb}_2\text{O}_7$	164
Figure 6.S2	EDX Spectra showing the elemental composition of flux-prepared $\text{AgLaNb}_2\text{O}_7$	165

CHAPTER 1

INTRODUCTION

Photocatalytic hydrogen production from solar energy and water using metal-oxide particles is an attractive and growing field of renewable energy research.¹⁻⁴ The long-term global energy demand is estimated to grow from 14TW (globally) to 20TW by the year 2050, and therefore a deeper understanding of how to achieve more efficient and cheaper routes to the utilization of sunlight will be critical to better harnessing this energy source and meet growing demands.⁵ Further, this approach would provide a clean and sustainable alternative to the combustion of fossil fuels such as crude oil, estimated to be within 50-150 years of depletion, and which produces environmentally-harmful greenhouse gases such as CO and CO₂.⁶ Heterogeneous catalysis has allowed for some of the most crucial processes in modern history. A few examples include the catalytic converter in automobiles to reduce air pollution, and the use of solid Fe catalysts in the Haber-Bosch process to produce ammonia.⁷ Metal-oxides are quite abundant in nature, cost effective, and contain a wide range of compositions and structures that enable numerous chemical and physical properties.⁸⁻¹⁰ Several metal-oxides are being studied for their photocatalytic behavior. A photocatalytic reaction for the production of hydrogen from water was first discovered by Fujishima and Honda in 1972, when they showed water could be split into hydrogen and oxygen by an *n*-

doped TiO₂ photoelectrode under ultraviolet irradiation.¹¹ Since that time, more than a hundred different metal oxides have been studied for their photocatalytic reactivity, and which have all been generally found to proceed by a common mechanism, which is as follows: Valence band electrons are excited to the conduction band by incident photons of light, the created electron-hole pairs are then separated by the band bending at the surface-electrolyte interface, where the electron is at a high enough potential to reduce water at the surface to form hydrogen, while the vacant hole in the valence band is at a low enough potential to oxidize water at the surface to produce oxygen, as shown in Figure 1.1.¹²⁻¹⁴ In principle, this reaction can be driven by light with a wavelength <1,008nm (i.e., >1.23eV for H₂O + 2hν → H₂ + ½O₂), which means the potentially useable region of the solar spectrum extends out into the near-IR wavelengths (see Figure 1.2), although typically these low-bandgap semiconductors will require a bias voltage or external redox agent to assist in the reaction.¹⁵

Numerous metal-oxides have been shown to efficiently photo-catalyze the conversion of water into hydrogen and oxygen under high-energy ultraviolet wavelengths, including NaTaO₃¹⁶, Sr₂Nb₂O₇^{17,18}, La₂Ti₂O₇¹⁹, as well as many others.²⁰⁻²⁷ These studies have predominantly utilized high-temperature solid-state synthetic techniques to prepare the metal-oxide solids, *but this method provides almost no control over the surface characteristics of the metal oxide particles where the photon-initiated oxidation and reduction reactions occur* (i.e., the critical sites of the electron transfer). Utilization of new synthetic routes to better gain control over the surface structures of the metal oxides could enable a new and deeper understanding of these reactions. An additional difficulty is that

these metal-oxides are nearly always characterized by large optical bandgap sizes ($>3.0\text{eV}$), where the required valence-to-conduction band electronic transition can only take place at ultraviolet and higher energies, which encompasses only a minor portion of the solar spectrum. Thus, two primary and critical directions in this area are: **a) new investigations of flux synthetic techniques to provide a greater level of control over the particle sizes, surfaces, and morphologies of photocatalytic metal-oxide solids, and, b) the exploration and testing of new band-energy strategies for attaining valence-to-conduction band transitions at visible-light wavelengths using a combination of transition metals with d^0 and d^{10} electron configurations**, and are therefore suitable for use with the predominant region of the solar spectrum.

The flux synthetic method is a molten-salt assisted solid state reaction that is known to shorten reaction times, reduce reaction temperatures, and to give selective control over particle features, such as size and morphology, as compared to metal oxides prepared by conventional solid-state techniques.²⁸⁻³³ The use of a flux during synthesis has also given researchers access to many metal oxides that cannot be prepared or are difficult to synthesize in pure form by traditional methods.³⁴ Prior to the reaction, the precursor metal-oxide components are diluted within a salt or a mixture of salts (usually combined at a eutectic point), such as alkali-metal halides, sulfates, carbonates, or nitrates. When the mixture is heated to above its melting point, the increased solubility of the metal-oxides can result in rapid diffusion and product formation in much shortened reaction times.³⁰ The choice of salt, the stoichiometric mixture and solubility of precursor components in the molten salt, the melting point of the salt, heating temperature, and reaction time are all controllable factors

that influence the size, shape, crystallinity, and growth of the desired oxide compound.³⁵ The choice of flux is typically based upon cost, melting point, ease of removal and that it does not undesirably react with the precursor mix. For example, in the case of $\text{Pb}(\text{Mg}_{1/3}\text{Nb}_{2/3})\text{O}_3$, a well-known lead-based relaxor, several flux reaction parameters, as shown in Figure 1.3, that influenced the speed of reaction were found to be temperature, solubility, melting point, and eutectic mixtures, whereas particle size was more largely affected by temperature, heating time, amount of flux used, and choice of flux.³⁶ In another example of $\text{K}_{0.8}\text{Li}_{0.266}\text{Ti}_{1.734}\text{O}_4$, a lamellar UV-shielding inorganic material, a K_2MoO_4 flux was used to achieve particle sizes between 5-50 μm in diameter to give a maximal shielding effect for human skin.³² However, *despite these significant advantages, flux synthetic methods had never previously been utilized to achieve more suitable preparations of metal-oxides for use as photocatalysts for hydrogen production.*

My research has built from previous work in the Maggard group that has focused on the flux synthesis of layered perovskite and 3D perovskite metal oxides containing two or more transition metals. Previous studies on the control over particle size were demonstrated via the use of a molten-salt flux during the syntheses of layered Aurivillius phases $\text{Bi}_5\text{Ti}_3\text{FeO}_{15}$ and $\text{LaBi}_4\text{Ti}_3\text{FeO}_{15}$, which are known ferroelectric materials with applications in electronic information storage devices.³⁷ Highly-textured platelet-like particle sizes that can be controlled from $< 1 \mu\text{m}$ to $> 20\mu\text{m}$, were obtained in only 0.5 – 1 h at 800 or 900 $^\circ\text{C}$, as shown in Figure 1.4. Factors such as surface area, composition, morphology and microstructure are all important to improve catalytic efficiency. Atoms at the surface of the particle are free to bond and interact with nearby molecules. Metal-oxide surfaces that have

unusual microfeatures such as nanosteps, defects, edges, kinks, and grooves can influence the rate of reaction by exposing certain ‘active sites’ that can improve one or more steps of the catalytic process.³⁸⁻⁴⁰ Figure 1.5 illustrates such an event, in which a layered step on the surface of a solid catalyst can have a lower energy of activation barrier and therefore an increased rate of catalysis. Factors such as local electronic structure, coordination environment, and geometrical considerations all contribute to the adsorption of a molecule and surface catalytic activity.⁴¹ By gaining greater control over particle morphology through the use of flux synthesis, surface features that help to improve overall photocatalytic activity can be accessed more easily. Photocatalysis studies on metal oxides have demonstrated that particle sizes and morphologies can play a critical role in their rates of H₂ production, such as demonstrated for the flux synthesis of La-doped NaTaO₃. The preparation of La-doped NaTaO₃ using a 1:1 Flux-to-Sample ratio heated to 900°C for 1h produced particles with a varied morphology and fine surface structure and showed that the photocatalytic activity is enhanced by two-fold compared to La-doped NaTaO₃ prepared by the conventional solid-state method, whose structure was found to be more rigid and not well-defined.⁴²

The surface of the metal-oxide photocatalyst is very important in heterogeneous catalysis, and measuring the surface area is typically one of the first experimental steps explored in the laboratory after synthesis. This can be found by using the BET method of surface area analysis. Derived in 1938 by Stephen Brunauer, Paul Emmett, and Edward Teller, the physical adsorption of a monolayer onto the surface of a particle can be expressed by equation 1.1

$$\frac{P}{V(P_o - P)} = \frac{1}{V_m \times C} + \frac{(C-1)}{V_m \times C} \times \frac{P}{P_o} \quad (1.1)$$

where P and P_o are the equilibrium and saturation pressures of adsorbates at the temperature of adsorption, V is the volumetric uptake of gas (usually N_2), V_m is the volume of gas required to cover one monolayer thickness on the surface, and C is the BET constant. The most commonly observed adsorption isotherm is type I, in which the adsorption of the gas monolayer reaches a saturation limit. The total surface area of the metal oxide is then given by equation 1.2

$$SA_{BET} = \frac{V_m \times N \times s}{V} \quad (1.2)$$

where N is avagadro's number, and s is the cross-sectional surface area of the adsorbed gas. The specific area can then be found by dividing the total surface area by the weight of catalyst used in the experiment.⁴³ The discussed metal-oxides in the following chapters exhibited a type I adsorption isotherm.

Few metal-oxide photocatalysts are reported that absorb visible-light radiation and result in the photon-driven reduction of water to hydrogen, such as α - Fe_2O_3 and $In_{1-x}Ni_xTaO_4$, and further, they typically exhibit incident photon-to-hydrogen efficiencies of only ~1-2%.^{44,45} By comparison, of the numerous (>100) reported metal-oxide photocatalysts that are active under ultraviolet light, many of them exhibit very high efficiencies (in the range of 20% to greater than 50%) for the production of hydrogen in water. Because visible-light wavelengths are approximately >50% of the total sunlight striking Earth, it is highly desirable and necessary to extend the efficient photocatalysis range of metal oxides. The electronic band structure of the known UV-active metal oxide photocatalysts such as TiO_2 and $NaTaO_3$, consist of a conduction band derived from the metal d^0 orbitals, the lowest energy of which in an octahedral coordination environment are t_{2g} -based bands, that is

positioned sufficiently higher than the reduction potential of H₂O.^{1,46-48} The valence band stems primarily from the O p-orbitals and is commonly located ~1.5-2.0eV below the oxidation potential of H₂O (-1.23 eV). Thus, the potential of the two bands is such that photo-excited electron/hole carriers may reduce and oxidize water into H₂ and O₂, respectively, but only under UV irradiation because of the large size of the bandgap. Since the minimum potential difference necessary between the two bands is 1.23 eV for these two half reactions, the bandgap size of an oxide can in principle be this small and still drive the overall water splitting reaction. Therefore, we have been exploring the new flux synthesis of materials that contain an ~0.5-1.5eV higher energy valence band which can be attained from the addition of late transition metals with filled d¹⁰ orbitals, and therefore can function as a higher energy donor level for excitation to the conduction band. Previous studies on Ag⁺ and Pb²⁺ (i.e., with d¹⁰ and s² electron configurations, respectively) containing metal oxides such as AgTaO₃, AgNbO₃, and PbTiO₃ have shown ~0.5-1.0eV lowered bandgap sizes compared to their alkali metal analogues (e.g., NaTaO₃, NaNbO₃), but typically low visible-light photocatalytic activity.⁴⁹⁻⁵¹ However, these studies have been limited to the solid-state preparation of these few known examples. More recently, research in our group has also extended to the studies of Ag⁺ and Cu⁺-containing heterometallic-oxide/organic hybrids prepared by hydrothermal synthesis with promising visible-light absorption properties, but the photon-driven reactivities of these compounds have been limited mainly to photodecomposition of organic dye materials.⁵²⁻⁵⁵ Many layered oxides such as the two-perovskite-layer Dion-Jacobson (DJ) ALaM₂O₇ (A = alkali metal, M = Nb, Ta) family, the three-perovskite-layer Ruddlesden-Popper (RP) A₂La₂Ti₃O₁₀, (A = alkali metal) family, and

single-perovskite-layer RP NaLaTiO₄ phase, contain interlayer alkali metal cations that can be exchanged with transition metals, and are also UV-active photocatalysts.^{25,56-59} The exchange of filled orbitals, such as those of Ag⁺ or Pb²⁺, between the perovskite layers could serve to add a new donor level band in the electronic structure, shown in Figure 1.6, at approximately 0.5eV and 1.0 eV above the O p-orbital based valence band, respectively. Thus, the exploration of new compositional transformations of existing UV-active photocatalysts (i.e. specifically, the insertion of Ag⁺ and Pb²⁺), will enable access to a greater range of new metal oxides with reduced visible-light bandgap sizes that could potentially lead to efficient photocatalysts for the production of hydrogen.

Recently, the Maggard research group has reported on the rapid flux-assisted visible-light sensitization of several layered-perovskite metal oxides in the ALaM₂O₇ (A = alkali metal, M = Nb, Ta) and A₂La₂Ti₃O₁₀ families, that is accomplished via the exchange of the interlayer alkali metal cations for copper-halide layers.^{56,60,25,57} My research has involved the development of the first known flux syntheses of these parent layered metal-oxide phases, in order to obtain a concomitant control over not only the particle sizes and morphologies, but as well, the optical bandgap sizes of these solid metal-oxide particles. Thus, my research efforts also extend to the subsequent ion-exchange reactions of the flux-prepared layered metal-oxides, in order to tune their optical bandgap sizes towards the visible wavelengths.

The major research efforts of my work described in this document involve new flux syntheses of metal-oxide photocatalytic materials in order to maintain particle size and shape control towards optimization of photocatalytic H₂ and O₂ production from water under both UV and visible-light irradiation. The effects of reaction conditions such as flux amount, flux

choice, reaction time, reaction temperature and cooling rates are varied and studied, as well as the effects from platinum cocatalyst deposition, photocatalysis reaction temperature, solvent, pH, and wavelength and intensity of the incident light. This work then extends further into the rational design, flux syntheses, and optimization techniques of visible-light-absorbing photocatalysts from existing UV-active layered materials. Through the characterizations and optical property studies, we seek to provide a deeper understanding of the origins of photocatalysis in metal-oxide particles

Experimental Techniques

Molten-Salt Flux Synthesis. Stoichiometric mixtures of desired analytical grade reagents were combined in a mortar and pestle and mixed well for 30 min prior to the addition of the desired flux material and usually ~10mL of acetone to aid in the mixing process. After complete evaporation of the acetone, the reactants are placed in alumina crucibles and heated in Lindberg Blue box furnaces in open air. Heating times and molar ratios are given in each chapter. The flux material was typically removed with hot deionized water and then the sample was dried at 80°C overnight in an oven. More details are provided within each chapter.

Powder X-ray Diffraction. High-resolution Powder X-ray Diffraction (PXRD) patterns of all products were collected on an INEL diffractometer using $\text{CuK}\alpha_1$ ($\lambda=1.54056$ Å) radiation from a sealed-tube X-ray generator (35kV, 30mA) using a curved position sensitive detector (CPS120). The sample was placed in a rotating chamber located between the direct beam of the incident X-rays and the detector. Powder X-ray diffraction patterns

were analyzed using the Winplotr program and analyzed with reference to theoreticalcalculated patterns contained in the Crystal Structure Database (ICSD) and the Powder Diffraction File (PDF). Profile fitting using either FullProf, GSAS/EXPGUI, or LATCON programs was also used as a check of the lattice parameters.⁶¹⁻⁶⁴

UV-Vis Diffuse Reflectance. UV-Vis Diffuse Reflectance Spectra (DRS) were collected on powdered samples using either a CARY 3E spectrophotometer or Shimadzu UV-3600 UV-Vis-NIR spectrophotometer equipped with an integrating sphere. Approximately 50mg of sample was mounted to a fused-silica holder and placed along the external window. Pressed BaSO₄ plates were used as a reference and the data were plotted as the remission function $F(R_{\infty}) = (1 - R_{\infty})^2 / (2 R_{\infty})$, where R_{∞} is the diffuse reflectance based on the Kubelka-Monk theory of diffuse reflectance.⁶⁵ The bandgap (E_g) was estimated using the formula E_g (eV) = 1240/ λ_g (nm), where λ_g is extrapolated from the linear rise in the absorption curve. Smaller particle sizes will exhibit higher diffuse reflectance at sub-bandgap wavelengths (i.e. usually >400nm) compared to larger particle sizes. Thus, particle sizes can be qualitatively estimated by comparing the diffuse reflectance of similar samples.^{66,67}

Scanning Electron Microscopy. Scanning electron microscopy (SEM) was performed using a JEOL SEM 6400 in order to examine the range of particle microstructures and approximate sizes and size distributions. Samples were observed either bare or sputter-coated with colloidal gold of ~45 nm in thickness to enhance conductivity and to prevent surface charging. Digital images of samples were typically taken at a range of magnifications to study both single particles as well as larger aggregate formations of particles. Concomitantly, the energy dispersive X-ray (EDX) spectra were also taken of the samples as a check of elemental composition.

BET Surface Area Analysis. Surface area measurements were collected using a Quantachrome ChemBET Pulsar TPR/TPD. Samples were preheated and outgassed for typically 2-3 h under Nitrogen flow and then analyzed using a 30% He/N gas mixture and liquid nitrogen cooling Dewar.

Photocatalysis Testing. The photocatalytic activity (for H₂ formation) of each metal-oxide product was measured under greater-than-bandgap illumination in aqueous solutions. For each sample, both the bare metal-oxide particles as well as Pt-loaded particles were tested. Numerous previous studies have shown that platinum islands on a metal oxide surface can function as an aid to the reduction of H₂O at the surfaces to give H₂.⁶⁸ While for some samples a range of surface wt% Pt was investigated, most commonly each was loaded at 1 wt% Pt cocatalyst using a reported photodeposition method¹⁶. First, typically 100mg of a metal oxide sample was mixed with 30mL of an aqueous solution of dihydrogen hexachloroplatinate(IV) (H₂PtCl₆·6H₂O; Alfa Aesar, 99.95%), and that was then irradiated using a 400W Xe arc-lamp with constant stirring using a magnetic stir bar for 2h. After platinization, the particles were separated via centrifugation, washed with distilled water to remove any remaining Cl⁻ ions, and then dried in an oven at 80°C. For photocatalytic measurements, a weighed (100mg) amount of the platinized sample was added to a ~90mL quartz reaction vessel that was then filled with water. In the event that only a low activity for H₂ formation was obtained, the experiment was repeated in a 20% aqueous methanol solution, which typically enhanced the rate. The added methanol functions as a hole scavenger, thereby generating CO₂ from photo-oxidation, and which allows the measurement of the formation rate of H₂ alone and without the typically more difficult concomitant

formation of O₂ being necessary and rate limiting.⁴ For the photocatalytic reactions containing methanol, the net balanced reaction is: CH₃OH + H₂O → 3 H₂ + CO₂. In some cases, the O₂ production was studied using an aqueous AgNO₃ solution and with a RuO₂ or Pt cocatalyst deposited via incipient wetness impregnation and is described in more detail in those chapters.

The metal-oxide particles were stirred in the dark for ~ 1 – 2 h to remove any trapped gases on the particles' surfaces. Next, this quartz reaction cell was irradiated under constant stirring using an external 1000W Xe arc-lamp equipped with an IR water filter and cooled using an external fan. The photoreaction vessel was connected to a small horizontal quartz tube that trapped the evolved gases, and contained a moveable liquid bubble that allowed a volumetric determination of the amount of evolved gases at a constant pressure. The most active photocatalytic metal-oxides exhibited the formation of copious amounts of gases that rose to the top of the reaction cell, and that was observed to be consistent with the movement of the liquid bubble. The progress of the photocatalytic reactions was marked every hour and used to calculate the amount of gases generated in μmol g⁻¹ h⁻¹. The trapped gases were manually injected into a gas chromatograph (SRI MG #2, helium ionization and thermal conductivity detectors) in order to identify the formed gases as H₂ and CO₂, and to confirm a constant molar ratio over time.

Dissertation Organization

This dissertation has been organized in the form of papers either formerly published or in a potentially publishable format. They are divided into two major sections, those being UV-active photocatalysts (Chapters 2-3) and visibly-active photocatalysts (Chapters 4-6).

The results of Chapters 2, 4, and 5 have been published with the citation listed at the beginning of each chapter, while chapters 3 and 6 are written in a potentially publishable format or have been recently submitted for publication.

References

- (1) Domen, K. *Bull. Chem. Soc. Japan* **2000**, 73, 1307.
- (2) Domen, K. *Korean J. of Chem. Eng.* **2001**, 18, 862.
- (3) Kato, H. *Catalysis today* **2003**, 78, 561.
- (4) Graetzel, M. E. *Energy Resources through Photochemistry and Catalysis*; Academic Press: New York, NY, 1983.
- (5) Cai, Z.; Xing, X.; Yu, R.; Sun, X.; Liu, G. *Inorg Chem* **2007**, 46, 7423.
- (6) Lewis, N. S.; Nocera, D. G. *Proceedings of the National Academy of Sciences* **2006**, 103, 15729.
- (7) Smil, V. *Nature* **1999**, 400, 415.
- (8) Brown, T. L., LeMay, H.E., Jr., Bursten, B.E. *Chemistry, The Central Science*; 8th ed.; Prentice Hall: Upper Saddle River, NJ 2000.
- (9) Cox, P. A. *Transition Metal Oxide: An Introduction to Their Electronic Structure and Properties.*; Clarendon Press: Oxford, 1992.
- (10) Grimes, C. A., Varghese, O.K., Ranjan, S. *Light, water, hydrogen: the solar generation of hydrogen by water photoelectrolysis*; Springer: New York, 2008.
- (11) Fujishima, A. *Nature* **1972**, 238, 37.
- (12) Tonkiewicz, M.; Fay, H. *Appl. Phys.* **1979**, 18, 1.
- (13) Xu, Y.; Schoonen, M. *The American mineralogist* **2000**, 85, 543.
- (14) Gratzel, M. *Nature* **2001**, 414, 338.
- (15) Osterloh, F. E. *Chem. Mater.* **2008**, 20, 35.
- (16) Kato, H.; Asakura, K.; Kudo, A. *J. Am. Chem. Soc.* **2003**, 125, 3082.

- (17) Hyun G. Kim, D. W. H., et. al *Chem. Comm.* **1999**, *12*, 1077.
- (18) Kudo, A. *J. Phys. Chem. B* **2000**, *104*, 571.
- (19) Kim, G. H. *Catal. Lett.* **2003**, *91*, 193.
- (20) Kudo, A.; Nakagawa, S.; Kato, H. *Chem. Lett.* **1999**, *11*, 1197.
- (21) Abe, R.; Higashi, M.; Sayama, K.; Abe, Y.; Sugihara, H. *J. Phys. Chem. B* **2006**, *110*, 2219.
- (22) Kutty, T. R. N.; Avudaithai, M. *Catal. Rev.* **1992**, *34*, 373
- (23) Machida, M.; Yabunaka, J.-i.; Kijima, T. *Chem. Comm.* **1999**, *19*, 1939.
- (24) Machida, M., et. al *J. Mater. Chem.* **2003**, *13*, 1433.
- (25) Takata, T. *J. Photochem. Photobiol. A, Chem.* **1997**, *106*, 45.
- (26) Domen, K. *Catal. Lett.* **1990**, *4*, 339.
- (27) Shimizu, K.-i.; Tsuji, Y.; Hatamachi, T.; Toda, K.; Kodama, T.; Sato, M.; Kitayama, Y. *Phys. Chem. Chem. Phys* **2004**, *6*, 1064
- (28) Chiu, C.; Li, C.; Desu, S. B. *J. Am. Ceram. Soc.* **1991**, *74*, 38.
- (29) Arendt, R. H. *J. Solid State Chem.* **1973**, *8*, 339.
- (30) Arendt, R. H.; Rosolowski, J. H.; Szymaszek, J. W. *Mater. Res. Bull.* **1979**, *14*, 703.
- (31) Hedden, D. B. *J. Solid State Chem.* **1995**, *118*, 419.
- (32) El-Toni, M. A. *Mater. Lett.* **2006**, *60*, 185.
- (33) Kan, Y. *Cryst. Eng.* **2003**, *38*, 567.
- (34) Kato, H., Akihiko Kudo. *Chem. Lett.* **1999**, *11*, 1207.
- (35) Mao, Y., et. al *Small* **2007**, *3*, 1122.

- (36) Yoon, K. H., Cho, Y. S., Dong, H. K. *J. Mater. Sci.* **1998**, *33*, 2977.
- (37) Porob, D. G.; Maggard, P. A. *Mater. Res. Bull.* **2006**, *41*, 1513.
- (38) Bowker, M. *The Basis and Applications of Heterogeneous Catalysis*; Oxford University Press: New York, NY, 1998.
- (39) Taylor, H. S. *Proc. R. Soc. London, Ser. A* **1925**, *108*.
- (40) Ertl, G. *Reactions at Solid Surfaces*; Wiley & Sons: Hoboken, NJ, 2009.
- (41) Norskov, J. K., et. al *Chem. Soc. Rev.* **2008**, *37*, 2163.
- (42) Porob, D. G.; Maggard, P. A. *J. Solid State Chem.* **2006**, *179*, 1727.
- (43) Brunauer, S.; Emmett, P. H.; Teller, E. *J. Am. Chem. Soc.* **1938**, *60*, 309.
- (44) Kiwi, J.; Graetzel, M. *J. Chem. Soc., Faraday Trans. 1* **1987**, *83*, 1101.
- (45) Zou, Z.; Ye, J.; Arakawa, H. *Catal. Lett.* **2001**, *75*, 209.
- (46) Matsumoto, Y. *J. Solid State Chem.* **1996**, *126*, 227.
- (47) Xu, Y. *The American Mineralogist* **2000**, *85*, 543.
- (48) Kato, H. *Catal. Lett.* **1999**, *58*, 153.
- (49) Kato, H.; Kobayashi, H.; Kudo, A. *J. Phys. Chem. B* **2002**, *106*, 12441.
- (50) Kim, H. G.; Becker, O. S.; Jang, J. S.; Ji, S. M.; Borse, P. H.; Lee, J. S. *J. Solid State Chem.* **2006**, *179*, 1214.
- (51) Kim, H. G.; Hwang, D. W.; Lee, J. S. *J. Am. Chem. Soc.* **2004**, *126*, 8912.
- (52) Lin, H.; Maggard, P. A. *Inorg Chem* **2008**, *47*, 8044.
- (53) Lin, H.; Maggard, P. A. *Inorg. Chem.* **2007**, *46*, 1283.
- (54) Lin, H.; Maggard, P. A. *Cryst. Growth Des.* **2010**, *10*, 1323.
- (55) Lin, H.; Wu, X.; Maggard, P. A. *Inorg Chem* **2009**, *48*, 11265.

- (56) Gopalakrishnan, J.; Bhat, V.; Raveau, B. *Mater. Res. Bull.* **1987**, *22*, 413.
- (57) Toda, K., et. al *J. Mater. Chem.* **1996**, *6*, 1067.
- (58) Viciu, L. *Cryst. Eng.* **2004**, *39*, 2147.
- (59) Toda, K. *Solid State Ionics* **1995**, *81*, 267.
- (60) Porob, D. G.; Maggard, P. A. *Chem. Mater.* **2007**, *19*, 970.
- (61) Rodríguez-Carvajal, J.; Roisnel, T.; Commission For Powder Diffraction, International Union for Crystallography: Rennes, France, 2004.
- (62) Schwarzenbach, D. *Acta Cryst., Sect. A: Found. Crystallogr.* **1989**, *A45*, 63.
- (63) Toby, B. H. *J. Appl. Crystallogr.* **2001**, *34*, 210.
- (64) A.C. Larson, R. B. V. D. *General Structure Analysis System (GSAS)*, Los Alamos National Laboratory, 2000.
- (65) Kubelka, P. *J. Opt. Soc. Am.* **1948**, *38*.
- (66) Lagorio, G. M. *J. Chem. Ed.* **2004**, *81*, 1607.
- (67) Christy, A. A.; Liang, Y.-Z.; Hui, C.; Kvalheim, O. M.; Velapoldi, R. A. *Vib. Spec.* **1993**, *5*, 233.
- (68) Nakamatsu, H. *J. Chem. Soc., Faraday Trans. 1* **1985**, *82*, 527.

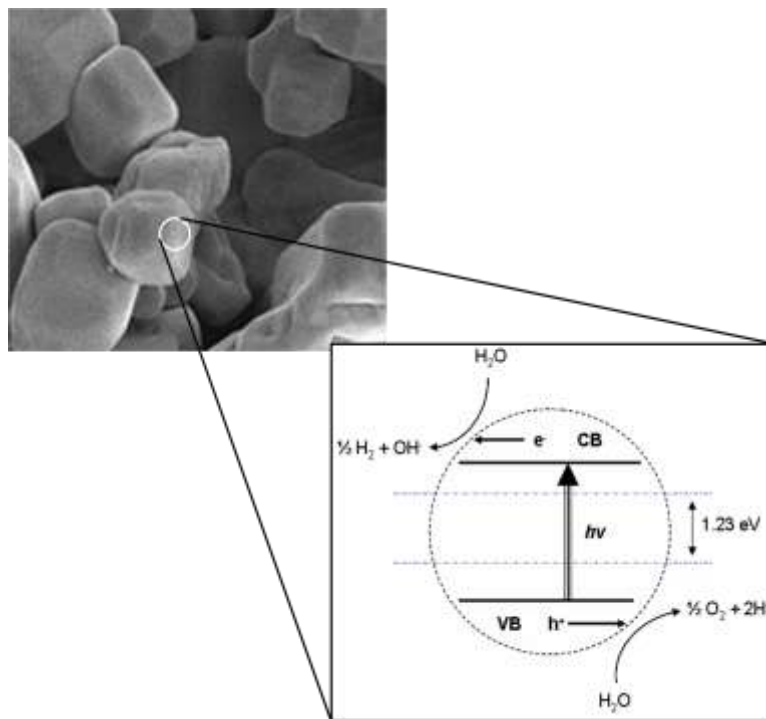


Figure 1.1. A representative metal oxide particle (left) shown with a schematic drawing of the overall water splitting process (right). Electrons excited into the conduction band by incident light migrate to the surface to reduce water into H_2 , while the vacant holes oxidize water to produce O_2 .

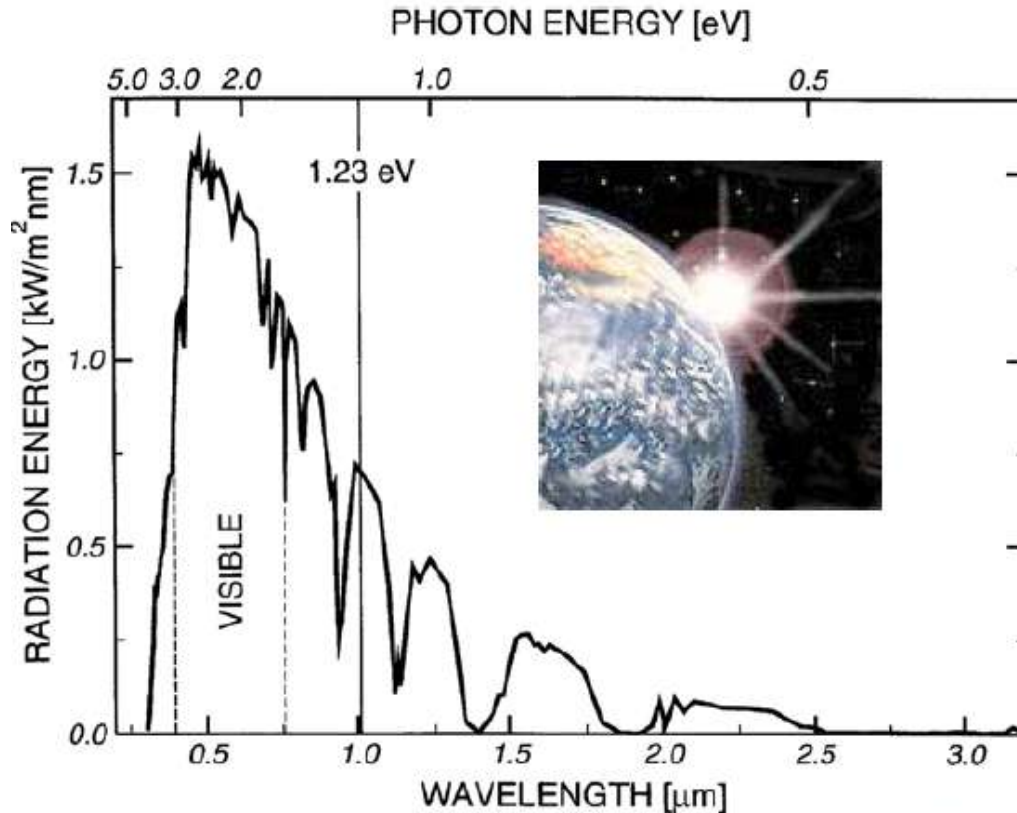


Figure 1.2. The relative intensity solar spectrum of incident light on the surface of the Earth during typical peak-hour daylight. Adapted from reference 14.

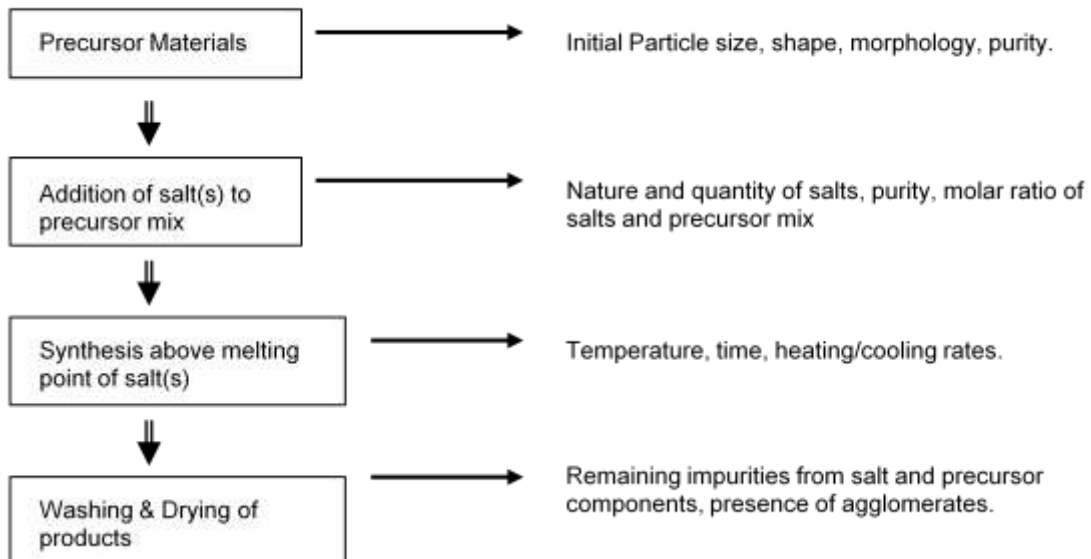


Figure 1.3. General factors influencing fine particle characteristics during a flux-synthesis reaction. Adapted from reference 34.

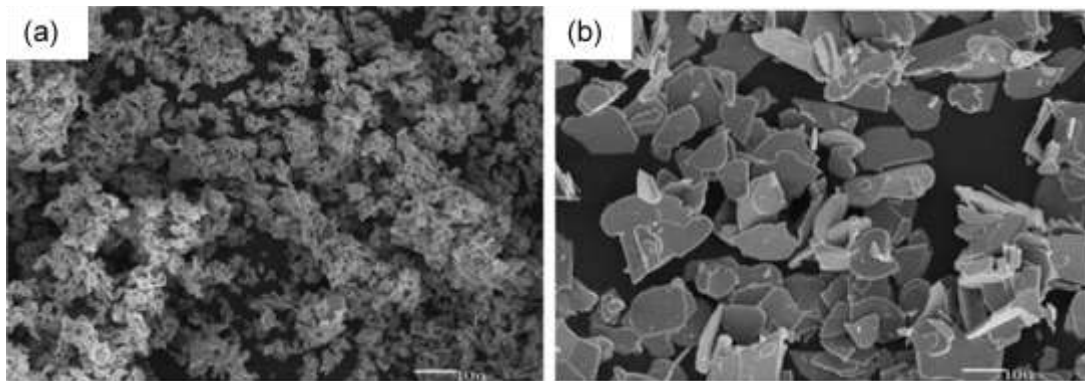


Figure 1.4. SEM Images of $\text{Bi}_5\text{Ti}_3\text{FeO}_{15}$ at varied heating times and temperatures. (a) 900°C for 1h, and (b) 1000°C for 20h.

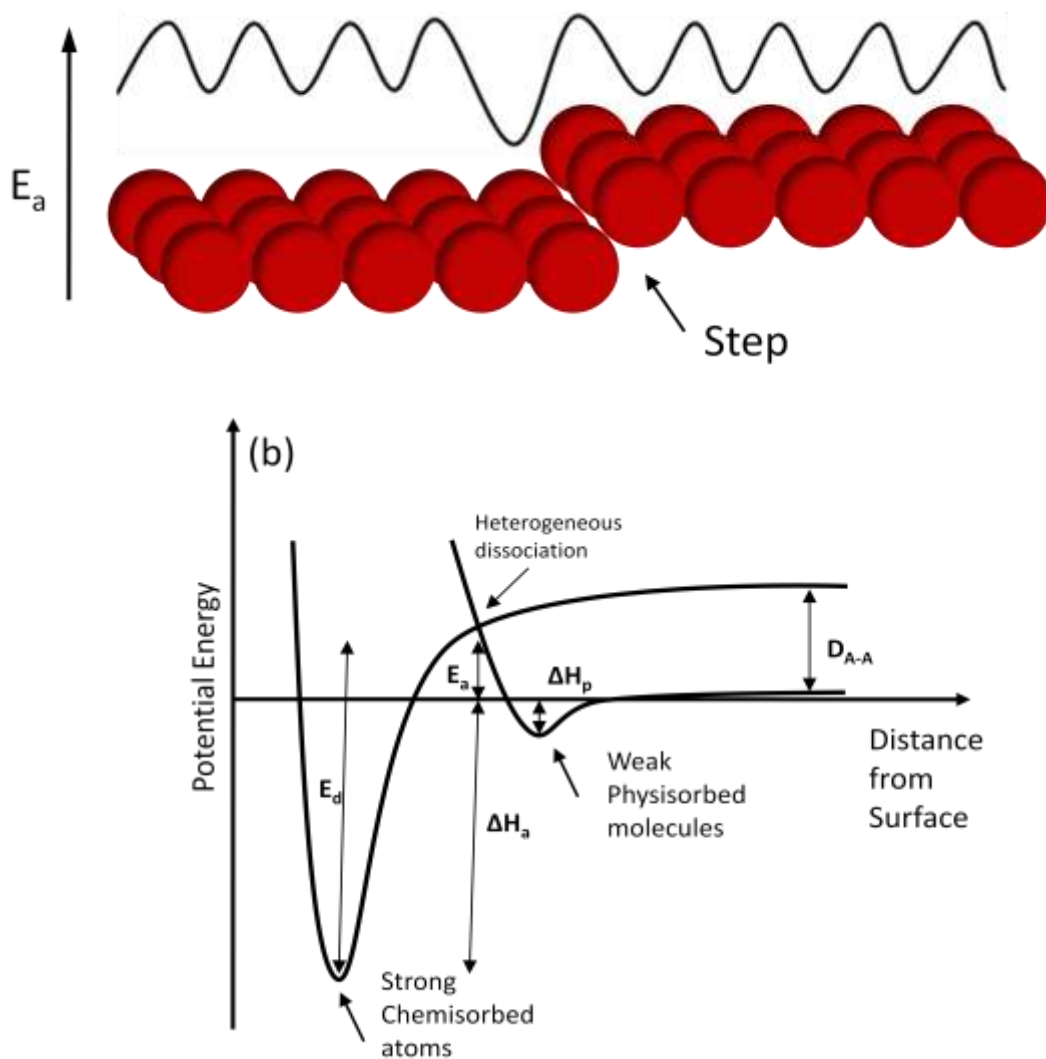


Figure 1.5. (a) A representative surface of a particle with a stepped feature and the general activation energy barrier (E_a) as a function of distance across the surface. At the location of the step, the energy barrier is lower and therefore a preferred ‘active site’ for particle adsorption and potential photocatalysis. (b) Classic Lennard-Jones diagram showing energies of the dissociation (D_{A-A}) of a molecule relative to the distance of the proposed active site of a particle’s surface showing both strong chemisorption and weak physisorption. E_d is denoted as the desorption energy, ΔH_a is the heat of adsorption, and ΔH_p is the heat of physisorption. Adapted from reference 37.

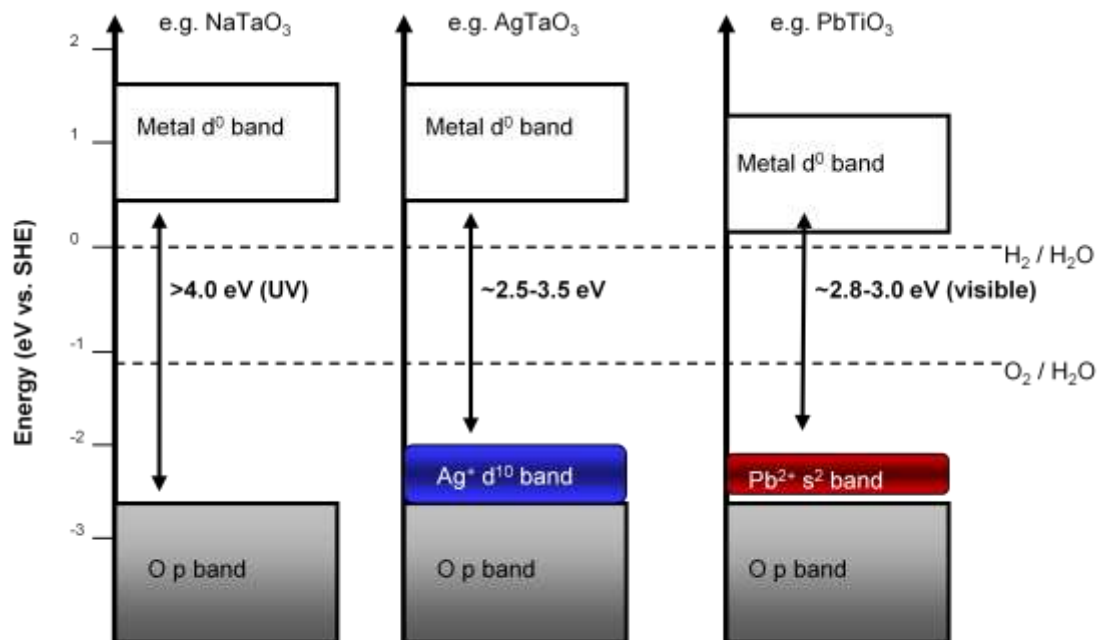


Figure 1.6. Simple band schematic drawing of a photocatalytic metal-oxide particle (left), and the reduced bandgap size with the addition of filled bands arising from $\text{Ag}^+ d^{10}$ (middle) and $\text{Pb}^{2+} s^2$ orbitals.

PART 1. UV-LIGHT ACTIVE PHOTOCATALYSTS

CHAPTER 2

New Molten-Salt Synthesis and Photocatalytic Properties Of $\text{La}_2\text{Ti}_2\text{O}_7$ Particles

An amended paper published in the Journal of Photochemistry and Photobiology A:

Chemistry

Journal of Photochemistry and Photobiology A: Chemistry **2008** 199, 230-235

David Arney, Brittany Porter, Benjamin Greve, and Paul A. Maggard

Department of Chemistry, North Carolina State University, Raleigh, NC 27695

TOC Caption: Platelet-shaped $\text{La}_2\text{Ti}_2\text{O}_7$ particles, with thicknesses down to <100 nm, can be prepared in a single-step molten-salt flux reaction in only 1 – 10 h. The platelet particle sizes can be varied as a function of reaction conditions, e.g. flux amount and reaction time, and which are shown to result in significantly enhanced photocatalytic activities with increasing amounts of exposed crystallite edges and (010) and (001) crystal faces. Further, this synthetic preparation renders them photocatalytically active for hydrogen formation even in pure water

Abstract

The (110)-layered perovskite $\text{La}_2\text{Ti}_2\text{O}_7$ photocatalyst has been synthesized in high purities and in homogeneous microstructures within a molten $\text{Na}_2\text{SO}_4/\text{K}_2\text{SO}_4$ flux in short reaction times of ~1–10 h. The $\text{La}_2\text{Ti}_2\text{O}_7$ particle morphologies and sizes were investigated as a function of flux amounts (flux: $\text{La}_2\text{Ti}_2\text{O}_7$ molar ratios of 1:1, 2:1, 5:1, and 10:1) and reaction times (1 h, 2 h, 5 h, and 10 h). Powder X-ray diffraction confirmed the structure type and high purity, and UV-Vis diffuse reflectance measurements yielded optical bandgap

sizes of $\sim 3.75\text{--}3.81$ eV. Rectangular platelet morphologies are obtained with maximal dimensions of ~ 500 nm - $5,000$ nm, but with thicknesses down to <100 nm, and which decrease in size with increasing amounts of flux used in the synthesis. Photocatalytic activities of the $\text{La}_2\text{Ti}_2\text{O}_7$ products were measured under ultraviolet irradiation in aqueous methanol solutions and yielded rates for hydrogen production from $55 \mu\text{mol H}_2 \text{ h}^{-1} \text{ g}^{-1}$ to $140 \mu\text{mol H}_2 \text{ h}^{-1} \text{ g}^{-1}$, with the maximum photocatalytic rates for the smallest particles, e.g. for 1:1 and 10:1 Flux: $\text{La}_2\text{Ti}_2\text{O}_7$ ratios respectively. The flux-prepared $\text{La}_2\text{Ti}_2\text{O}_7$ products were also photocatalytically active in pure water, yielding maximal rates for hydrogen formation of $31 \mu\text{mol H}_2 \text{ h}^{-1} \text{ g}^{-1}$. The observed photocatalytic rates were up to nearly two times greater than that obtained when $\text{La}_2\text{Ti}_2\text{O}_7$ was prepared by the reported solid-state method, and indicates that a greater number of exposed crystallite edges and the (010) and (001) crystal faces play a key role in the photocatalysis mechanisms for hydrogen formation.

Keywords: Flux synthesis; $\text{La}_2\text{Ti}_2\text{O}_7$; Photocatalysis

Introduction

The synthesis of early transition-metal oxide particles has drawn considerable recent attention owing to their absorption of ultraviolet/visible light and efficient photocatalytic production of H_2 and O_2 from aqueous solutions.¹⁻⁴ Typically, the metal oxides are also loaded with surface cocatalyst islands, such as RuO_2 or Pt particles, and more recently Rh/ Cr_2O_3 core-shell particles, that function to assist the electron transfer and liberation of H_2/O_2 upon irradiation in solution.⁵ Among the many explored titanate, niobate, and

tantalate photocatalysts, solids with layered types of structures have generally been among those exhibiting the highest photocatalytic rates, such as most prominently known for the (110) layered perovskites including $M_2Nb_2O_7$ ($M = Ca, Sr$), $R_2Ti_2O_7$ ($R = Y, La-Yb$) and $La_4CaTi_5O_{17}$.⁶⁻⁷ The reported quantum yields of the (110) layered perovskites range as high as ~20-50 % at ultraviolet wavelengths.^{4,7} Of these layered perovskites, $La_2Ti_2O_7$ has received the most attention because of its photocatalytic activity in the presence of sacrificial reagents or in pure water. Its photocatalytic activity for H_2 and/or O_2 production from aqueous solutions has been studied as a function of different rare-earth (R) elements (e.g. $R_2Ti_2O_7$), with transition-metal dopants for its sensitization to visible light, as well as for the decomposition of organic pollutants.⁸⁻¹⁴ High photocatalytic activities for metal oxides have generally been correlated with smaller particle sizes and with good particle crystallinity. However, the standard solid-state synthesis of $La_2Ti_2O_7$ typically yields low surface areas and requires high temperatures (~1100-1400°C) and repeated regrindings and reheatings owing to the difficulty of achieving good homogeneity and high purity by this method. Relatively few alternative preparative routes to $La_2Ti_2O_7$ have been explored, including hydrothermal syntheses and the high-temperature decomposition of metal-organic precursors.¹⁵⁻¹⁸ These syntheses have provided for smaller particle sizes compared to the solid-state method, but also typically require extended heating times and multi-step synthetic procedures.

Our research efforts in this area have focused on the rapid and simple single-step synthesis (down to ~1 – 2 hour) of metal-oxide photocatalysts within molten-salt fluxes. For example, we recently reported the first flux synthesis of high purity $Bi_5Ti_3FeO_{15}$ and

LaBi₄Ti₃FeO₁₅ with highly-textured platelet-like particle sizes that can be controlled from < 1 μm to > 20 μm, and that are obtained in only 0.5 – 1 h at 800 or 900 °C.¹⁹ We have also demonstrated that these methods allow for the visible-light sensitization of layered perovskite metal oxides, via rapid flux-assisted exchange reactions.²⁰ However, the effect of flux synthesis on the photocatalytic activity of layered metal oxides has not been investigated to date. By comparison, the flux synthesis of a perovskite-type photocatalyst, La-doped NaTaO₃, was found to result in up to a two-fold enhancement of photocatalytic rates, and which was a function of the particle sizes and fine surface features.²¹ A flux-synthesis route to the (110) layered perovskite photocatalyst La₂Ti₂O₇ would be promising for control over the particle-size distributions and homogeneity, and therefore could enable the study of the underlying particle features and surfaces that control its photocatalytic properties.

Presented herein is the new flux synthesis of La₂Ti₂O₇ and an investigation of the effect of its particle sizes/morphologies on optical properties and photocatalytic rates for hydrogen formation. The reaction durations and reactant-to-flux ratios were independently varied, and both of which can affect the particle sizes and cluster aggregation. The products were characterized by powder X-Ray diffraction, UV-Vis diffuse reflectance spectroscopy, BET surface-area analysis, and scanning electron microscopy. Photocatalytic activities were measured in an aqueous methanol as well as pure water solutions, in order to evaluate the effect of particle sizes and morphologies on the rate of H₂ formation, and to compare to those obtained by the solid-state reaction method.

Experimental

Synthesis and Characterization. The flux synthesis of La₂Ti₂O₇ was performed by

combining a stoichiometric mixture of AR grade TiO_2 and La_2O_3 (preheated and dried at 900°C), which was ground together with ~ 10 mL of acetone. After evaporation of the acetone, the reactants were combined with the $\text{Na}_2\text{SO}_4/\text{K}_2\text{SO}_4$ (1:1 molar ratio) salt flux to give flux: $\text{La}_2\text{Ti}_2\text{O}_7$ molar ratios of 1:1, 2:1, 5:1, and 10:1. These reactant mixtures were then placed inside an alumina crucible and heated at 1100°C inside a box furnace for reaction times of 1 h, 2 h, 5 h, and 10 h. The crucibles were allowed to radiatively cool to room temperature and the resulting products were washed with hot deionized water to remove the flux, and then dried overnight in an oven at 80°C . A fine homogeneous white powder of $\text{La}_2\text{Ti}_2\text{O}_7$ was obtained in high purity, as judged from powder X-ray diffraction. The solid-state preparation of $\text{La}_2\text{Ti}_2\text{O}_7$ involved grinding, pelletizing, and heating the La_2O_3 and TiO_2 reactants to 1100°C for 50 h with one intermittent grinding, similar to other reported procedures.⁸ High-resolution Powder X-ray Diffraction (PXRD) patterns of all products were collected on an INEL diffractometer using $\text{CuK}\alpha_1$ ($\lambda=1.54056 \text{ \AA}$) radiation from a sealed-tube X-ray generator (35 kV, 30 mA) using a curved position sensitive detector (CPS120). Scanning electron microscopy (SEM) was performed using a JEOL JEM 6300 in order to examine the particle microstructures and approximate sizes of the reaction products. UV-Vis Diffuse Reflectance Spectra (DRS) were collected on powdered samples using a CARY 3E spectrophotometer equipped with an integrating sphere. BET surface area analyses were performed using a Quantachrome ChemBET Pulsar TPR/TPD.

Photocatalytic Measurements. Measurements of the photocatalytic rates of the flux-synthesized $\text{La}_2\text{Ti}_2\text{O}_7$ products were conducted similar to previously described procedures.²⁰⁻

²³ Each sample was first loaded with 1 wt % platinum cocatalyst by the photodeposition

method. The platinum cocatalyst serves as a well-known kinetic aid in solution for the reduction of H_2O at the surfaces to give H_2 . First, 100 mg of $\text{La}_2\text{Ti}_2\text{O}_7$ was mixed with 30 ml of an aqueous solution of dihydrogen hexachloroplatinate(IV) ($\text{H}_2\text{PtCl}_6 \cdot 6\text{H}_2\text{O}$; Alfa Aesar, 99.95 %), and that was then irradiated using a 400 W Xe arc-lamp with constant stirring for 2 h. After platinization, the grayish-colored $\text{La}_2\text{Ti}_2\text{O}_7$ particles were separated via centrifugation, washed with distilled water to remove any remaining Cl^- ions, and then dried in an oven at 80°C . Next, a weighed (100 mg) amount of the platinized $\text{La}_2\text{Ti}_2\text{O}_7$ was added to an ~90 ml quartz reaction vessel that was then filled with a 20 % aqueous methanol solution, or alternatively, with pure water. The added methanol functions as a hole scavenger, thereby generating CO_2 from photo-oxidation, and which allows the measurement of the formation rate of H_2 alone and without the typically more rate-limiting step of O_2 formation. The photoreaction vessel was connected to a small horizontal quartz tube that trapped the evolved gases, and contained a moveable liquid bubble that allowed a volumetric determination of the amount of evolved gases at a constant pressure. The metal-oxide particles were stirred in the dark for ~ 1 – 2 h to remove any trapped gases on the particles surfaces. Next, this outer-irradiation type quartz reaction cell was irradiated under constant stirring using a 1000 W Xe arc-lamp equipped with an IR water filter and cooled using an external fan. Each of the photocatalytic reactions exhibited the formation of copious amounts of gases that rose to the top of the reaction cell, and that was consistent with the movement of the liquid bubble. The progress of the photocatalytic reactions was marked every hour and used to calculate the amount of gases generated. The trapped gasses were injected into a gas chromatograph (SRI MG #2, helium ionization and thermal conductivity

detectors) in order to identify the formed gases as H₂ and CO₂, and to confirm a constant molar ratio over time.

Results and Discussion

The La₂Ti₂O₇ solid crystallizes in a structure containing (110) perovskite layers spanning four TiO₆ octahedra in width, and which stack together in the monoclinic and polar space group *Pna2₁*.²⁴ The PXRD patterns of the flux products, shown in Figure 2.1, could be fitted and indexed to the La₂Ti₂O₇ structure and confirm that high purity and good crystallinity could be obtained in short reaction times of 1 – 10 h within a Na₂SO₄/K₂SO₄ flux (1:1 molar ratio) at flux:La₂Ti₂O₇ ratios of 1:1, 2:1, 5:1 and 10:1. To evaluate the particle sizes and morphologies of the La₂Ti₂O₇ products, scanning electron microscopy (SEM) images were taken on the samples prepared with flux:La₂Ti₂O₇ ratios of 2:1 and 10:1 for reaction times of 1 h, 2 h, 5 h, and 10 h, shown in Figures 2.2 and 2.3 respectively. These images reveal aggregations of distinct platelet-like particles of La₂Ti₂O₇, and which is typical of layered types of structures where the stacked perovskite layers correspond to the smallest crystal dimension. In this case, the top and bottom faces of the platelet particles would correspond to the (100) crystal faces, and the edges of the particles would correspond to the (010) and the (001) crystal faces. A distribution of platelet particle sizes was observed, with the lengths and widths of the platelets typically in the range of ~500 nm – 2,000 nm for larger flux:La₂Ti₂O₇ ratios of 10:1 and 5:1 and ~1,000 nm – 6,000 nm for smaller flux:La₂Ti₂O₇ ratios of 2:1 and 1:1, as shown in Figures 2.2 and 2.3. A calculated average of particle size collected over several individual platelets observed from SEM data was performed. For the smaller flux:La₂Ti₂O₇ ratio of 2:1, average particle size was calculated to

be 1,068 nm in length while the thickness of the individual platelets were close to 200 nm. For the larger flux:La₂Ti₂O₇ of 10:1, average particle size was approximately 675 nm, with thicknesses close to 100 nm. While the individual particle sizes generally decreased both with increasing flux amounts and reaction time, a distribution of particle sizes could be found in all samples. A distribution of smaller particle sizes would most significantly enhance the number of exposed edges, i.e. the (010) and (001) crystal faces, while the amount of exposed (100) crystal faces would not be affected as significantly. Individual platelets were a few orders of magnitude thinner, down usually to <100 nm. The aggregation of the individual particles into larger agglomerates increased with increasing reaction times in each case, as shown in Figures 2.2 (C and D) and 2.3 (C and D), but this was minimal with higher amounts of flux used in the synthesis. For comparison, SEM micrographs were taken of La₂Ti₂O₇ prepared by the solid-state method and compared to that obtained by flux synthesis, Figure 2.4. The solid-state method yields neither a well-defined crystal morphology nor a range of distinct particle sizes. A calculation of the average particle size shows that La₂Ti₂O₇ samples prepared by the solid state method show an approximate particle size of 320 nm. Nevertheless, the particle morphologies/microstructures are known to directly impact the photocatalytic activities of metal oxides.^{15, 25, 26} Therefore, the flux synthetic technique offers a rapid and single-step approach to target more highly defined particle microstructures, as well as a more distinctive exposure of specific crystal faces that will be critical in probing their roles in photocatalytic properties. To examine the deposition of a 1% wt. platinum cocatalyst onto the surface of the La₂Ti₂O₇ particles, field-emission scanning electron microscopy (FESEM) images were taken of selected flux-prepared products and are shown in

Figure 2.S4 of the supplemental information. Small platinum islands are observed on the faces, edges, and corners of the particles' surface, and appear generally evenly distributed through all observed samples.

Measurements of the UV-Vis diffuse reflectance spectra were taken on all flux-synthesized $\text{La}_2\text{Ti}_2\text{O}_7$ samples in order to verify their optical bandgap sizes and as a probe of the averaged bulk particle sizes. These are shown for several selected samples in Figure 2.5. The optical bandgap sizes were calculated from the onset of absorption using the well-known formula $E_g \text{ (eV)} = 1240 / \lambda_g \text{ (nm)}$, where $\lambda_g \text{ (nm)}$ is extrapolated from the linear rise in the absorption. In all cases, the optical bandgaps were calculated to be within a range of ~3.75-3.81 eV, and were in close agreement with previous studies.^{8,9}

The DRS of the $\text{La}_2\text{Ti}_2\text{O}_7$ samples prepared with a 5:1 flux ratio, Figure 2.5A, illustrate that the diffuse reflectance of sub-bandgap light ($\lambda > 400 \text{ nm}$) increases with increasing reaction times of 1, 2, 5, and 10 hours. A distribution of smaller particle sizes will increase the diffuse reflectance by enhancing the scattering and decreasing light penetration.^{19, 20} Thus, the averaged bulk particle dimensions show a clear trend towards smaller sizes with the 5:1 and 10:1 flux ratios with increasing reaction time, in agreement with the SEM images. However, for the smaller flux ratios of 2:1 and 1:1, the DRS do not increase regularly with increasing reaction time, e.g. showing a higher diffuse reflectance (and larger particle sizes) for 10 h versus 5 h. The smaller amounts of flux allow for more close interactions of the reactants and $\text{La}_2\text{Ti}_2\text{O}_7$ particles and for them to crystallize and grow via a solid-state rather than flux pathway. Thus, the larger amounts of flux are critical for the particles to be well separated. Both increasing amounts of flux and increasing reaction times

yield the smallest particle sizes, as shown together in Figure 2.5B. For comparison, the UV-Vis DRS of $\text{La}_2\text{Ti}_2\text{O}_7$ prepared via the solid-state method is also shown, and which has the lowest diffuse reflectance for the largest particle sizes.

Table 2.S2 lists the measured surface areas of all $\text{La}_2\text{Ti}_2\text{O}_7$ using BET analysis. All flux samples were observed to be within a range of $2.6 - 4.0 \text{ m}^2 \text{ g}^{-1}$. Samples prepared using greater $\text{Na}_2\text{SO}_4/\text{K}_2\text{SO}_4$ flux ratios exhibited higher surface areas (i.e. smaller particle sizes) while those prepared using smaller flux ratios generally had lower surface areas and larger particle sizes, in agreement with the UV-Vis DRS data. The solid-state prepared $\text{La}_2\text{Ti}_2\text{O}_7$ exhibited a measured surface area of $1.1 \text{ m}^2 \text{ g}^{-1}$, which was the lowest observed of all $\text{La}_2\text{Ti}_2\text{O}_7$ samples.

The $\text{La}_2\text{Ti}_2\text{O}_7$ compound prepared by the solid-state method is among the most efficient photocatalysts reported, exhibiting quantum efficiencies of up to ~20-50 %, depending on the dopants and surface co-catalysts.^{4,7} Upon irradiation by bandgap or greater energies, the electrons that are excited into the conduction band serve to reduce water to H_2 at the Pt co-catalyst sites, while the photo-generated holes in the conduction band are scavenged by methanol to produce CO_2 . The latter is used in order to measure the formation rate of H_2 alone, as the oxidation of water to O_2 can be slower and rate limiting. Flux syntheses of different particle size distributions, as well as the different amounts of (100) and (010) or (001) crystal faces, can both potentially impact the rates of these surface reactions. Hence, the photocatalytic rates of H_2 production was measured for each $\text{La}_2\text{Ti}_2\text{O}_7$ sample under identical conditions, using ultraviolet irradiation in an outer-irradiation quartz reaction vessel in a 20 % aqueous methanol or pure water solution. Listed in Table 2.1 are the

reaction conditions and measured photocatalytic rates for the $\text{La}_2\text{Ti}_2\text{O}_7$ samples. The photocatalysis rates generally increased with increasing reaction times, with up to a $\times 2$ - $\times 3$ increase for flux reactions at 10 h and 5 h ($\sim 100 - 140 \mu\text{mol H}_2 \text{ h}^{-1} \text{ g}^{-1}$) versus 2h or 1h ($\sim 30 - 80 \mu\text{mol H}_2 \text{ h}^{-1} \text{ g}^{-1}$). The higher rates therefore correlate with the smaller particle size distributions and a higher number of exposed crystal edges and (010) and (001) surfaces, as confirmed by the SEM and DRS results (above). All $\text{La}_2\text{Ti}_2\text{O}_7$ samples prepared with a reaction time of 5 h or longer yielded rates higher than that exhibited by the sample prepared by the solid state method, which exhibited a rate of $87 \mu\text{mol H}_2 \text{ h}^{-1} \text{ g}^{-1}$. Shorter reaction times yielded lower rates than that of the solid-state sample. A comparison of the effect of both the flux amount and reaction time for the 10:1 and 5:1 samples is shown in Figure 2.6, which is a plot of the formation of H_2 versus time. The higher 10:1 ratio gave much higher rates, see blue versus green lines, while the shortest flux reaction times have lower rates in each case, see the dotted versus solid lines. However, this illustrates that the reaction time has the more predominant effect on rates than the flux: $\text{La}_2\text{Ti}_2\text{O}_7$ ratio, which exhibited little discernible trends. This is likely the result of a range of particle size distributions in every sample, as well as by partially solid-state driven reactions at the lower flux ratios of 2:1 and 1:1. The enhanced photocatalytic activities of the smaller and anisotropic platelet particles suggest that these platelet edges, i.e. orthogonal to the perovskite layer, are a significant factor in the high photocatalytic activity that had previously been observed for $\text{La}_2\text{Ti}_2\text{O}_7$.

For comparison, selected $\text{La}_2\text{Ti}_2\text{O}_7$ samples were tested in deionized water for photocatalysis. Each sample was loaded with a 1 % Pt cocatalyst and placed in a reaction vessel with ~ 90 mL deionized water. Photocatalytic testing of both the solid state sample

and the 2 h 2:1 flux: $\text{La}_2\text{Ti}_2\text{O}_7$ sample showed zero activity after several hours of testing. The 10 h 10:1 flux: $\text{La}_2\text{Ti}_2\text{O}_7$ sample exhibited a rate of H_2 production in pure water of $31 \mu\text{mol H}_2 \text{ g}^{-1} \text{ h}^{-1}$, averaged over ~12 hours, which was ~23 % of the rate in an aqueous methanol solution. Thus, the smallest particles with the largest amount of edges showed some of the highest activities in 20 % aqueous methanol, and as well, the surfaces had been rendered active for hydrogen production even in a pure water solution.

Conclusions

The rapid single-step synthesis of the (110) layered perovskite $\text{La}_2\text{Ti}_2\text{O}_7$ can be performed in a molten $\text{Na}_2\text{SO}_4/\text{K}_2\text{SO}_4$ flux at 1100°C in short reaction times of 1 h – 10 h. Platelet-like particle morphologies are obtained in high purity and with homogeneous microstructures that range in size from ~500 nm – 6,000 nm, with thicknesses of <100 nm. The smallest particle-size distributions of ~500 nm – 2,000 nm were obtained for increasing amounts of flux and the longer reaction times of 5 h and 10 h. Measured optical bandgap sizes of the $\text{La}_2\text{Ti}_2\text{O}_7$ products were in the range of ~3.75 – 3.81 eV. UV-Vis DRS exhibited higher diffuse reflectances for the 10:1 and 5:1 samples for longer reaction times, i.e. for the samples with smaller particle sizes. Photocatalytic activities of the flux-synthesized $\text{La}_2\text{Ti}_2\text{O}_7$ samples in an aqueous methanol solution were ~55 – 140 $\mu\text{mol H}_2 \text{ h}^{-1} \text{ g}^{-1}$, with the maximum rates for the flux reactions time of 5 h or longer. The measured rates were nearly twice as large than for $\text{La}_2\text{Ti}_2\text{O}_7$ prepared by the solid-state method, and strongly suggest a key role of the crystallite edges and the (010) and (001) crystal faces in the origins of its high activity. Further, the flux-synthesized particles resulting from the highest flux ratio and reaction time were highly active for hydrogen production even in pure water. Thus, flux

synthetic preparations of $\text{La}_2\text{Ti}_2\text{O}_7$ particles has enabled a beginning of deeper insights into the surface features that govern its high photocatalytic activity.

Acknowledgments

Support of this work is acknowledged from the Beckman Foundation through the Beckman Young Investigator Program (P.M.), and the Chemical Sciences, Geosciences, and Biosciences Division, Office of Energy Basic Energy Sciences, Office of Science, U.S. Department of Energy. (DE-FG02-06ER06-15).

Supporting Information

UV-Vis diffuse reflectance spectra of all flux-synthesized products, refined lattice parameters, and EDS results for composition analysis. Supplementary data associated with this article can be found in the online version, at [doi:10.1016/j.jphotochem.2008.06.005](https://doi.org/10.1016/j.jphotochem.2008.06.005).

References

- (1) M. Grätzel (Ed.), *Energy Resources through Photochemistry and Catalysis*, Academic Press, New York, 1983.
- (2) H. Kato, A. Kudo, *Catal. Today* 78 (2003) 561-569.
- (3) K. Domen, J.N. Kondo, M. Hara, T. Takata, *Bull Chem. Soc. Jpn.* 73 (2000) 1307-1331.
- (4) J. Kim, D.W. Hwang, H.G. Kim, S.W. Bae, J.S. Lee, W. Li, S.H. Oh, *Topics Catal.* 35 (2005) 295-303.
- (5) a) K. Maeda, K. Teramura, D. Lu, N. Saito, Y. Inoue, K. Domen, *Angew. Chem. Int. Ed.* 45 (2006) 7806-7809; b) K. Maeda, K. Teramura, D. Lu, N. Saito, Y. Inoue, K. Domen, *J. Phys. Chem. C* 111 (2007) 7554-7560.
- (6) D.W. Hwang, H.G. Kim, J. Kim, K.Y. Cha, Y.G. Kim, J.S. Lee, *J. Catal.* 193 (2000) 40-48.
- (7) H.G. Kim, D.W. Hwang, J. Kim, Y.G. Kim, J.S. Lee *Chem. Commun.* (1999) 1077-1078.
- (8) D.W. Hwang, J.S. Lee, W. Li, S.H. Oh, *J. Phys. Chem. B* 107 (2003) 4963-4970.
- (9) R. Abe, M. Higashi, K. Sayama, Y. Abe, H. Sugihara, *J. Phys. Chem. B* 110 (2006) 2219-2226.
- (10) M. Uno, A. Kosuga, M. Okui, K. Horisaka, S. Yamanaka, *J. Alloys Compds.* 400 (2005) 270-275.
- (11) D.W. Hwang, H.G. Kim, J.S. Lee, J. Kim, W. Li, S.H. Oh, *J. Phys. Chem. B* 109 (2005) 2093-2102.

- (12) D.W. Hwang, H.G. Kim, J.S. Jang, S.W. Bae, S.M. Ji, J.S. Lee, *Catal. Today* 93-95 (2004) 845-850.
- (13) J. Kim, D.W. Hwang, H.G. Kim, S.W. Bae, S.M. Ji, J.S. Lee, *Chem. Commun.* (2002) 2488-2489.
- (14) D.W. Hwang, K.Y. Cha, J. Kim, H.G. Kim, S.W. Bae, J.S. Lee, *Ind. Eng. Chem. Res.* 42 (2003) 1184-1189.
- (15) K. Li, Y. Wang, H. Wang, M. Zhu, H. Yan, *Nanotech.* 17 (2006) 4863-4867.
- (16) H. Song, T. Peng, P. Cai, H. Yi, C. Yan, *Catal. Lett.* 113 (2007) 54-58.
- (17) J. Kim, D.W. Hwang, S.W. Bae, Y.G. Kim, J.S. Lee, *Kor. J. Chem. Eng.* 18 (2001) 941-947.
- (18) H.G. Kim, D.W. Hwang, S.W. Bae, J.H. Jung, J.S. Lee, *Catal. Lett.* 91 (2003) 193-193.
- (19) D.G. Porob, P.A. Maggard, *Mater. Res. Bull.* 41 (2006) 1513-1519.
- (20) D.G. Porob, P.A. Maggard, *Chem. Mater.* 19 (2007) 970-972.
- (21) D.G. Porob, P.A. Maggard, *J. Solid St. Chem.* 179 (2006) 1727-1732.
- (22) Z. Zhang, P.A. Maggard, *J. Photochem. Photobio. A* 186 (2007) 8-13.
- (23) J. Luo, P.A. Maggard, *Adv. Mater.* 18 (2006) 514-517.
- (24) M. Gasperin, *Acta Cryst. B* 31 (1975) 2129-2130.
- (25) C. Chang, Y. Zhu, *Chem. Mater.* 17 (2005) 3537-3545.
- (26) H. Kato, K. Asakura, A. Kudo, *J. Am. Chem. Soc.* 125 (2003) 3082-3089

Table 2.1

Measured photocatalytic rates of hydrogen formation for $\text{La}_2\text{Ti}_2\text{O}_7$ prepared using a $\text{Na}_2\text{SO}_4/\text{K}_2\text{SO}_4$ flux and also by the solid-state method.

Sample	Synthetic Conditions		Activity ($\mu\text{mol H}_2/\text{h g}$)
	Flux: $\text{La}_2\text{Ti}_2\text{O}_7$ ratio	Time (h)	
$\text{La}_2\text{Ti}_2\text{O}_7$ std ^a	-	-	87
LTO1	1:1	1	55
LTO2	2:1	1	-
LTO3	5:1	1	58
LTO4	10:1	1	68
LTO5	1:1	2	80
LTO6	2:1	2	50
LTO7	5:1	2	30
LTO8	10:1	2	74
LTO9	1:1	5	87
LTO10	2:1	5	140
LTO11	5:1	5	119
LTO12	10:1	5	89
LTO13	1:1	10	138
LTO14	2:1	10	107
LTO15	5:1	10	99
LTO16	10:1	10	130

^a Prepared by solid-state reaction of TiO_2 and La_2O_3 reactants at 1100°C for 50h.

^b Testing conditions: Outer irradiation 1000W high-pressure Xe arc-lamp, 100mg of $\text{La}_2\text{Ti}_2\text{O}_7$, 20% aqueous methanol solution, and 1 wt% Pt surface cocatalyst.

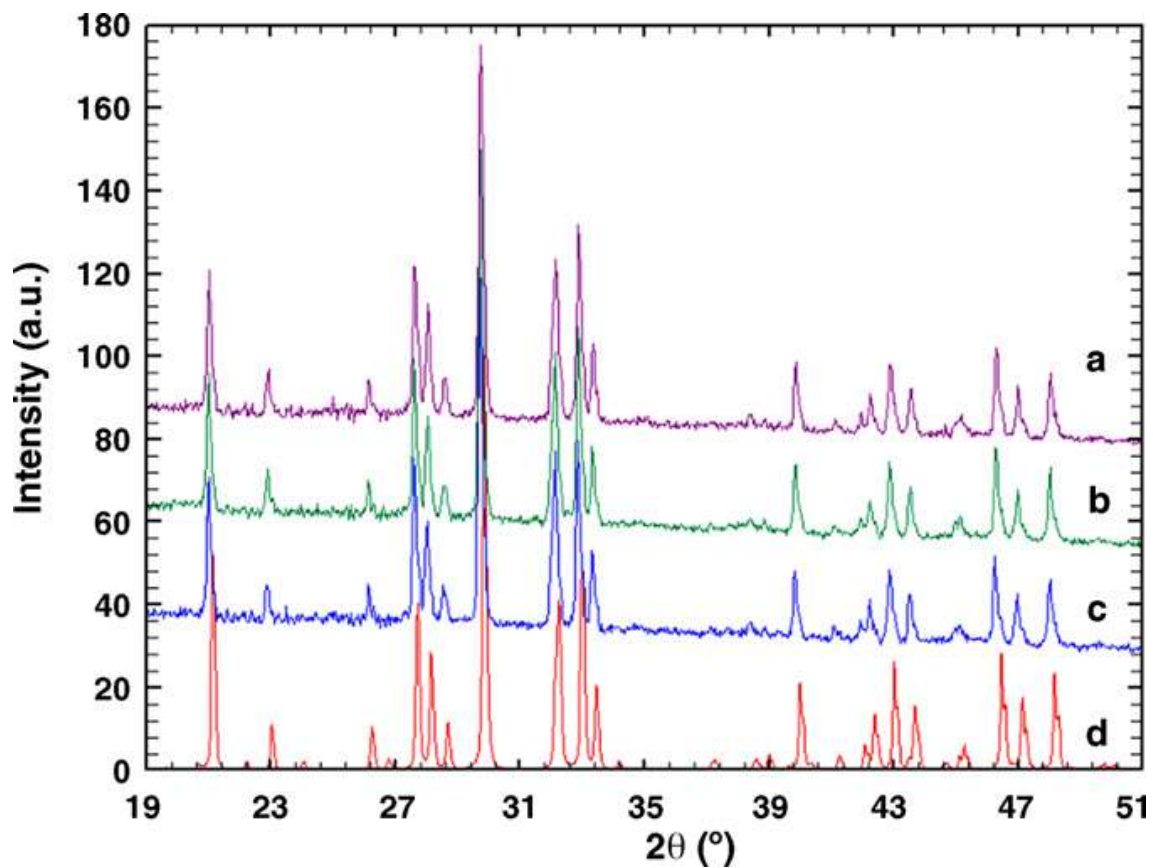


Figure 2.1. The PXR D of the $\text{La}_2\text{Ti}_2\text{O}_7$ products prepared using (a) a 10:1 flux ratio heated for 10 h, (b) a 1:1 flux ratio heated for 1 h, (c) solid-state methods (1100 °C, 50 h), and compared to (d) the calculated theoretical pattern.

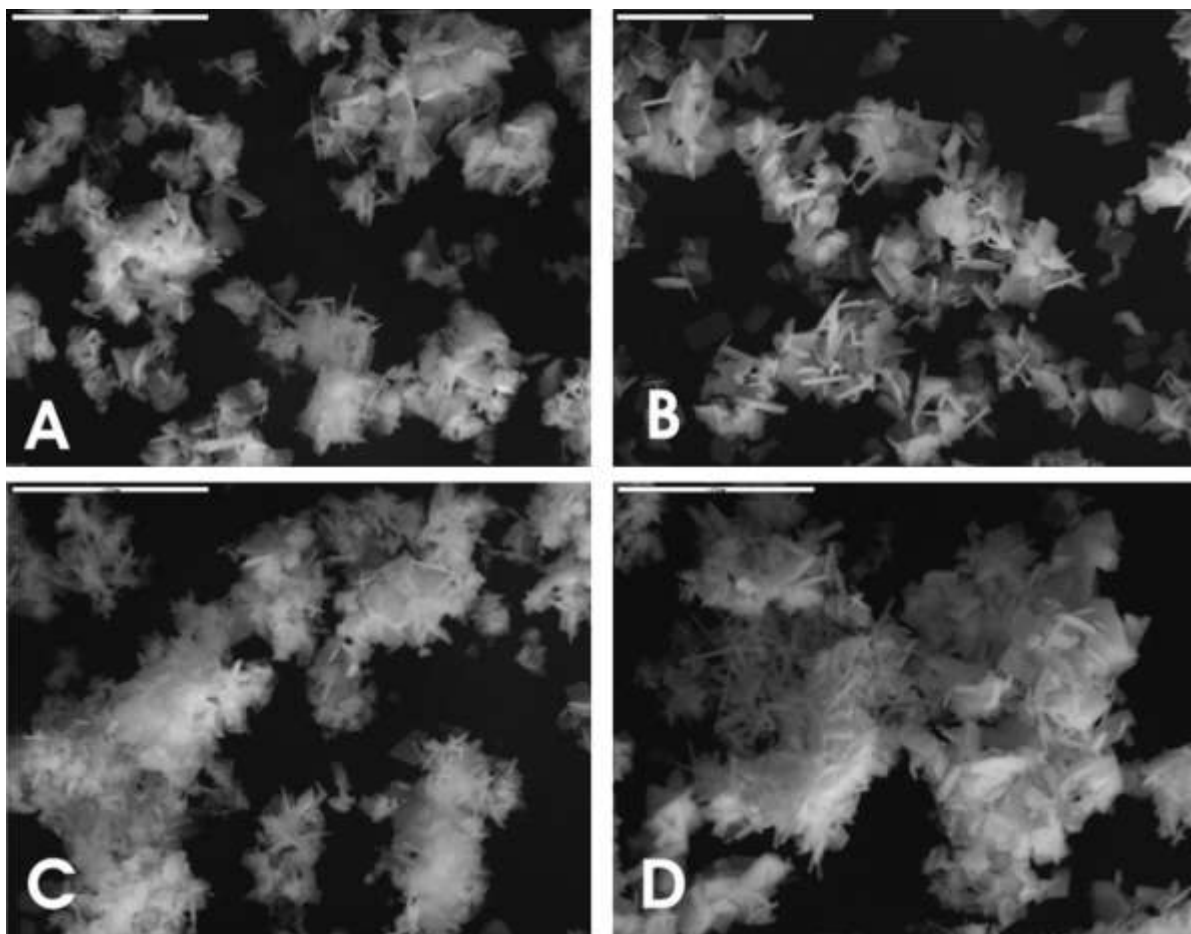


Figure 2.2. SEM images of washed flux products for a 2:1 molar ratio of flux: $\text{La}_2\text{Ti}_2\text{O}_7$ after reaction times of (A) 1h, (B) 2h, (C) 5h, and (D) 10h. The scale is $10\mu\text{m}$.

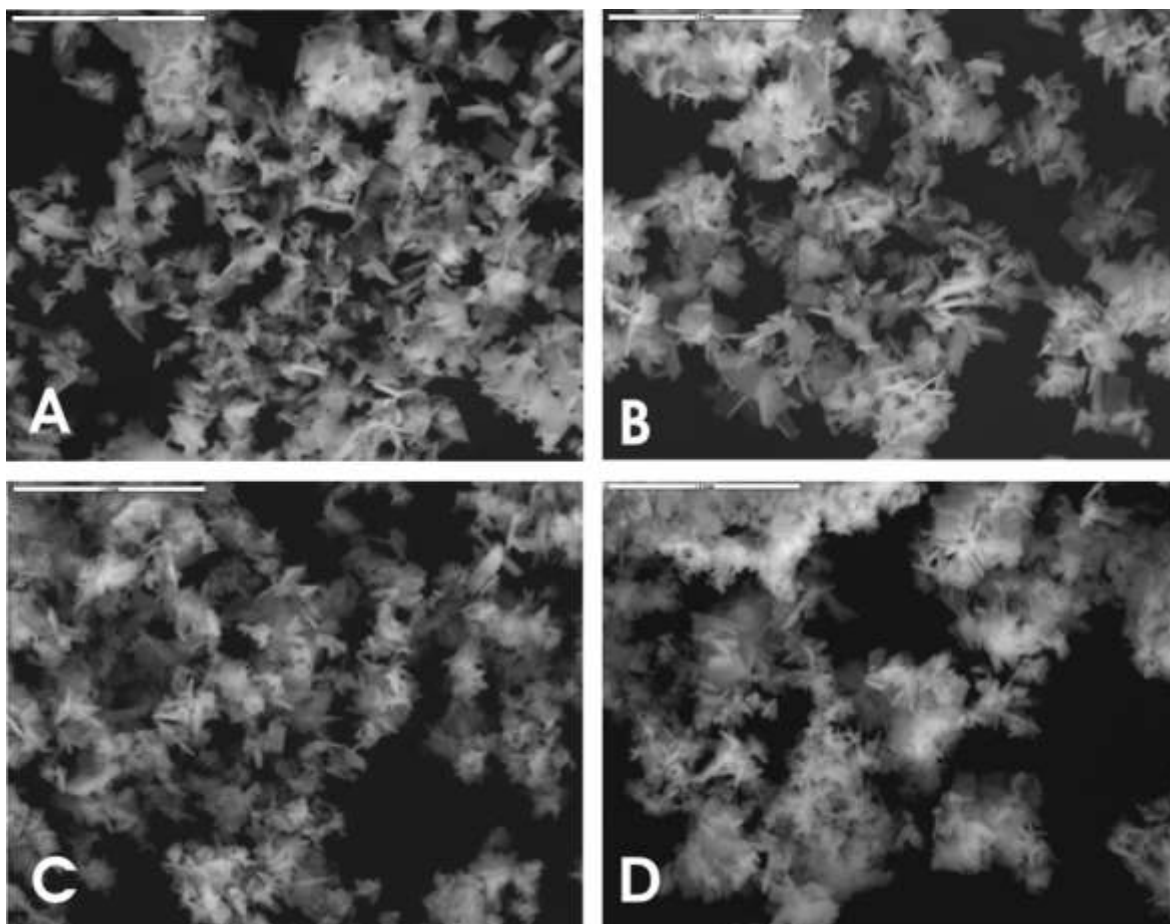


Figure 2.3. SEM images of washed flux products for a 10:1 molar ratio of flux: $\text{La}_2\text{Ti}_2\text{O}_7$ after reaction times of (A) 1h, (B) 2h, (C) 5h, and (D) 10h. The scale is $10\mu\text{m}$.

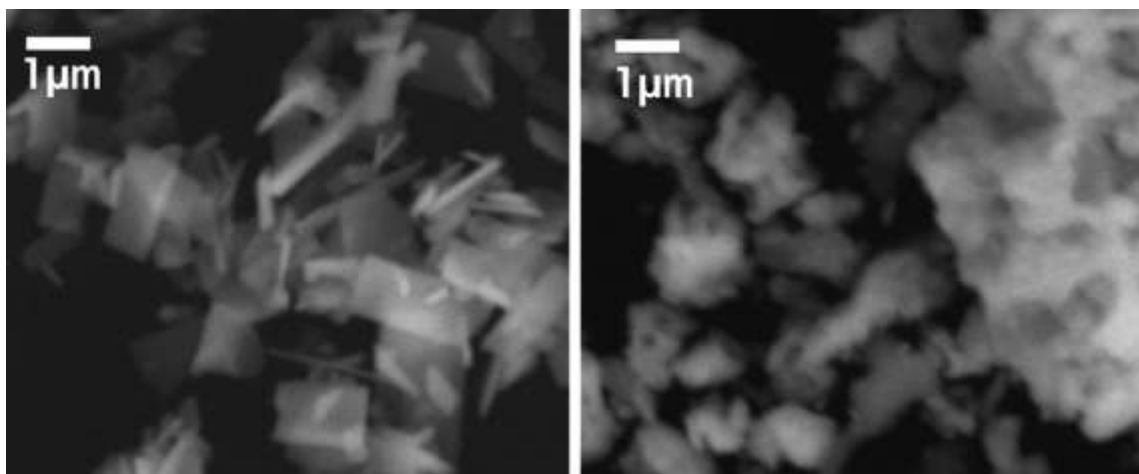


Figure 2.4. Comparison of the SEM images of the particle morphologies obtained from a flux reaction (left; 10:1 ratio and 1h reaction time) and from a solid-state preparation (right).

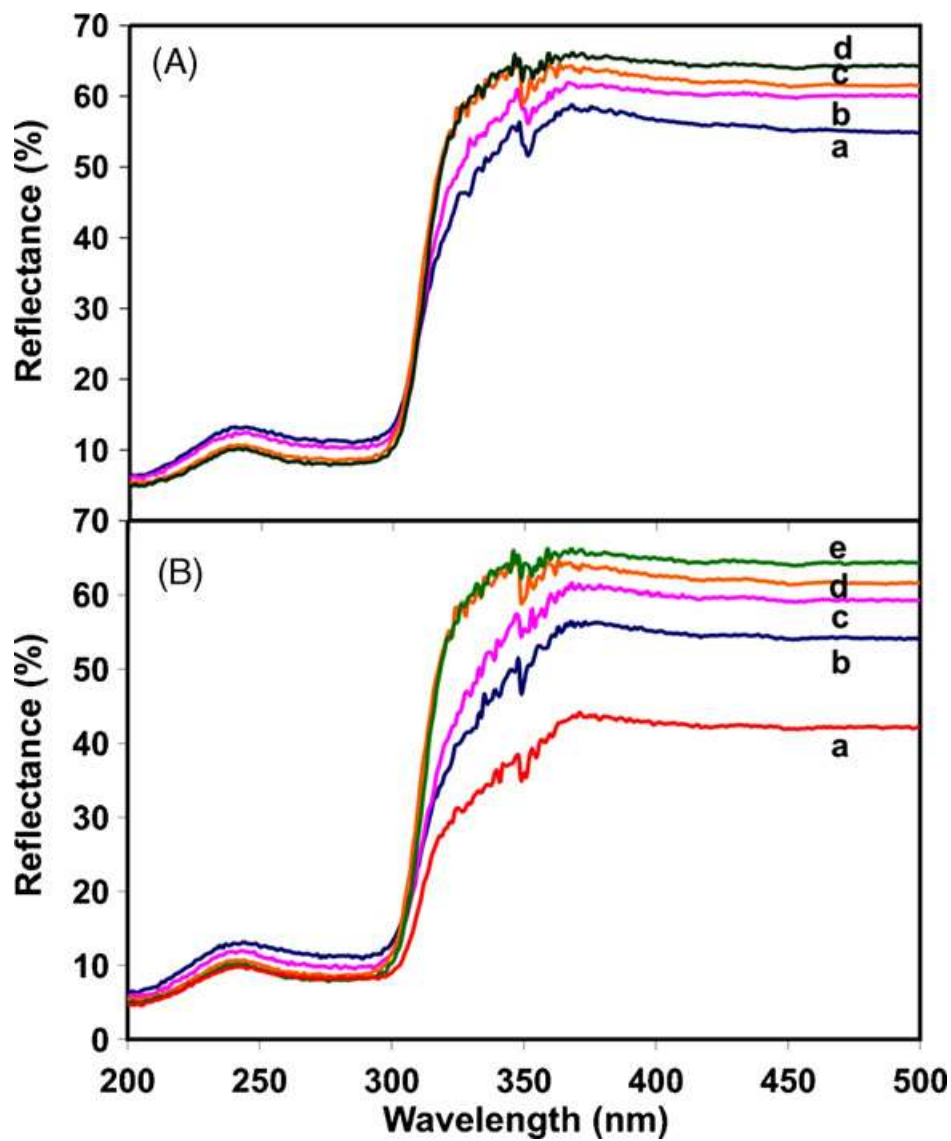


Figure 2.5. Plots of UV-Vis diffuse reflectance, as % reflectance versus wavelength, for (A) a 5:1 flux: $\text{La}_2\text{Ti}_2\text{O}_7$ ratio reacted for (a) 1h, (b) 2h, (c) 5h and (d) 10h, and (B) for the (a) solid-state sample and the flux samples of (b) 1:1 at 1h, (c) 2:1 at 2h, (d) 5:1 at 5h, and (e) 10:1 at 10h.

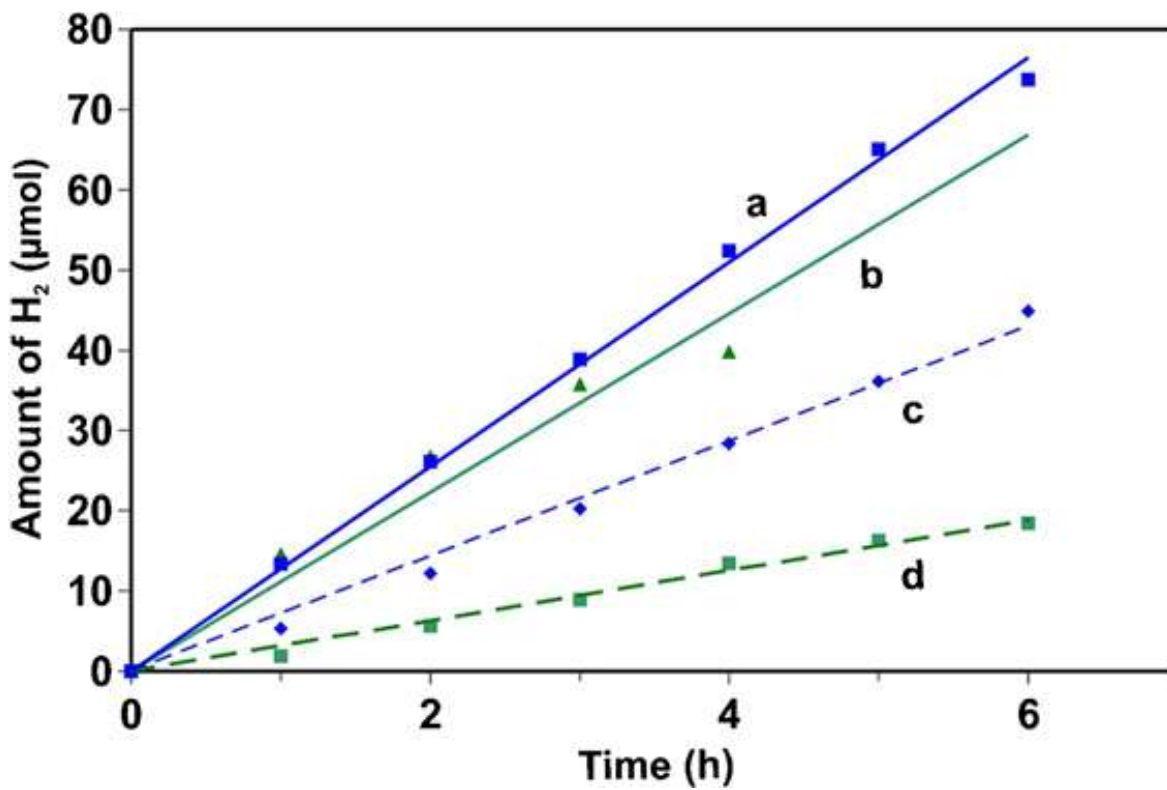


Figure 2.6. Photocatalytic formation of hydrogen versus time for flux-synthesized $\text{La}_2\text{Ti}_2\text{O}_7$ prepared in a reaction time and flux: $\text{La}_2\text{Ti}_2\text{O}_7$ ratio of (a) 10h and 10:1, (b) 5h and 5:1, (c) 1h and 10:1, and (d) 2h and 5:1.

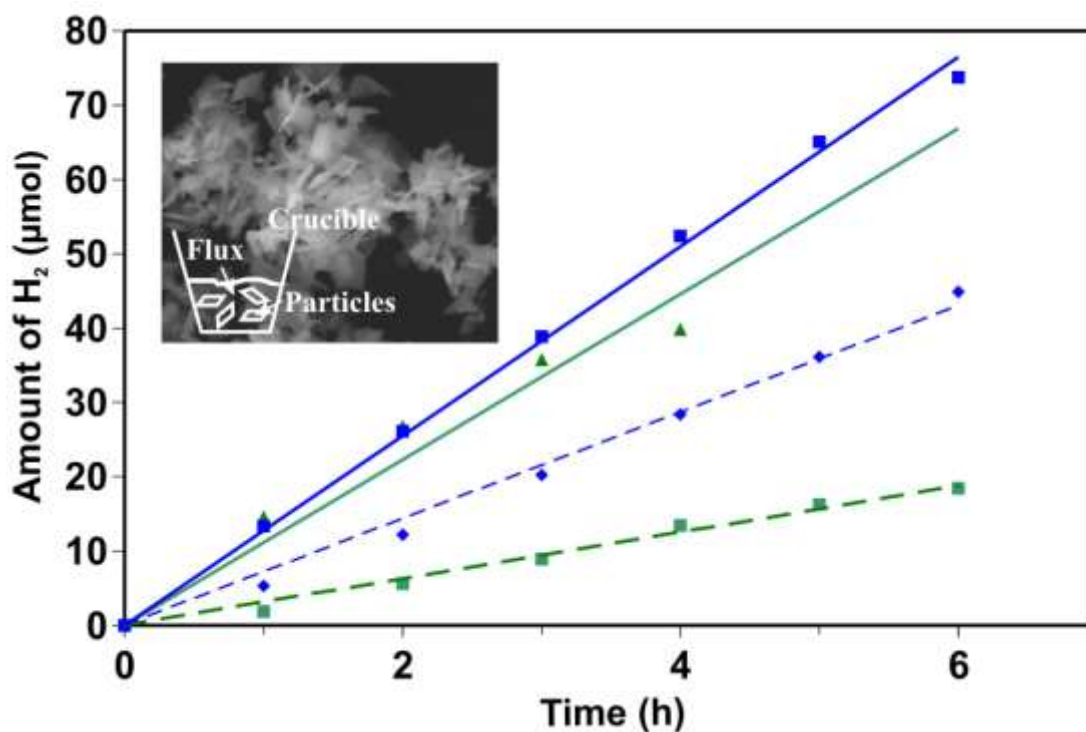


Figure 2.7. TOC Caption Photocatalytic $\text{La}_2\text{Ti}_2\text{O}_7$ platelet-shaped particles, with thicknesses down to $<100\text{nm}$, can be prepared in a single-step molten-salt flux reaction in only 1 – 10h. The platelet particle sizes can be varied as a function of reaction conditions, e.g. flux amount and reaction time, and which are shown to result in enhanced photocatalytic activities for hydrogen formation compared to a conventional solid-state preparation.

Supporting Information

“New Molten-Salt Synthesis and Photocatalytic Properties Of $\text{La}_2\text{Ti}_2\text{O}_7$ ”
David Arney, Brittany Porter, Benjamin Greve, and Paul A. Maggard*

Table 2.S1. Refined cell parameters^a for $\text{La}_2\text{Ti}_2\text{O}_7$ synthesized by different Flux-prepared conditions.

Sample Name	$a(\text{\AA})$	$b\text{\AA}$	$c\text{\AA}$	Volume (\AA^3)
LTO 1:1 Flux, 1 h	7.810(1)	13.013(1)	5.5486(7)	557.72(8)
LTO 2:1 Flux, 2 h	7.791(2)	12.983(5)	5.537(2)	553.7(6)
LTO 5:1 Flux, 5 h	7.801(1)	12.996(2)	5.5415(9)	555.7(1)
LTO 10:1 Flux, 10 h	7.815(1)	13.020(1)	5.551(1)	558.5(1)

^aUnit cell parameters were refined by Rietveld analysis using the program GSAS and software EXPGUI.

Table 2.S2. Measured BET surface area^a of $\text{La}_2\text{Ti}_2\text{O}_7$ particles in $\text{m}^2 \text{g}^{-1}$.

Sample	Synthetic Conditions		S.A. (m^2/g)
	Flux: $\text{La}_2\text{Ti}_2\text{O}_7$ ratio	Time (h)	
$\text{La}_2\text{Ti}_2\text{O}_7$ std	-	-	1.1
LTO1	1:1	1	2.6
LTO2	2:1	1	3.34
LTO3	5:1	1	3.7
LTO4	10:1	1	3.75
LTO5	1:1	2	3.0
LTO6	2:1	2	3.3
LTO7	5:1	2	4.0
LTO8	10:1	2	3.2
LTO9	1:1	5	3.1
LTO10	2:1	5	3.11
LTO11	5:1	5	3.5
LTO12	10:1	5	3.13
LTO13	1:1	10	3.2
LTO14	2:1	10	2.6
LTO15	5:1	10	3.1
LTO16	10:1	10	3.0

^a Data added January, 2011.

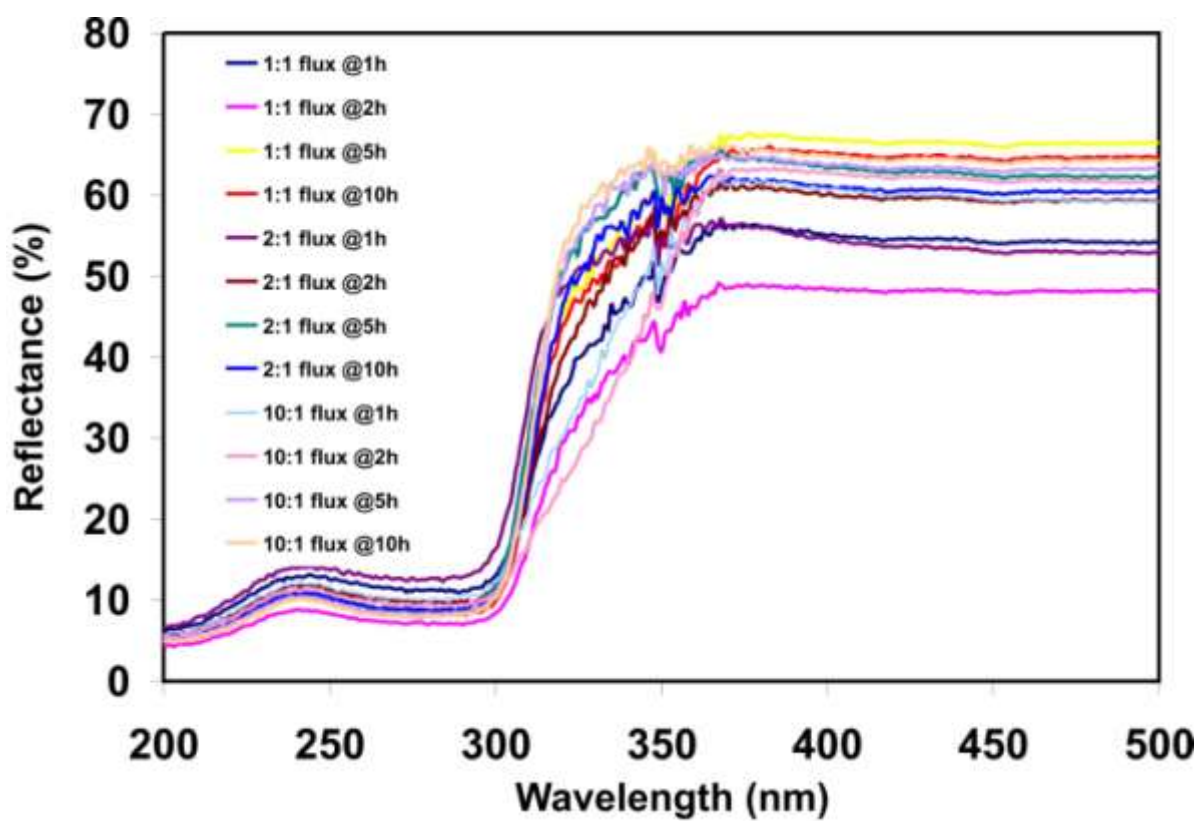


Figure 2.S1. UV-Vis diffuse reflectance measurements, plotted as % reflectance versus wavelength, for flux: $\text{La}_2\text{Ti}_2\text{O}_7$ ratios of 10:1, 5:1, 2:1 and 1:1 for reaction times of 1, 2, 5, and 10 hours.

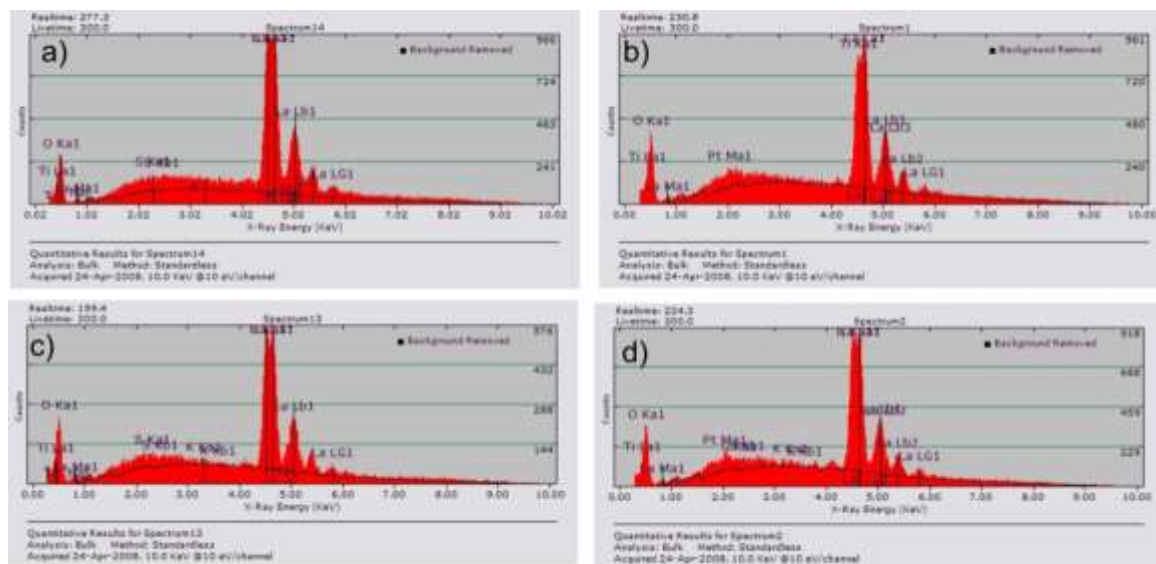


Figure 2.S2. EDS Spectra of $\text{La}_2\text{Ti}_2\text{O}_7$ samples prepared a) with a 2:1 flux ratio for 1h, b) 2:1 flux ratio for 10h, c) 10:1 flux ratio for 1h, and d) by the solid-state method.

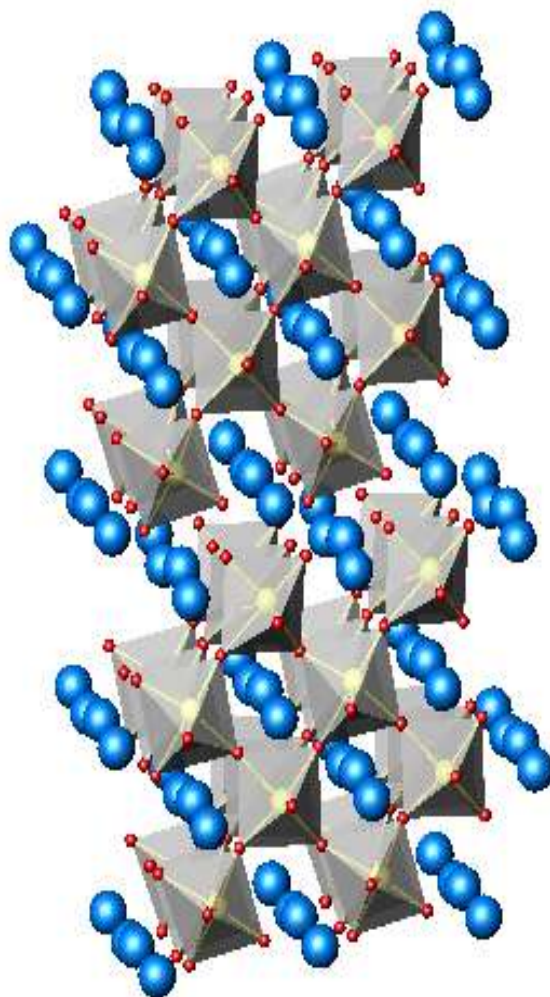


Figure 2.S3. Structure of layered perovskite $\text{La}_2\text{Ti}_2\text{O}_7$. TiO_6 octahedra are shown in grey, while La^{3+} ions fill the interstitial sites. Space group $\text{Pna}2_1$.

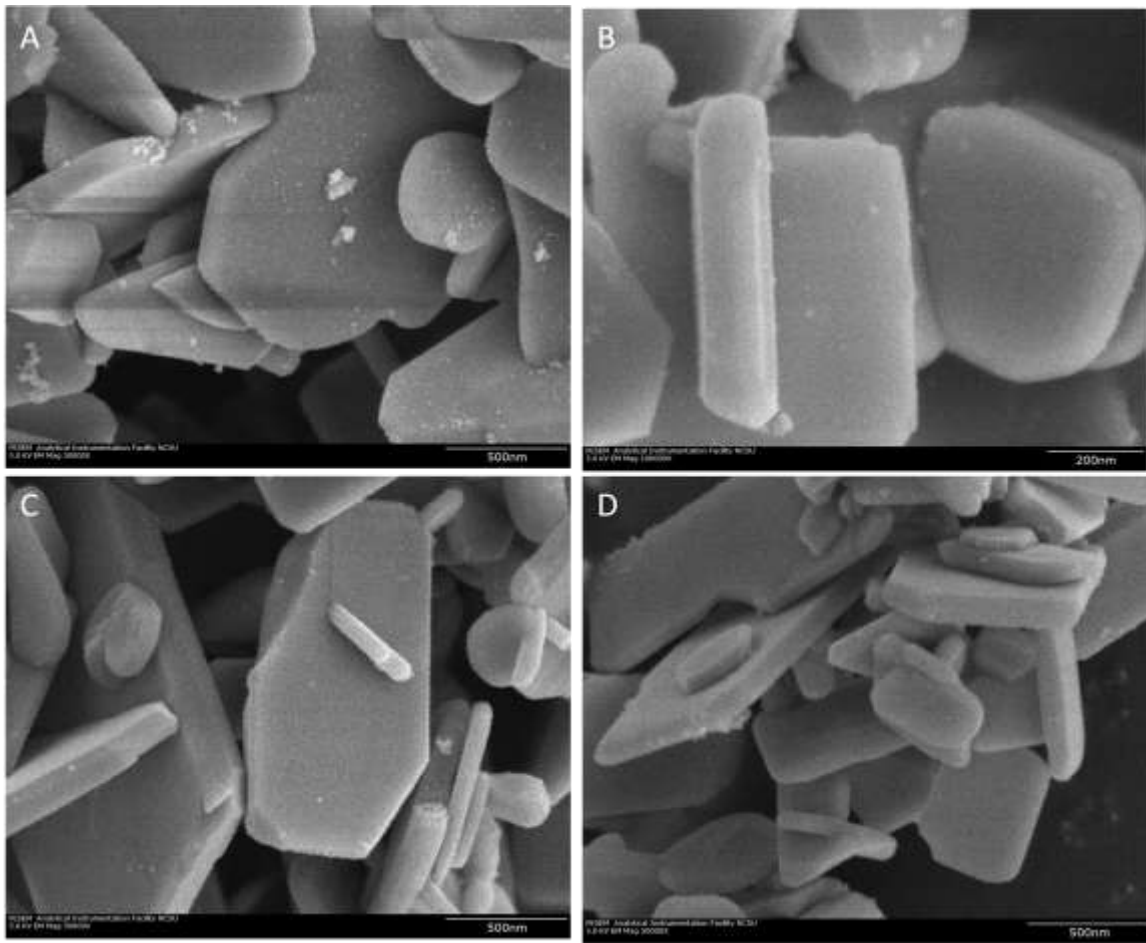


Figure 2.S4. FESEM images of $\text{La}_2\text{Ti}_2\text{O}_7$ taken after a 1% deposition of a platinum cocatalyst by the photodeposition method. (A and B) 1:1 flux heated for 1h, (C and D) 10:1 flux heated for 1h. (Data added August 2010).

CHAPTER 3

Particle Size Control and Photocatalytic H₂ Production From Na₂Ca₂Nb₄O₁₃ Crystals Grown From a Molten Flux

A paper prepared for submission

David Arney and Paul A. Maggard*

Department of Chemistry, North Carolina State University, Raleigh, NC 27695

Abstract

The (n=4) layered Ruddlesden-Popper phase perovskite Na₂Ca₂Nb₄O₁₃ was prepared in molten NaCl and Na₂SO₄ fluxes using 5:1 – 20:1 flux-to-reactant molar ratios heated to 1100°C for a duration of 10 h and slow cooled for 50 h. Long thin rods and large flat platelets were obtained for samples prepared using a NaCl and Na₂SO₄ flux, respectively, with surface areas ranging from 0.36 – 4.6 m²/g. A bandgap size of ~3.3 eV was determined by UV-Vis diffuse reflectance measurements. The smallest particle sizes and highest surface areas were obtained for the 5:1 NaCl flux molar ratio. The photocatalytic activities of the Na₂Ca₂Nb₄O₁₃ particles were evaluated in an aqueous methanol solution and yielded a maximum rate of 1355 μmol H₂·g⁻¹·h⁻¹ for the 5:1 NaCl flux-prepared sample. Higher rates were correlated with the surface area of the particles. The apparent quantum yield of the Na₂Ca₂Nb₄O₁₃ was 6.5% at 350 nm. Additionally, the deposition of a platinum cocatalyst along exposed edges and nanofeatures greatly influenced the photocatalytic activity of the particles.

Keywords: Flux Synthesis; Na₂Ca₂Nb₄O₁₃; photocatalysis

1. Introduction

Developing novel and efficient photocatalytic materials currently is of considerable interest with respect to renewable energy resources, particularly in the synthesis of early

transition-metal oxides.¹ Layered metal oxide materials have been some of the most successful produced, exhibiting high photocatalytic rates and quantum efficiencies under UV irradiation, such as $\text{Sr}_2\text{Ta}_2\text{O}_7$, $\text{La}_4\text{CaTi}_5\text{O}_{17}$, $\text{La}_2\text{Ti}_2\text{O}_7$, and $\text{Rb}_4\text{Nb}_6\text{O}_{17}$.²⁻⁶ Typically, these materials are synthesized using traditional solid state techniques. However, lack of control over particle size, morphology, and surface area have limited optimization of photocatalytic parameters from the perspective of particle size and shape. Alternatively, synthesis using molten salt or flux techniques have shown to provided a greater control over particle size and morphology, reduced heating times and reaction temperatures, and also improve photocatalytic performance with respect to their solid state-prepared counterparts.^{5,7-10}

It is with this motivation that we have focused our research efforts towards the photocatalytic study of the flux synthesis of the $n=4$ layered Ruddlesden-Popper phase perovskite $\text{Na}_2\text{Ca}_2\text{Nb}_4\text{O}_{13}$. Extensive research has been performed on the $n=3$ layered potassium photocatalyst analogue $\text{KCa}_2\text{Nb}_3\text{O}_{10}$, but to the authors' best knowledge the photocatalytic properties of $\text{Na}_2\text{Ca}_2\text{Nb}_4\text{O}_{13}$ have not yet been explored.¹¹⁻¹⁴ The flux synthesis of $\text{Na}_2\text{Ca}_2\text{Nb}_4\text{O}_{13}$ crystals using molten NaCl and Na_2SO_4 was reported previously by Chiba and Oishi.¹⁵⁻¹⁸ Presented herein is the molten flux synthesis of $\text{Na}_2\text{Ca}_2\text{Nb}_4\text{O}_{13}$ particles and an investigation of the effect of its particle sizes and morphologies on the photocatalytic rates for the production of H_2 . Additionally, the deposition sites of a platinum cocatalyst were also studied by field emission microscopy (FESEM) to compare how the photocatalytic activity varies from two deposition methods, photochemical deposition (PCD) and incipient wetness impregnation (IWI). The reactant-to-flux ratios were independently varied and their products were characterized by powder X-ray diffraction (PXRD), UV-vis

diffuse reflectance spectroscopy, BET surface area analysis, and scanning electron microscopy (SEM).

2. Experimental

2.1. Synthesis and characterization

The flux synthesis of $\text{Na}_2\text{Ca}_2\text{Nb}_4\text{O}_{13}$ was performed by combining a stoichiometric mixture of reagent-grade Na_2CO_3 , $\text{Ca}(\text{NO}_3)_2$, and Nb_2O_5 in a mortar and pestle and grinding for 30 min prior to the addition of either the NaCl or Na_2SO_4 flux in flux-to-reactant molar ratios of 5:1 and 20:1. After grinding, the reactant mixtures were then placed inside alumina crucibles and heated to 1100°C inside a box furnace at a rate of $50^\circ\text{C}/\text{h}$ for a reaction time of 10 h, and then cooled to 700°C at a rate of $5^\circ\text{C}/\text{h}$. The products were then allowed to radiatively cool to room temperature. The crystalline products were removed and washed with hot deionized water to remove the flux. Transparent crystals of $\text{Na}_2\text{Ca}_2\text{Nb}_4\text{O}_{13}$ were obtained in high purity, as judged from powder X-ray diffraction.

High-resolution Powder X-ray Diffraction (PXRD) data of all products were collected on an INEL diffractometer using $\text{CuK}\alpha_1$ ($\lambda = 1.54056\text{\AA}$) radiation from a sealed-tube X-ray generator (35kV, 30mA) using a curved position sensitive detector (CPS120). Lattice constants of all samples were refined using the JADE program. Field-emission scanning electron microscopy analyses were performed on a JEOL SEM 6400, and concomitantly the energy dispersive X-ray (EDX) spectra were taken to identify elemental compositions. UV-Vis diffuse reflectance spectra (DRS) were collected for all samples on a Shimadzu UV-3600 spectrophotometer equipped with an integrating sphere. BET surface area analyses were performed using a Quantachrome ChemBET Pulsar TPR/TPD.

2.2. Photocatalysis Testing.

The photocatalytic activity for H₂ formation was measured using an outer-irradiation type fused-silica reaction cell with a volume of 90 mL and irradiated under ultraviolet light ($\lambda > 300$ nm). First, each sample was loaded with a 1 wt% Pt cocatalyst using one of two well-known methods, by photochemical deposition (PCD) and via incipient wetness impregnation (IWI).^{19,20} Numerous previous studies have shown that platinum islands on a metal oxide surface can function as a kinetic aid to the reduction of H₂O to give H₂.²¹ In a typical PCD experiment, 100mg of Na₂Ca₂Nb₄O₁₃ is mixed with 30mL of an aqueous solution of dihydrogen hexachloroplatinate(IV) (H₂PtCl₆·6H₂O; Alfa Aesar, 99.95%), and then irradiated for 2 h using a 400W Xe arc-lamp with constant stirring using a magnetic stir bar. Approximately 1-2mL of MeOH is added prior to the reaction to aid platinum reduction onto the surface of the catalyst. UV-Vis measurements of the remaining solution confirmed a complete deposition of the platinum cocatalyst. After photoplatinization, the particles were separated via centrifugation, washed with distilled water to remove any remaining Cl⁻ ions, and then dried overnight in an oven at 80°C. For the IWI method comparison, 100mg of catalyst is brought to incipient wetness in an evaporating dish by a solution of H₂PtCl₆·6H₂O. The slurry is stirred and slowly evaporated in a water bath. The dried powder is then calcined at 400° C for 4h inside a box furnace, and then stored in air. For the photocatalytic H₂ measurements, the platinized Na₂Ca₂Nb₄O₁₃ was then added to the fused-silica reaction vessel that was filled with a 20% aqueous methanol solution. The added methanol functions as a hole scavenger, thereby generating CO₂ from its photo-oxidation, and which allows the measurement of the H₂ formation rate alone without the typically more difficult concomitant

formation of O₂ being necessary and potentially rate limiting.²² The net balanced reaction is: CH₃OH + H₂O → 3 H₂ + CO₂. The Na₂Ca₂Nb₄O₁₃ particles were first stirred in the dark for ~ 20 – 30 min , in order to remove any trapped gases on the particles' surfaces. Next, the reaction cell was irradiated under constant stirring for 12 h using an external 1000 W Xe arc-lamp equipped with an IR water filter and cooled using an external fan. The outlet of the photoreaction vessel was connected to a small horizontal quartz tube that trapped the evolved gases, and contained a moveable liquid bubble that allowed a volumetric determination of the amount of evolved gases at a constant pressure. The Na₂Ca₂Nb₄O₁₃ samples exhibited the formation of copious amounts of gases that rose to the top of the reaction cell, and that was observed to be consistent with the movement of the liquid bubble. The progress of the photocatalytic reactions was marked every hour and used to calculate the amount of gases generated in μmol H₂·g⁻¹·h⁻¹. The trapped gases were manually injected into a gas chromatograph (SRI MG #2; helium ionization and thermal conductivity detectors) in order to confirm the generated gases as H₂ and CO₂. The Apparent Quantum Yield (AQY) was measured using a reaction cell containing 0.15g of the suspended platinized catalyst and 75 mL of a 20% MeOH_(aq) solution irradiated using the 1000W Xe Arc Lamp equipped with an IR filter and 350 nm bandpass filter (Newport Oriel).

$$\text{AQY (\%)} = \{[\text{number of reacted electrons}] / [\text{number of incident photons}]\} \times 100^{19,23}$$

The number of reacted electrons was determined from the volume of evolved H₂. The number of incident photons was determined by ferrioxalate actinometry.²⁴

3. Results and Discussion

$\text{Na}_2\text{Ca}_2\text{Nb}_4\text{O}_{13}$ is the $n=4$ member of the Ruddlesden-Popper type perovskite belonging to the orthorhombic crystal system with space group $Immm$. The n corresponds to the thickness of the perovskite layers, while the interlayer structure is composed of Na and O atoms (shown in Figure 3.1).¹⁵ Both NaCl and Na_2SO_4 were chosen as a flux based upon previous successful reports of synthesis of layered perovskite materials as well as its low cost ease of removal after the reaction.^{5,15-18} Small flat platelet crystals formed quite well with the Na_2SO_4 flux and were visible to the naked eye while the products formed using the NaCl flux appeared as a white homogeneous powder. Figure 3.2 shows the PXRD patterns of flux prepared products. Several peaks corresponding to the [001] direction were diminished due to preferred orientation of the crystals. X-ray characterization was carried out further using a capillary loaded sample on a Rigaku X-ray diffractometer, which confirmed complete formation of the crystalline products. Refined lattice parameters were calculated for all samples using JADE software, reporting the following lattice range ($a = 3.8918 - 3.9000 \text{ \AA}$), ($b = 3.8820 - 3.8842 \text{ \AA}$), and ($c = 36.127 - 36.132 \text{ \AA}$) (See Supporting Information). An EDX analysis was also performed on $\text{Na}_2\text{Ca}_2\text{Nb}_4\text{O}_{13}$ samples in order to confirm the elemental compositions which are provided in the Supporting Information. The spectra revealed Na, Ca, Nb, and O in their approximate stoichiometric molar ratios. There was no significant detection of any S or Cl, indicating the fluxes had been removed completely by the washing.

Field-emission SEM was employed to evaluate the size and shape of the $\text{Na}_2\text{Ca}_2\text{Nb}_4\text{O}_{13}$ particles. Figure 3.3 displays several images of the NaCl flux-prepared

samples. SEM observations of both the 5:1 and 20:1 Flux: $\text{Na}_2\text{Ca}_2\text{Nb}_4\text{O}_{13}$ samples revealed long thin flat rods approximately $\sim 350 - 650$ nm across and $\sim 1,000 - 6,000$ nm long with widths of ~ 30 nm that aggregated into larger clumps. While the larger aggregates contained many surface features due to the collection of smaller particles, the surfaces of the individual rods remained relatively flat with some edges and nanosteps that cleaved at a 90° angle, relative to their orthorhombic symmetry. The 20:1 NaCl flux prepared samples appeared largely the same although the lengths of some of the rods were slightly larger, ranging from approximately $\sim 1,000 - 10,000$ nm in length. The Na_2SO_4 flux prepared samples largely contained contrasting particle formation, and are shown collectively in Figure 3.4. Both the 5:1 and 20:1 Na_2SO_4 flux samples yielded large flat platelets, while the 5:1 Na_2SO_4 sample also contained a small observable amount of thin flat rod aggregates. The thin rods were similar in shape to those found in the NaCl flux samples, but whose thicknesses were observed to be slightly greater, approximately ~ 100 nm on average. The large flat platelets ranged in sizes from $\sim 50 - 200$ μm , with thicknesses ranging approximately ~ 500 nm to nearly 10 μm in size. The surfaces of the plates were largely flat, but several nanosteps and grooves that are consistent with the layered structure were observed along the edges of all the platelets, with the individual nanosteps ranging typically $\sim 10 - 30$ nm in thickness. The 20:1 Na_2SO_4 samples revealed exclusively large flat platelets similar to those observed in the 5:1 Na_2SO_4 sample but appearing much larger, ranging in size from $\sim 80 - 350$ μm , with thicknesses ranging approximately $5 - 25$ μm . The surfaces of these large platelets were also relatively flat, as was with those observed in the 5:1 Na_2SO_4 sample, but along the edges contained several nanosteped features and grooves corresponding to the crystal layers and approximately $10 - 120$ nm in width.

The deposition location of a platinum cocatalyst plays a key role in improving the photocatalytic activity of a metal oxide catalyst. It is well known that Pt^{4+} will undergo a reduction to Pt^0 metal during the photodeposition reaction, and therefore likely will deposit at or near sites of higher electron density.^{25,26} By observing where the largest amounts of platinum are being deposited could reveal a deeper understanding of the nature of photocatalysis by exposing the most active sites of the particles. FESEM imaging was again used to observe platinum deposits on $\text{Na}_2\text{Ca}_2\text{Nb}_4\text{O}_{13}$ after the samples had been loaded with a 1% wt. platinum cocatalyst using both the PCD method and via IWI. Figure 3.5 shows the platinized products of the 20:1 Na_2SO_4 sample prepared using the PCD method. Small platinum islands have formed on the surface and which these formations were not observed on any SEM images of the samples taken before the platinum deposition took place. The platinum islands appear to have deposited near or along edges, grooves, and defects of the particle surface (3.5B-D), and little or no deposition is observed on the exposed faces of the crystal (3.5A), suggesting anisotropy regarding the electron migration pathway within the crystal during photo-excitation. Therefore, it is likely the nanofeatures of the particles, including the edges, steps, and grooves, that are the most active sites for photodeposition of the platinum cocatalyst onto the particle surface. Figure 3.6 shows FESEM images of the 5:1 Na_2SO_4 sample taken after a 1% Pt deposition via incipient wetness impregnation. The Pt islands are distributed generally evenly on all surfaces of the particle. There were no observed sites of preferential deposition of Pt as compared to the photodeposited samples. During the IWI process, chloroplatinic acid molecules will physically adsorb to all surfaces of the $\text{Na}_2\text{Ca}_2\text{Nb}_4\text{O}_{13}$ particles, and then is calcined at 400°C where the Pt islands will attach

at their respective adsorption sites, and which does not require electron excitation from incident light to reduce the Pt particles, therefore preferential site deposition will not be observed as in the PCD method.

Measurements of the UV-Vis Diffuse Reflectance Spectra (DRS) were taken on all flux-synthesized $\text{Na}_2\text{Ca}_2\text{Nb}_4\text{O}_{13}$ samples in order to determine their optical bandgap sizes, shown in Figure 3.7. The reflectance has been converted to absorbance using the Kubelka-Munk function. In all cases, the optical bandgaps were calculated to be within a range of ~ 3.3 eV, based on the onset of absorption. These values are in agreement with similar UV-active layered niobate photocatalysts.^{11,12}

To observe the photocatalytic water-splitting process, irradiated photons of bandgap or greater energies must excite electrons in a semiconductor to create electron/hole pairs, which can then both oxidize and reduce water into O_2 and H_2 , respectively. In these experiments CH_3OH was employed as a sacrificial reagent to observe only the H_2 half reaction separately, without the more difficult water oxidation step. The flux syntheses of different particle sizes and morphologies should impact the rates of these reactions. Figure 3.8 shows the time course evolution of H_2 from the $\text{Na}_2\text{Ca}_2\text{Nb}_4\text{O}_{13}$ products after platinization by the PCD method, and the rates from both the PCD and IWI methods and BET surface area calculations are listed in Table 3.1. In all cases, activity was observed for the entire duration of exposure to UV irradiation. The highest observed rate of H_2 production was $1355 \mu\text{mol H}_2 \cdot \text{g}^{-1} \cdot \text{h}^{-1}$ for the 5:1 NaCl flux prepared samples using the PCD method and which also had the highest measured surface area and smallest observed particle sizes. The apparent quantum yield of the 5:1 NaCl PCD prepared sample was 6.5% at 350 nm, and is

relatively similar in comparison to other known layered niobate photocatalysts.²⁷ Contrastingly, the lowest PCD observed rate of H₂ production was 230 μmol H₂·g⁻¹·h⁻¹ for the 5:1 Na₂SO₄ flux prepared samples and which also had a lower measured surface area and larger observed particle sizes. The 20:1 Na₂SO₄ flux prepared particles produced H₂ at a rate of 447 μmol H₂·g⁻¹·h⁻¹, yet had a lower surface area than the 5:1 Na₂SO₄ flux sample. This is likely due to the greater number of nanosteps and defects observed from the SEM data, indicating a greater region of active surface area, in which the photocatalytic reduction of water at the cocatalyst deposit sites is occurring. Compared to the PCD method, the IWI method yielded lower activity rates in all Na₂Ca₂Nb₄O₁₃ samples, but the corresponding trend in activity is similar. The highest observed IWI rate was 1099 μmol H₂·g⁻¹·h⁻¹ for the 5:1 NaCl flux prepared samples, and the lowest was 113 μmol H₂·g⁻¹·h⁻¹ for the 20:1 Na₂SO₄ flux prepared samples, and which had the highest and lowest measured surface areas, respectively. This data shows that the PCD method, in which the Pt nanoislands preferentially desposited along edges and defects, results in greater overall photocatalytic activity versus a more general Pt island distribution as was observed in the SEM data for the IWI prepared samples. In all cases, the evolution activity of the NaCl flux prepared samples outperformed the rates observed in the Na₂SO₄ flux prepared particles. As the amount of flux used in the synthesis reaction increased, the surface area and photocatalytic activity generally decreased. This is likely due to an increased number of exposed active sites, in good agreement with the SEM images of the platinized Na₂Ca₂Nb₄O₁₃ particles. It has been previously reported that nanosteped features have contributed to higher rates of activity in photocatalysts and also help to inhibit recombination effects.^{28,29} Our recently concluded

studies on related metal-oxide photocatalysts also show similar results with respect to the relationship between platinum deposition, particle surface area and photocatalytic activity.^{30,31} It is indeed likely that the nano-features and edges observed in $\text{Na}_2\text{Ca}_2\text{Nb}_4\text{O}_{13}$ exhibit a similar effect in its photocatalytic activities.

4. Conclusions

The photocatalyst $\text{Na}_2\text{Ca}_2\text{Nb}_4\text{O}_{13}$ can be prepared in either a NaCl or Na_2SO_4 flux at 1100°C for 10 h with slow cooling and yield either long thin rods or large flat platelets ranging in size from $\sim 350 - 10,000$ nm and $\sim 50 - 350$ μm in size, respectively. A measured optical bandgap of $\text{Na}_2\text{Ca}_2\text{Nb}_4\text{O}_{13}$ was determined to be 3.3 eV by UV-Vis diffuse reflectance. Platinum islands photodeposited onto the samples largely deposited onto edges and nanosteps, exposing the most active sites of the particles, while a more general distribution of Pt nanoislands was observed when deposited via incipient wetness impregnation. UV-light photocatalytic H_2 rates of the $\text{Na}_2\text{Ca}_2\text{Nb}_4\text{O}_{13}$ particles in aqueous MeOH solution ranged from $230 - 1355$ $\mu\text{mol H}_2 \cdot \text{g}^{-1} \cdot \text{h}^{-1}$ when a platinum cocatalyst was deposited by the PCD method and $113 - 1099$ $\mu\text{mol H}_2 \cdot \text{g}^{-1} \cdot \text{h}^{-1}$ when platinum was deposited by the IWI method. Higher rates were correlated with greater preferential deposition of platinum islands near and along surface edges, nanosteps, and defects, as well as with higher surface area and a greater number of exposed active sites. Thus, the results demonstrate the value of flux synthetic methods in tuning particle sizes and surface microstructures in order to probe the origins of photocatalytic activity on the surfaces of metal-oxide particles.

5. Acknowledgements

Financial support of this research is acknowledged from the Chemical Sciences, Geosciences and Biosciences Division, Office of Basic Energy Sciences, Office of Science, U.S. Department of Energy (DE-FG02-07ER15914).

6. Supporting Information

Refined lattice parameters, and EDS results for composition analysis.

7. References

- (1) Lewis, N. S.; Nocera, D. G. *Proceedings of the National Academy of Sciences* **2006**, *103*, 15729.
- (2) Kudo, A. *The journal of physical chemistry. B* **2000**, *104*, 571.
- (3) Kato, H.; Kudo, A. *J. Photochem. Photobiol., A* **2001**, *145*, 129.
- (4) Hyun G. Kim, D. W. H., et. al *Chemical Communications* **1999**, *12*, 1077.
- (5) Arney, D., Porter, Brittany; Greve, Benjamin; Maggard, P.A. *Journal of photochemistry and photobiology. A, Chemistry* **2008**, *199*, 230.
- (6) Sayama, K.; Arakawa, H.; Domen, K. *Catal. Today* **1996**, *28*, 175.
- (7) El-Toni, M. A.; Yin, S.; Sato, T. *Materials letters* **2006**, *60*, 185.
- (8) Aboujalil, A.; Deloume, J.-P.; Chassagneux, F.; Scharff, J.-P.; Durand, B. *J. Mater. Chem.* **1998**, *8*, 1601.
- (9) Porob, D. G.; Maggard, P. A. *Materials Research Bulletin* **2006**, *41*, 1513.
- (10) Porob, D. G.; Maggard, P. A. *Journal of Solid State Chemistry* **2006**, *179*, 1727.
- (11) Maeda, K.; Mallouk, T. E. *J. Mater. Chem.* **2009**, *19*, 4813.
- (12) Maeda, K.; Eguchi, M.; Youngblood, W. J.; Mallouk, T. E. *Chem. Mater.* **2009**, *21*, 3611.
- (13) Ebina, Y.; Sasaki, T.; Harada, M.; Watanabe, M. *Chem. Mater.* **2002**, *14*, 4390.
- (14) Domen, K.; Ebina, Y.; Sekine, T.; Tanaka, A.; Kondo, J.; Hirose, C. *Catal. Today* **1993**, *16*, 479.

- (15) Chiba, K.; Ishizawa, N.; Nagai, Y.; Oishi, S. *Solid State Ionics* **1998**, *108*, 179.
- (16) Oishi, S. *Chemistry letters* **1998**, *5*, 439.
- (17) Chiba, K.; Ishizawa, N.; Oishi, S. *Acta Crystallogr., Sect. C: Cryst. Struct. Commun.* **1999**, *C55*, 1041.
- (18) Oishi, S. *Chemistry letters* **1999**, *10*, 1011.
- (19) Kato, H.; Asakura, K.; Kudo, A. *J. Am. Chem. Soc.* **2003**, *125*, 3082.
- (20) Sreethawong, T.; Yoshikawa, S. *Int. J. Hydrogen Energy* **2006**, *31*, 786.
- (21) Nakamatsu, H. *J. Chem. Soc., Faraday Trans. 1* **1985**, *82*, 527.
- (22) Graetzel, M. E. *Energy Resources through Photochemistry and Catalysis*; Academic Press: New York, NY, 1983.
- (23) Kudo, A.; Miseki, Y. *Chemical Society Reviews* **2009**, *38*, 253.
- (24) Hatchard, C. G.; Parker, C. A. *Proc. R. Soc. London, Ser. A* **1956**, *235*, 518.
- (25) Kraeutler, B.; Bard, A. J. *J. Am. Chem. Soc.* **1978**, *100*, 4317.
- (26) Ohtani, B.; Iwai, K.; Nishimoto, S.-i.; Sato, S. *J. Phys. Chem. B* **1997**, *101*, 3349.
- (27) Hwang, D. W. *Journal of catalysis* **2000**, *193*, 40.
- (28) Kudo, A.; Kato, H.; Tsuji, I. *Chemistry letters* **2004**, *33*, 1534.
- (29) Kudo, A.; Kato, H. *Chemical Physics Letters* **2000**, *331*, 373.
- (30) Arney, D., Hardy, Christopher; Greve, Benjamin; Maggard, Paul A. *Journal of photochemistry and photobiology. A, Chemistry* **2010**, *In Press*.
- (31) Arney, D.; Watkins, T.; Maggard, P. A. *Journal of the American Ceramic Society* **2011**, *94*, 1483.

Table 3.1. Measured photocatalytic rates of H₂ formation for flux-prepared Na₂Ca₂Nb₄O₁₃ particles deposited with a 1% wt. Pt cocatalyst by photochemical deposition (PCD) and incipient wetness impregnation (IWI) methods.

<u>Sample</u>	<u>Flux:</u> <u>Na₂Ca₂Nb₄O₁₃</u> <u>Ratio</u>	<u>Surface</u> <u>Area</u> <u>(m²/g)</u>	<u>PCD</u> <u>Activity</u> <u>(μmol H₂/g-h)</u>	<u>IWI</u> <u>Activity</u> <u>(μmol H₂/g-h)</u>
Na ₂ Ca ₂ Nb ₄ O ₁₃ A	5:1 NaCl	4.6	1355	1099
Na ₂ Ca ₂ Nb ₄ O ₁₃ B	20:1 NaCl	3.9	835	539
Na ₂ Ca ₂ Nb ₄ O ₁₃ C	5:1 Na ₂ SO ₄	1.6	230	204
Na ₂ Ca ₂ Nb ₄ O ₁₃ D	20:1 Na ₂ SO ₄	0.36	447	113

Testing Conditions: Outer irradiation 1000 W high-pressure Xe arc-lamp, 150 mg of Na₂Ca₂Nb₄O₁₃, 20% MeOH_(aq) and 1 wt% Pt surface cocatalyst.

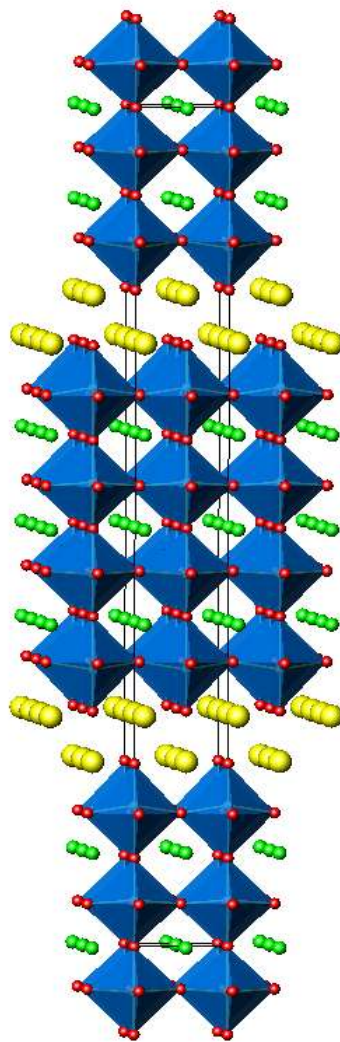


Figure 3.1. Structure of $\text{Na}_2\text{Ca}_2\text{Nb}_4\text{O}_{13}$. NbO_6 octahedra are shown in blue, Ca atoms shown in green, and Na atoms in yellow. Space Group Immm.

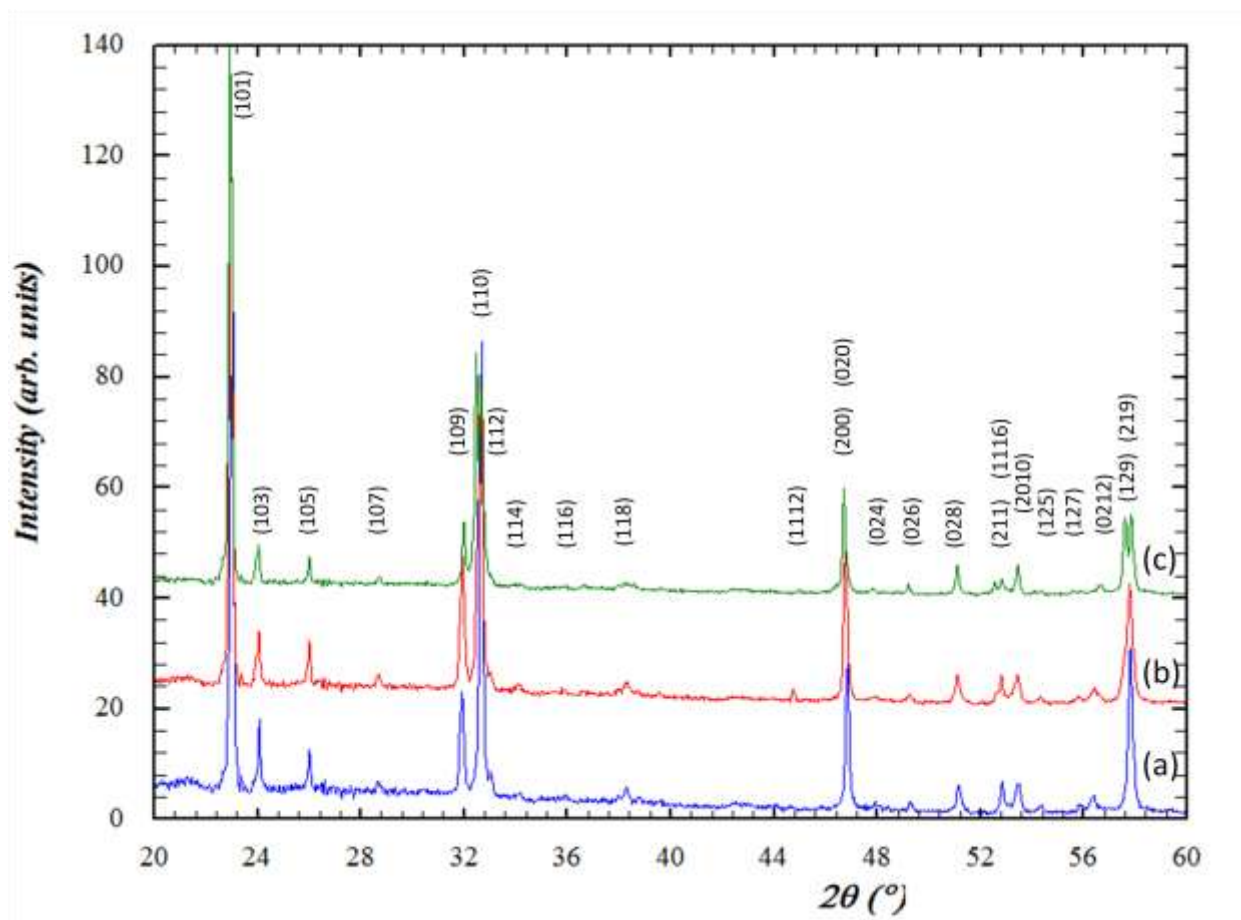


Figure 3.2. PXR D Patterns of $\text{Na}_2\text{Ca}_2\text{Nb}_4\text{O}_{13}$ prepared using (a) 5:1 NaCl flux ratio, (b) 5:1 Na_2SO_4 flux ratio and (c) 20:1 Na_2SO_4 flux ratio.

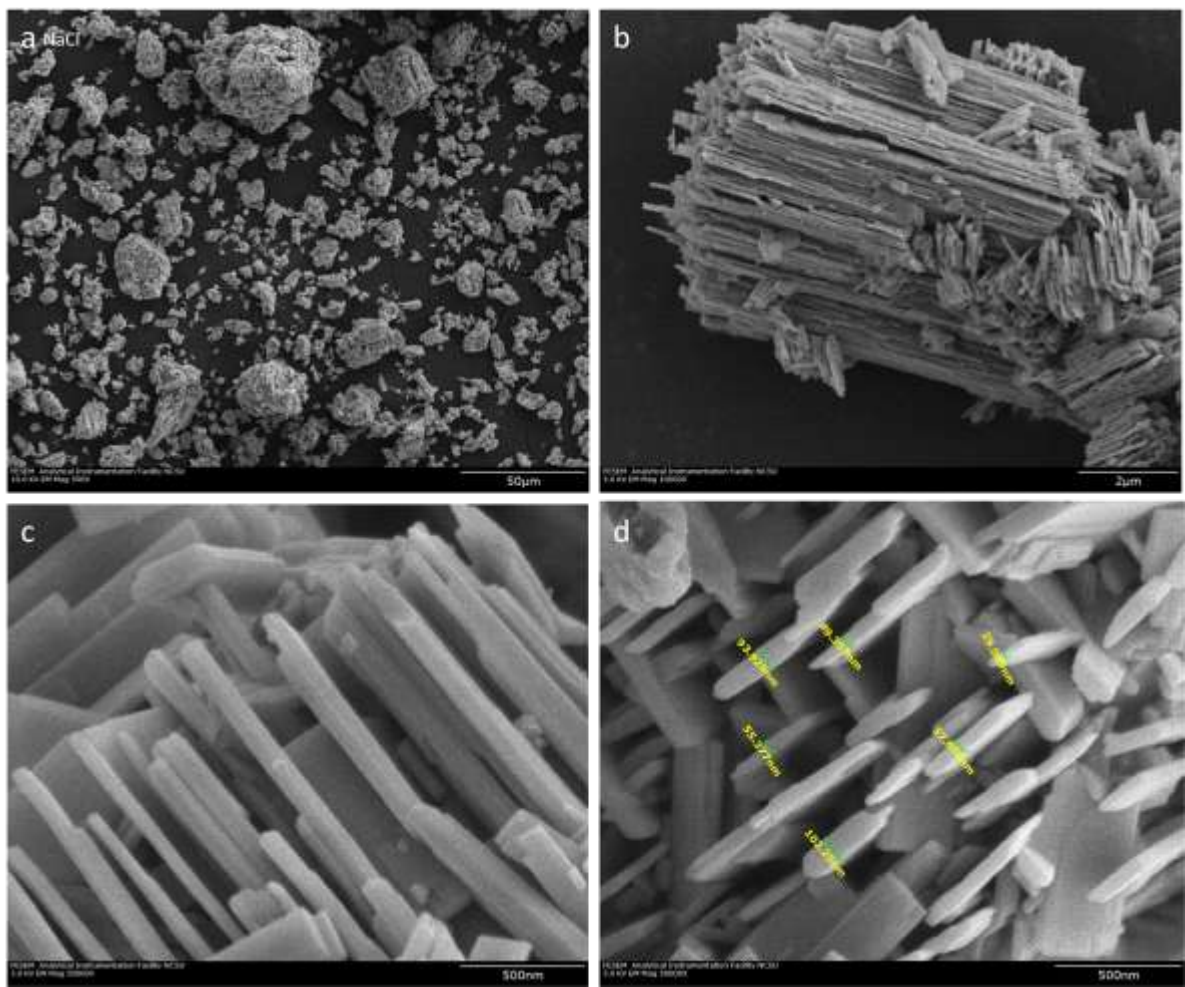


Figure 3.3. FESEM Images of $\text{Na}_2\text{Ca}_2\text{Nb}_4\text{O}_{13}$ aggregate rods prepared from a NaCl flux.

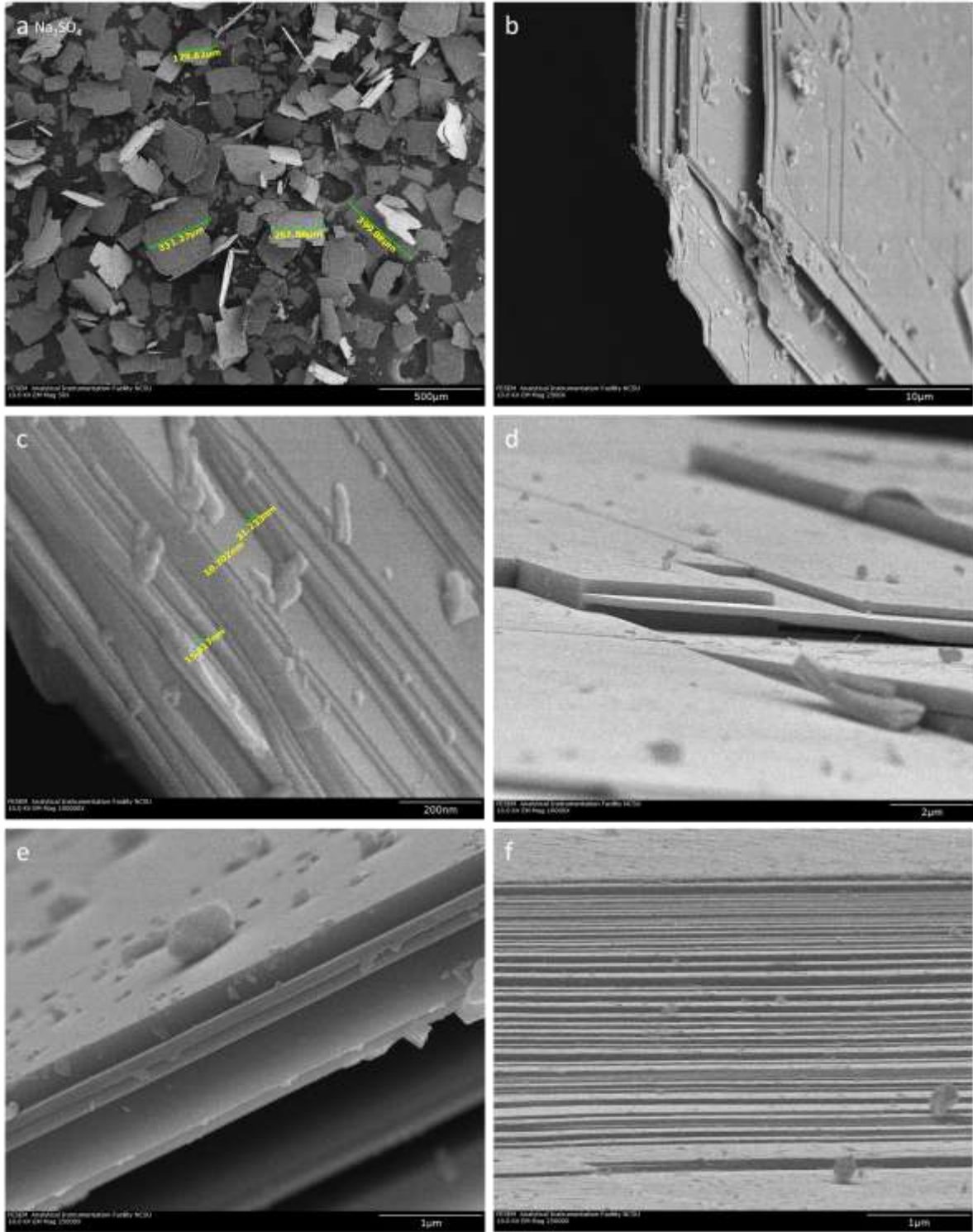


Figure 3.4. FESEM Images of $\text{Na}_2\text{Ca}_2\text{Nb}_4\text{O}_{13}$ platelet particles prepared from a Na_2SO_4 Flux.

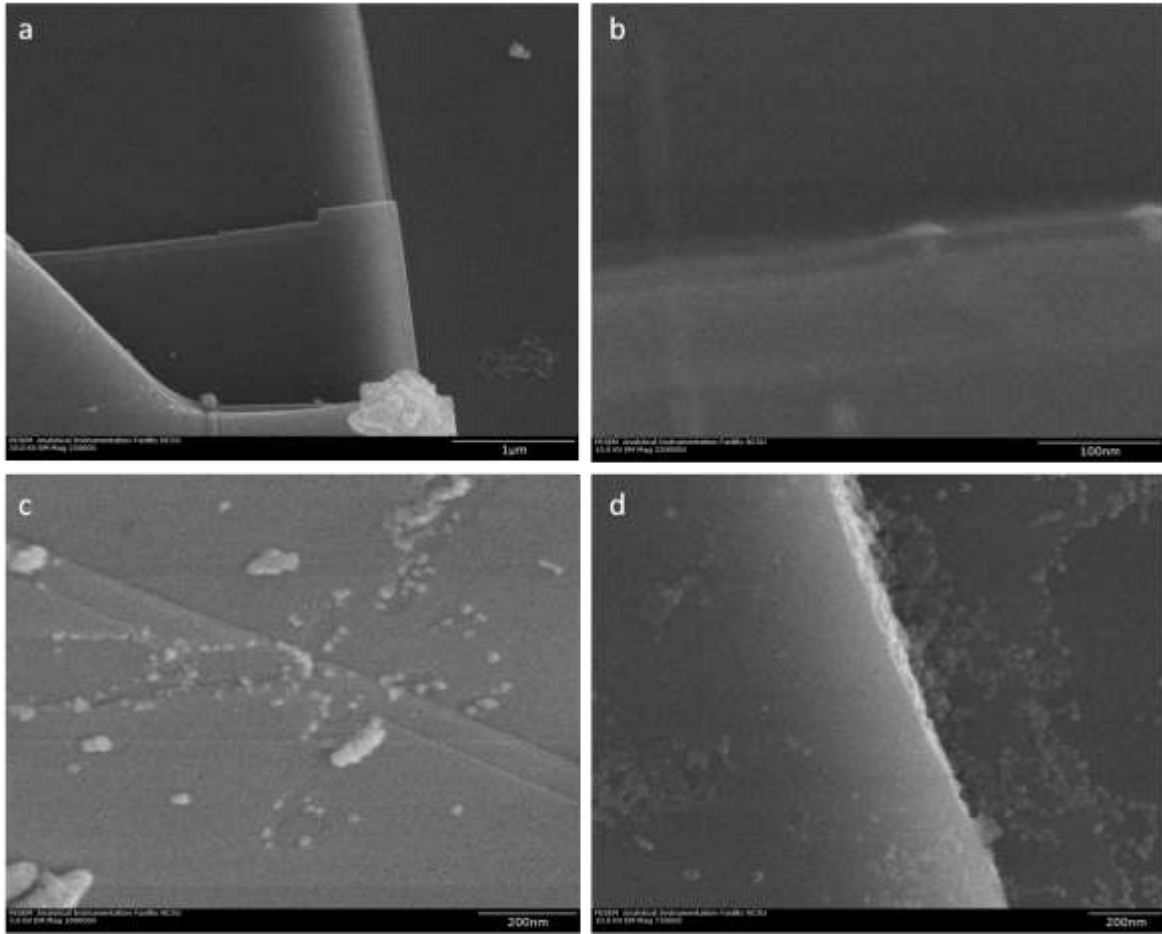


Figure 3.5. FESEM Images of the 20:1 Na_2SO_4 flux prepared $\text{Na}_2\text{Ca}_2\text{Nb}_4\text{O}_{13}$ sample deposited with a 1% Pt Cocatalyst by the PCD method.

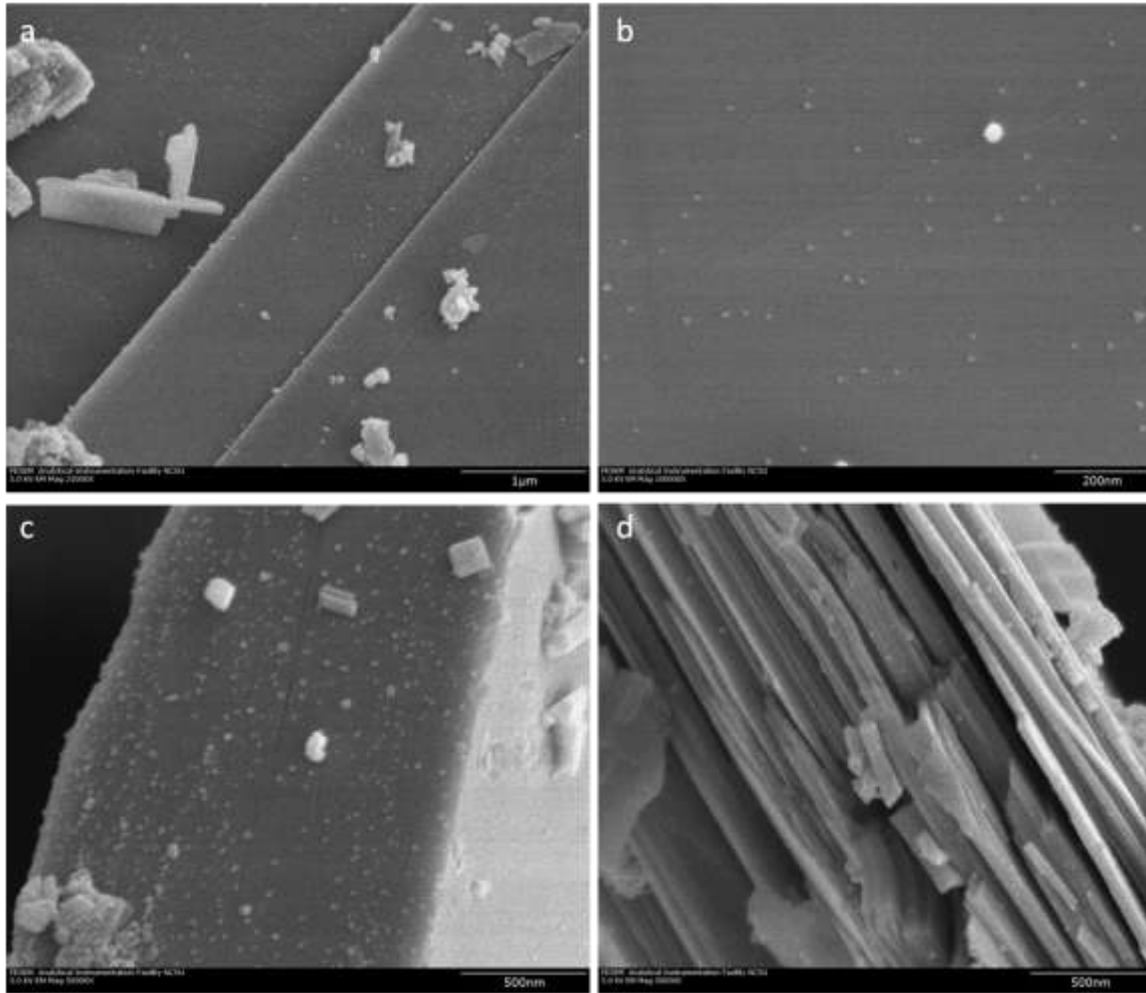


Figure 3.6. FESEM Images of the 5:1 Na_2SO_4 flux prepared $\text{Na}_2\text{Ca}_2\text{Nb}_4\text{O}_{13}$ sample with a 1% Pt cocatalyst deposited via IWI method.

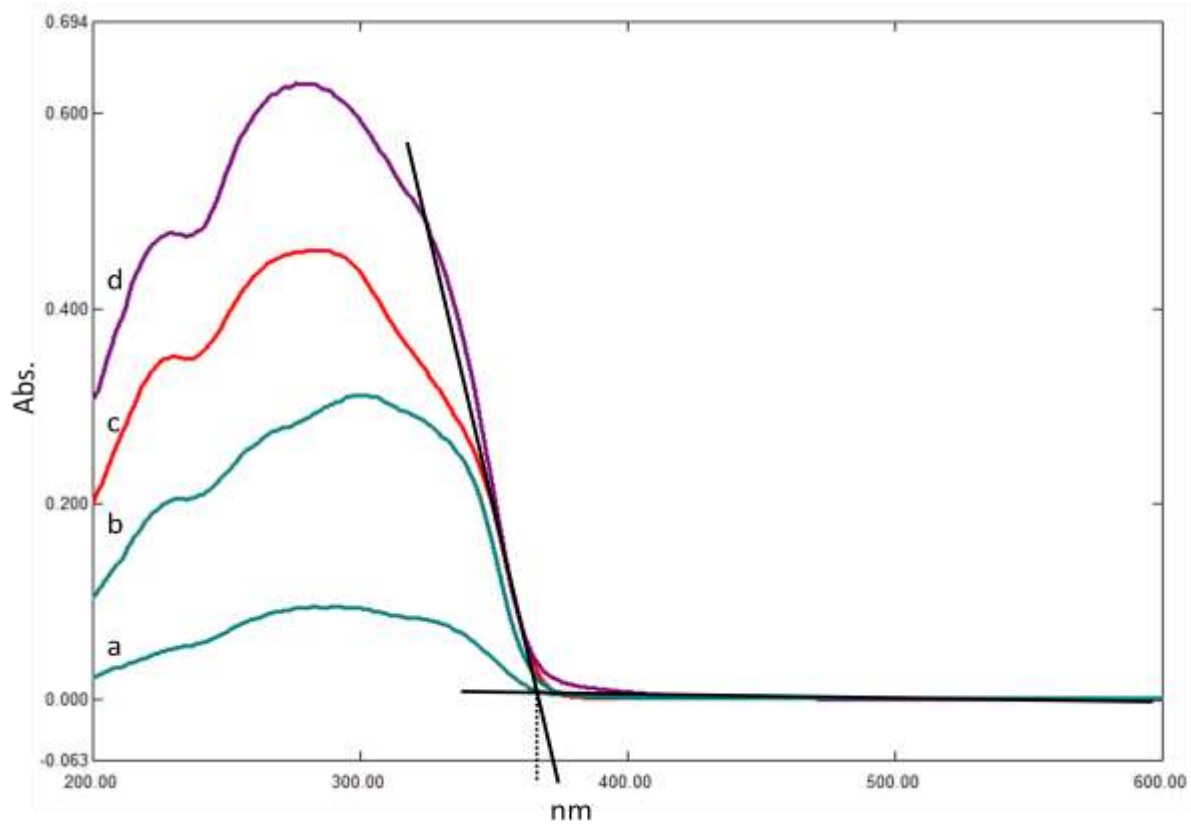


Figure 3.7. UV-Vis Diffuse Reflectance Measurements for $\text{Na}_2\text{Ca}_2\text{Nb}_4\text{O}_{13}$ prepared using a (a) 5:1 NaCl Flux, (b) 5:1 Na_2SO_4 flux, (c) 20:1 Na_2SO_4 flux, and (d) 20:1 NaCl flux molar ratio.

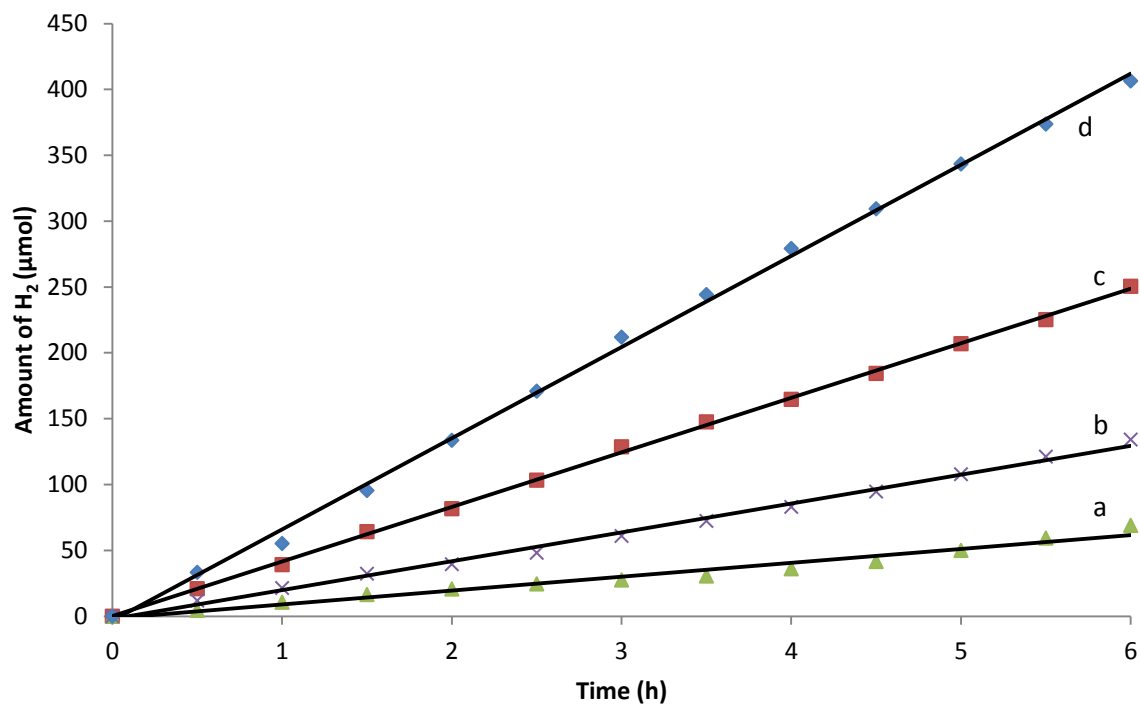


Figure 3.8. Photocatalytic formation of hydrogen versus time for flux-prepared $\text{Na}_2\text{Ca}_2\text{Nb}_4\text{O}_{13}$ using a (a) 5:1 Na_2SO_4 flux, (b) 20:1 Na_2SO_4 flux, (c) 20:1 NaCl flux, and (d) 5:1 NaCl flux. Catalyst prepared with 1% wt Pt cocatalyst deposited by the PCD method.

Supplemental Information

“Particle Size Control and Photocatalytic H₂ Production From Na₂Ca₂Nb₄O₁₃ Crystals Grown From a Molten Flux”

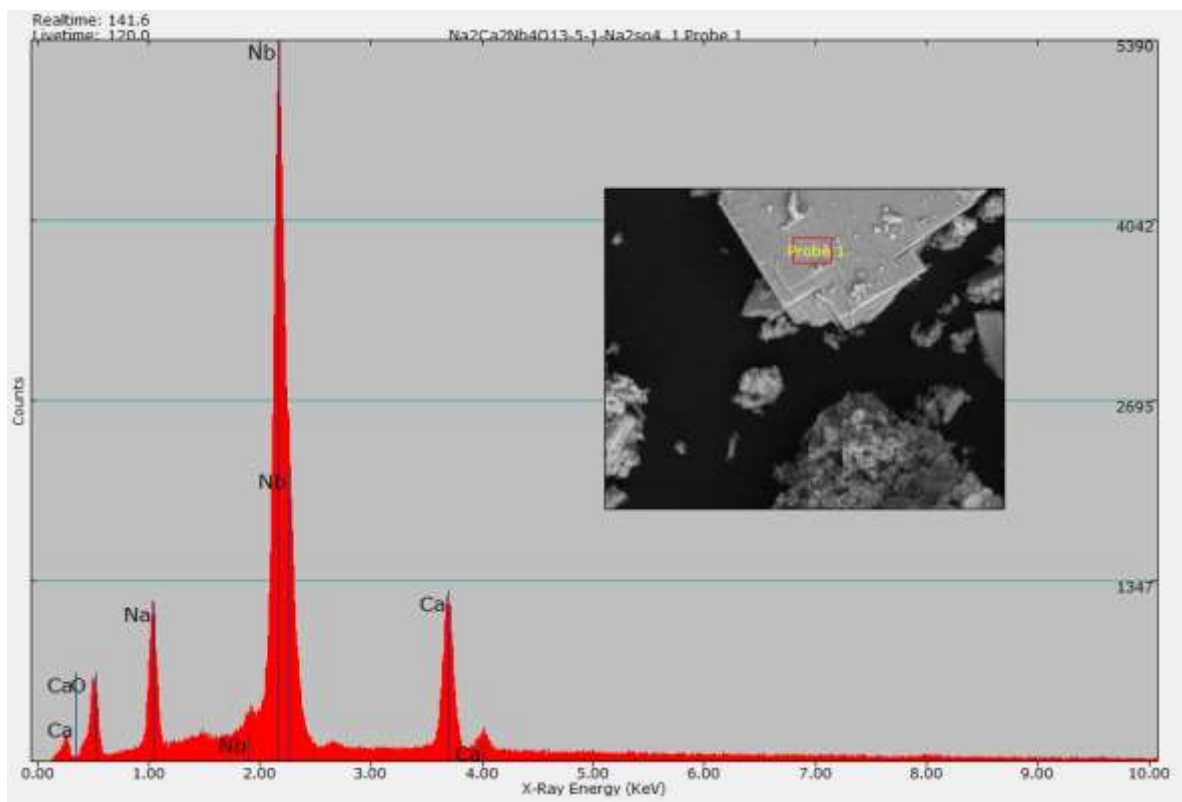
David Arney and Paul A. Maggard*

Table 3.S1. Refined cell parameters^a for Na₂Ca₂Nb₄O₁₃ prepared by NaCl and Na₂SO₄ flux methods.

<u>Na₂Ca₂Nb₄O₁₃</u>			
<u>Flux</u>			
<u>Conditions</u>	<u><i>a</i> (Å)</u>	<u><i>b</i> (Å)</u>	<u><i>c</i> (Å)</u>
5:1 NaCl	3.900(1)	3.882(5)	36.127(13)
20:1 NaCl	3.893(1)	3.884(1)	36.132(5)
5:1 Na ₂ SO ₄	3.8918(8)	3.8842(8)	36.128(10)
20:1 Na ₂ SO ₄	3.8936(7)	3.882(1)	36.129(6)

^a Unit cell parameters were refined using the program JADE

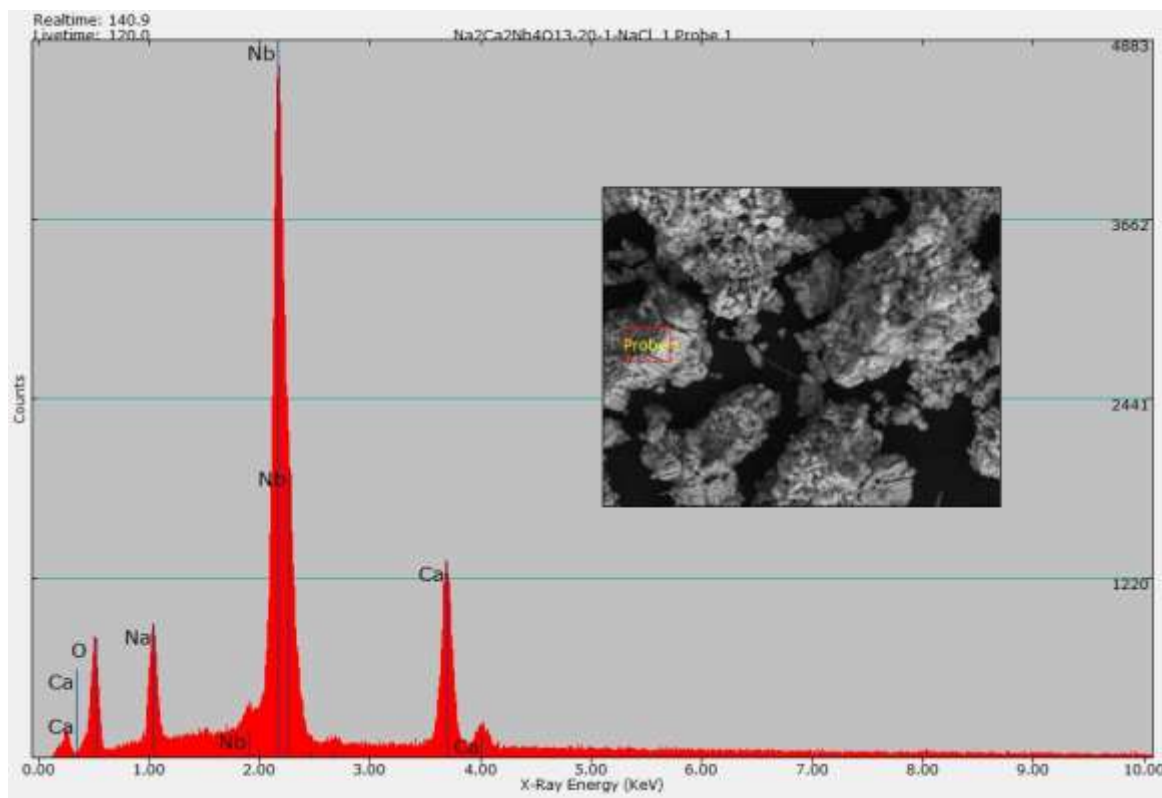
Figure 3.S1. EDX Spectra showing the elemental composition of $\text{Na}_2\text{Ca}_2\text{Nb}_4\text{O}_{13}$ prepared using a 5:1 Na_2SO_4 flux: $\text{Na}_2\text{Ca}_2\text{Nb}_4\text{O}_{13}$ molar ratio.



Element	Weight %	Std. Dev.	Atomic %	FWHM (eV)	ROI (net)
O	16.69	1.01	40.09	69.7	3671.03
Na	14.53	0.86	24.27	78.2	5415.47
S?	0.1	0.04	0.12	95.6	13208.42
Ca	13.06	0.75	12.52	111.5	9004.09
Nb	55.63	1.39	23	93.9	35203.39
Total	100				

? This element is statistically insignificant

Figure 3.S2. EDX Spectra showing the elemental composition of $\text{Na}_2\text{Ca}_2\text{Nb}_4\text{O}_{13}$ prepared using a 20:1 NaCl flux: $\text{Na}_2\text{Ca}_2\text{Nb}_4\text{O}_{13}$ molar ratio.



Element	Weight %	Std. Dev.	Atomic %	FWHM (eV)	ROI (net)
O	19.32	1.07	44.17	69.7	4849.22
Na	13.58	0.82	21.61	78.2	5838.84
Ca	15.01	0.81	13.7	111.5	11958
Nb	52.09	1.3	20.51	93.9	38663.43
Total	100				

PART 2. VISIBLE-LIGHT ACTIVE PHOTOCATALYSTS

CHAPTER 4

Flux Synthesis of AgNbO₃: Effect of Particle Surfaces and Sizes on Photocatalytic Activity

An amended paper published in the Journal of Photochemistry and Photobiology A:

Chemistry

Journal of Photochemistry and Photobiology A: Chemistry **2010** 214, 54-60

David Arney, Christopher Hardy, Benjamin Greve, and Paul A. Maggard*

Department of Chemistry, North Carolina State University, Raleigh, NC 27695

Abstract

The molten-salt flux synthesis of AgNbO₃ particles was performed in a Na₂SO₄ flux using 1:1, 2:1 and 3:1 flux-to-reactant molar ratios and heating to 900°C for reaction times of 1 – 10 h. Rectangular-shaped particles are obtained in high purity and with homogeneous microstructures that range in size from ~100 – 5,000nm and with total surface areas from 0.16 – 0.65 m²·g⁻¹. The smallest particle-size distributions and highest surface areas were obtained for the largest amounts of flux (3:1 ratio) and the shortest reaction time (1h). Measured optical bandgap sizes of the AgNbO₃ products were in the range of ~2.8 eV. The photocatalytic activities of the AgNbO₃ particles for H₂ formation were measured in visible light ($\lambda > 420\text{nm}$) in an aqueous methanol solution and varied from ~1.7 – 5.9 $\mu\text{mol H}_2\cdot\text{g}^{-1}\cdot\text{h}^{-1}$. The surface microstructures of the particles were evaluated using field-emission SEM, and the highest photocatalytic rates of the AgNbO₃ particles were correlated with the formation of high densities of ~20-50 nm terraced surfaces. By comparison, the solid-state sample showed no well-defined morphology or microstructure. Thus, the results presented herein

demonstrate the utility of flux synthetic methods in targeting new particles sizes and surface microstructures for the enhancement and understanding of photocatalytic reactivity over metal-oxide particles.

Keywords: Flux synthesis; AgNbO₃; photocatalysis

Introduction

Photocatalytic hydrogen production from solar energy and water using metal-oxide particles is a rapidly expanding field of renewable energy research.¹⁻⁴ Numerous metal-oxides have been shown to split water into hydrogen and oxygen in aqueous solutions when irradiated by high-energy ultraviolet photons, including NaTaO₃, Sr₂Nb₂O₇, La₂Ti₂O₇, as well as many others.⁵⁻¹⁶ However, the highest intensities and greatest fraction (>50%) of the solar spectrum consist of visible-light wavelengths, and thus the synthesis of new photocatalysts that efficiently utilize visible-light photons for hydrogen production could help realize significant new technological advancements. Previously, it has been shown that Ag⁺-containing early transition-metal oxides can absorb light out to the visible wavelengths owing to their smaller bandgap sizes.¹⁷⁻¹⁹ This arises because of the higher-energy valence band that derives from the filled Ag 4*d* orbitals, and which is still sufficiently below the (O₂/H₂O) oxidation potential. Previous studies on AgNbO₃ and AgTaO₃ have shown that their bandgap sizes are ~2.8 eV and ~3.4 eV, respectively, and that the photon-driven oxidation and reduction of water is feasible in visible light using suitable sacrificial reagents.¹⁷ AgTaO₃ is reportedly inactive for the photocatalytic production of H₂ in visible

light owing to its larger bandgap size, but AgNbO_3 was found to be active in visible light using sacrificial reagents with low rates of $\sim 1.5 \mu\text{mol H}_2 \cdot \text{g}^{-1} \cdot \text{h}^{-1}$.¹⁷ However, the synthesis of AgNbO_3 and AgTaO_3 in these photocatalysis studies proceeded via traditional solid-state methods. This synthetic route provides almost no control over the particle sizes and/or surface characteristics of the metal-oxide particles where the photon-initiated oxidation and reduction reactions occur (i.e. the active sites of the reaction). Utilization of new synthetic methods to better gain control over the particle features of metal oxides can potentially enable a deeper understanding of these reactions. As an alternative synthetic method, the use of molten-salt flux techniques for the preparation of metal oxides can enable shorter reaction times, reduced reaction temperatures, and tunability of the particle features, such as their sizes and morphologies.^{20-25, 30}

Thus, new synthetic investigations into the preparation of AgNbO_3 particles by flux synthetic techniques were conducted in order to determine the roles the particle sizes and surfaces had in its photocatalytic activities. The flux synthesis of large single crystals of AgNbO_3 for X-ray analysis has been reported previously in the literature based on the use of AgCl and Ag_2SO_4 fluxes.^{26,27} However, the research motivation herein was to investigate flux-synthetic routes to much smaller particle sizes of AgNbO_3 , and to compare the resultant photocatalytic activities, surface areas, and particles sizes with those products obtained from traditional solid-state methods. Described herein is the synthesis of AgNbO_3 particles within a molten Na_2SO_4 flux, and an investigation of the effects of reaction durations and flux-to-reactant ratios on the particle sizes and morphologies, as well as their optical properties and photocatalytic rates for H_2 formation. The products were characterized by powder X-Ray

diffraction, UV-Vis diffuse reflectance spectroscopy, BET surface-area analysis, field-emission scanning electron microscopy, and their visible-light photocatalytic activities for H₂ production.

Experimental

2.1. Synthesis and Characterization. The flux synthesis of AgNbO₃ was performed by combining a well-ground stoichiometric mixture of Ag₂O and Nb₂O₅ and adding this to a Na₂SO₄ salt flux to give flux-to-reactant molar ratios of 1:1, 2:1, and 3:1. The reactant mixtures were then placed inside an alumina crucible and heated to 900°C inside a box furnace for reaction times of 1, 2, and 10 hours. The crucibles were allowed to radiatively cool to room temperature inside the furnace. Additionally, 1:1 flux-prepared samples were slow cooled to 750°C at rates of 15°C/h and 3°C/h, respectively, before then radiatively cooling to room temperature. The resulting products were washed with hot deionized water to remove the flux, and then briefly washed once with 1M HNO₃ to remove any excess silver and dried overnight in an oven at 80°C. A fine homogeneous grayish powder of AgNbO₃ was obtained in high purity, as judged from powder X-ray diffraction. The solid-state method of preparing AgNbO₃ involved grinding, pelletizing, and heating the Ag₂O and Nb₂O₅ reactants to 900°C for 12h, according to the reported procedures.¹⁷

High-resolution Powder X-ray Diffraction (PXRD) data of all products were collected on an INEL diffractometer using CuK α_1 ($\lambda = 1.54056\text{\AA}$) radiation from a sealed-tube X-ray generator (35kV, 30mA) using a curved position sensitive detector (CPS120). Unit cell parameters of the flux-prepared samples were calculated using the LATCON software.²⁸ Field-emission scanning electron microscopy analyses were performed on a JEOL SEM

6400, and concomitantly the energy dispersive X-ray (EDX) spectra were taken as a check of the elemental compositions. UV-Vis diffuse reflectance spectra (DRS) were collected for all samples on a Shimadzu UV-3600 spectrophotometer equipped with an integrating sphere. BET surface area analyses were performed using a Quantachrome ChemBET Pulsar TPR/TPD.

2.2. *Photocatalysis Testing.* The photocatalytic activity for H₂ formation was measured using an outer-irradiation type fused-silica reaction cell with a volume of 90 mL and irradiated under visible light ($\lambda > 420$ nm). First, each sample was loaded with a 1 wt% Pt cocatalyst using the photodeposition method.⁵ Numerous previous studies have shown that platinum islands on a metal oxide surface can function as a kinetic aid to the reduction of H₂O to give H₂.²⁹ Typically, 250mg of a AgNbO₃ sample was mixed with 30mL of an aqueous solution of dihydrogen hexachloroplatinate(IV) (H₂PtCl₆·6H₂O; Alfa Aesar, 99.95%), and which was then irradiated for 6 h using a 400W Xe arc-lamp with constant stirring using a magnetic stir bar. UV-Vis measurements of the remaining solution confirmed a complete deposition of the platinum cocatalyst. After platinization, the particles were separated via centrifugation, washed with distilled water to remove any remaining Cl⁻ ions, and then dried overnight in an oven at 80°C. For the photocatalytic H₂ measurements, the platinized AgNbO₃ was then added to the fused-silica reaction vessel that was filled with a 20% aqueous methanol solution. The added methanol functions as a hole scavenger, thereby generating CO₂ from its photo-oxidation, and which allows the measurement of the H₂ formation rate alone without the typically more difficult concomitant formation of O₂ being necessary and potentially rate limiting.⁴ The net balanced reaction is: CH₃OH + H₂O

→ 3 H₂ + CO₂. The AgNbO₃ particles were first stirred in the dark for ~ 1 – 2 h, in order to remove any trapped gases on the particles' surfaces. Next, the reaction cell was irradiated under constant stirring for 6 – 12 h using an external 400 W Xe arc-lamp equipped with a long-pass cutoff filter (>420 nm), an IR water filter, and cooled using an external fan. The outlet of the photoreaction vessel was connected to a small horizontal quartz tube that trapped the evolved gases, and contained a moveable liquid bubble that allowed a volumetric determination of the amount of evolved gases at a constant pressure. The most active AgNbO₃ samples exhibited the formation of copious amounts of gases that rose to the top of the reaction cell, and that was observed to be consistent with the movement of the liquid bubble. The progress of the photocatalytic reactions was marked every hour and used to calculate the amount of gases generated in μmol H₂·g⁻¹·h⁻¹. The trapped gases were manually injected into a gas chromatograph (SRI MG #2; helium ionization and thermal conductivity detectors) in order to confirm the generated gases as H₂ and CO₂.

3. Results and Discussion

3.1 Particle Crystallinity, Sizes, and Surfaces. The AgNbO₃ particles crystallize in a perovskite-related structure in the orthorhombic space group *Pbcm*.²⁶ The NbO₆ octahedra are condensed via corner sharing while Ag atoms occupy the interstitial sites, shown in Figure 4.1. The Na₂SO₄ salt was chosen as a flux based on its previously successful use in the synthesis of La-doped NaTaO₃ and La₂Ti₂O₇, as well as for its low cost and ease of removal after synthesis.³⁰ The Powder X-ray Diffraction (PXRD) patterns of the flux-prepared AgNbO₃ products could be fitted and indexed to the reported structure type, as shown in Figure 4.2.²⁷ Refined unit-cell parameters for all samples are provided in the

Supporting Information. These PXRD data show that high purity and good crystallinity could be obtained in short reaction times of 1, 2, and 10 hours and at $\text{Na}_2\text{SO}_4(\text{flux}):\text{AgNbO}_3$ molar ratios of 1:1, 2:1 and 3:1. Synthetic attempts using larger flux: AgNbO_3 ratios and higher reaction temperatures resulted in the formation of NaNbO_3 , as identified by PXRD. A barely detectable amount of NaNbO_3 was also observed as a separate phase in the PXRD patterns for the reactions at the 3:1 molar ratio. However, NaNbO_3 can be ruled out as a contributor to visible-light photocatalysis because of its large bandgap size (~ 3.4 eV), as reported previously.¹

In order to evaluate the AgNbO_3 particle sizes and morphologies, field-emission SEM images were taken on samples prepared using flux: AgNbO_3 ratios and heating times of 1:1 for 1 h (ANO1), 1:1 for 10 h (ANO3), 2:1 for 10 h (ANO6), 3:1 for 1 h (ANO7), 3:1 for 10h (ANO9), and the solid-state prepared sample. These AgNbO_3 samples represent those having both the shortest and longest reaction times, and the smallest and largest amounts of flux used in the reaction. Shown in Figure 4.3, the AgNbO_3 particles formed in rectangular and block-like shapes that clustered into larger aggregates of particles. A distribution of particle sizes was observed, with the edge dimensions of the particles typically ranging between $\sim 100 - 700$ nm for shorter reaction times of 1h, and $\sim 600 - 4,000$ nm for longer reaction times of 10h. The amount of flux had a relatively small effect on the AgNbO_3 particle sizes, as the particles prepared using larger amounts of flux were only a little smaller. An estimation of the average particle sizes was made based on size measurements on ~ 20 randomly selected particles that were observed in different regions of the sample. These measurements for the 1:1 flux: AgNbO_3 ratio, shown in Figures 4.3A and 4.3B, yield average

sizes of ~450 nm and ~1,700nm for the 1h and 10h reaction times, respectively. For the 3:1 flux:AgNbO₃ ratio, shown in Figures 4.3C and 4.3D, average particle sizes of ~400nm and ~900nm were observed for the 1h and 10h reaction times, respectively. The largest particle sizes were observed in ANO3 for the smallest amount of flux (1:1) and longest reaction time (10h). While the individual AgNbO₃ particle sizes decreased both with increasing flux amounts and decreasing reaction times, a distribution of sizes could be found in all samples. For comparison, field-emission SEM images were taken of the AgNbO₃ sample prepared by the traditional solid-state method, as shown in Figure 4.4. The solid-state products were observed to have no distinctly well-defined morphologies and exhibited a significantly wider range of particle sizes.

An EDX analysis was also performed on AgNbO₃ samples in order to confirm the elemental compositions, provided in the Supporting Information. The spectra revealed primarily Ag, Nb, and O in approximately the 1:1:3 molar ratio. Also, a small but detectable amount of Na was observed in all flux-prepared samples, indicating a small amount of incorporation of Na⁺ from the Na₂SO₄ salt flux. The molar amount ranged from ~7% Na⁺ for the 1:1 flux-prepared samples up to ~12% for the 3:1 flux-prepared samples. These represent the lowest and highest amounts of Na content from among all flux-prepared samples. As described in the PXRD data above, higher flux amounts or longer reaction times yield a minor impurity of NaNbO₃ in the products. NaNbO₃ is a known photocatalyst that is active in UV light only. No detectable amount of S was observed in any of the samples, indicating that the flux itself had been completely removed by the washing.

Surface area measurements were performed on each powdered AgNbO_3 sample, and these data are listed in Table 4.1. The largest measured surface area of $0.65 \text{ m}^2\cdot\text{g}^{-1}$ (ANO7) was obtained for the largest flux amount (3:1) and shortest reaction time (1h), and conversely, the smallest surface area of $0.24 \text{ m}^2\cdot\text{g}^{-1}$ (ANO3) for the smallest flux amount (1:1) and longest reaction time (10h). For intermediate flux reaction conditions, the surface area decreases in a regular way with increasing reactions times and decreasing flux-to-reactant ratios. This trend is consistent with the particle sizes calculated from the SEM images. Further, both the BET surface areas and SEM images confirm that reaction times have a more significant effect on the resulting AgNbO_3 particle sizes than the amount of flux used in the reaction. By comparison, the AgNbO_3 product prepared by the solid-state method exhibited a surface area of $0.55 \text{ m}^2\cdot\text{g}^{-1}$, and which is intermediate between that for the 1 h and 2 h flux reactions. The effects of slower cooling rates on the AgNbO_3 particles were also tested using a 1:1 flux-to-reactant ratio. The flux reactions were slow cooled from 900°C to 750°C at rates of $15^\circ\text{C}/\text{h}$ and $3^\circ\text{C}/\text{h}$, while a third reaction was quickly radiatively cooled to room temperature in 0 h. The measured surface areas of the 0 h, 10 h, and 50 h cooled reactions gradually decreased from $0.39 \text{ m}^2\cdot\text{g}^{-1}$ to $0.30 \text{ m}^2\cdot\text{g}^{-1}$ and to $0.16 \text{ m}^2\cdot\text{g}^{-1}$, respectively. Therefore, the AgNbO_3 surface areas can also be controlled via tuning the cooling rate of the reaction, but not any more significantly than using the flux-to-reactant molar ratio or the reaction time.

3.2. Optical Properties and Photocatalytic Activities. Measurements of the UV-Vis diffuse reflectance spectra were taken on all AgNbO_3 samples in order to determine their optical bandgap sizes, and are shown for several selected samples in Figure 4.5. In all cases, the bandgap sizes were calculated to be within a range of $\sim 2.75 - 2.81 \text{ eV}$, consistent with

previous reports.¹⁷ However, the flux-prepared samples are slightly blue-shifted compared to the AgNbO₃ sample prepared by the solid-state method, most likely owing to the incorporation of small amounts of Na⁺ into the products.

Using a traditional solid-state preparation, the AgNbO₃ particles have previously been shown to oxidize water to O₂ under visible-light irradiation, and with the aid of a co-catalyst, to reduce water to H₂ at rates of ~1.5 μmol H₂·g⁻¹·h⁻¹ in a 10% aqueous methanol solution.¹⁷ When irradiated by photons of bandgap and greater energies, the electrons excited into the conduction band drive the reduction half reaction, while the remaining holes in the valence band are scavenged by methanol to produce CO₂ (a partial-DOS diagram can be found in the Supporting Information). The latter is used in order to measure the formation rate of H₂ alone, as the oxidation of water to O₂ can be slower and rate limiting. Flux syntheses of different particle-size distributions should impact the rates of these surface reactions. The visible-light photocatalytic rates of H₂ formation for the flux-prepared AgNbO₃ products were measured and are listed in Table 4.1. For the 1:1 and 3:1 flux-to-reactant molar ratios, the rates of H₂ formation generally increased with higher surface areas and smaller particle sizes, as obtained by increasing the amount of flux and decreasing the reaction time. The highest observed rate of activity was 5.9 μmol H₂·g⁻¹·h⁻¹ for the AgNbO₃ particles prepared from the 3:1 flux-to-reactant ratio and heated for 1h (ANO7). By contrast, for the 2:1 flux-prepared AgNbO₃ particles, the photocatalytic rates decreased with the shorter reaction times, and instead yielded the highest rate of 4.0 μmol H₂·g⁻¹·h⁻¹ for the longer 10 h reaction time (ANO6). For comparison, the photocatalytic rate of the solid-state prepared AgNbO₃ was measured to be 3.5 μmol H₂·g⁻¹·h⁻¹. These results suggest that particle sizes and surface areas alone do not entirely determine the rate of photocatalysis.

Though particle size, in general, has been shown above to have an impact on the AgNbO₃ photocatalytic activity and rates, another critical consideration is the relative concentration of particle surfaces that is active versus inactive. As described above for AgNbO₃, and as described previously in studies on La₂Ti₂O₇, the smaller particles generally exhibit the highest photocatalytic rates for H₂ formation.³⁰ However, the 2:1 flux-prepared samples (ANO4, ANO5, ANO6) did not follow this expected behavior, listed in Table 1. Thus, higher-magnification field-emission SEM was used to further probe the surfaces of the AgNbO₃ particles exhibiting either the higher or lower activity rates. The SEM images, shown in Figure 4.6, revealed a large concentration of nano-stepped terraced surfaces (20-50nm) on the AgNbO₃ particles prepared with a 1:1 flux ratio at either 1 h (4.6B) or 10 h (4.6A). These nano-stepped features were also observed in the 3:1 flux-prepared samples, Figures 4.6C and 4.6D, but in fewer numbers per particle. By contrast, the 2:1 flux-prepared sample (ANO6), shown in Figures 4.6E and 4.6F, did not exhibit these nano-stepped surfaces, but however, exhibited the lowest rates of H₂ formation. Generally, the photocatalytic rates of AgNbO₃ particles with these surface nanosteps were among the highest observed, while samples that did not exhibit these features were much less active. The AgNbO₃ sample prepared by the solid-state method exhibited very irregular particle surfaces and no distinct and well-formed surface features. After ~6 h of photocatalysis testing, relatively larger and apparently etched edges of ~100 – 200 nm in size were also observed, shown in Figure 4.7. The most inactive solid-state and flux-prepared AgNbO₃ samples frequently required a 1 – 2 h incubation period before any measurable activity began, and which may be the result of the time required for significant surface etching to

occur. However, the PXRD patterns of the AgNbO_3 powders after phototesting showed no detectable degradation or photocorrosion yet, and the sample weights were approximately unchanged. A related study on the UV-photocatalyst NaTaO_3 shows that La-doping yields nano-stepped surface features similar to those found here, but at larger $\sim 100 - 700$ nm sizes.^{31,32} These nanosteps at the metal-oxide surfaces are reported to create separate surface sites for the formation of H_2 and O_2 and also help to inhibit recombination. Therefore, it is likely that the nano-stepped features in AgNbO_3 have a similar effect. A recent report on the solvothermal synthesis of AgNbO_3 particles yields increased photocatalytic activity for O_2 formation, and that was associated with similar nano-stepped surfaces.³⁶ FESEM imaging was further employed in order to examine the deposition of a 1% wt. platinum cocatalyst onto the surface of AgNbO_3 particles and can be found in the Supporting Information. Figure 4.S2 reveals small platinum island deposits onto the surface of a 1:1 Na_2SO_4 flux sample heated for 1h (ANO1). The islands appear to have deposited generally onto the edges and steps of the particles (4.S2A), although deposition onto specific facets is also observed (4.S2D). Platinum-deposited AgNbO_3 particles prepared using a 3:1 flux heated for 1h (ANO7) are shown in Figure 4.S3. As seen previously in the deposited ANO1 samples, the highest concentrations of platinum islands are observed along or near the edges, nanosteps, and defects of the particles' surface, suggesting that these locations exhibit a greater concentration of electron density and are the likely primary 'active sites' for catalysis. Figure 4.S4 shows platinum deposition onto the surface of AgNbO_3 particles prepared by conventional solid-state methods. Although the samples exhibited no well-defined morphologies, platinum cocatalyst islands can be seen on the surfaces and appear more

concentrated near particle edges and defect sites, although a general distribution of islands throughout all observed solid-state products is observed. Future *in-situ* measurements are necessary to more deeply probe the origins and mechanisms of the active sites on the AgNbO₃ surfaces.

Conclusions

The synthesis of AgNbO₃ particles can be performed in a molten Na₂SO₄ flux at 900°C in short reaction times of 1 – 10h, with high purities and homogeneous microstructures that range in size from ~100 – 5,000nm. The smallest particle-size distributions of ~100 – 700nm and highest surface areas of 0.65 m²·g⁻¹ were obtained for the largest amount of flux (3:1) and shortest reaction time (1h). Measured optical bandgap sizes of the AgNbO₃ products were in the range of ~ 2.75 – 2.81 eV. Visible-light photocatalytic rates of the flux-synthesized AgNbO₃ particles for H₂ formation in an aqueous methanol solution were 1.7 – 5.9 μmol H₂·h⁻¹·g⁻¹. The higher rates were correlated with the formation of ~20 – 50 nm terraced surface features on the flux-synthesized particles. By comparison, the AgNbO₃ sample prepared by solid-state methods showed no well-defined particle morphology or microstructure. Thus, the results herein demonstrate the value of flux synthetic methods in tuning particle sizes and surface microstructures in order to probe the origins of photocatalytic activity on the surfaces of metal-oxide particles.

5. Acknowledgments. Financial support of this research is acknowledged from the Chemical Sciences, Geosciences and Biosciences Division, Office of Basic Energy Sciences, Office of Science, U.S. Department of Energy (DE-FG02-07ER15914).

6. Supporting Information. Refined unit-cell parameters from powder X-ray diffraction patterns for all flux-synthesized and solid-state AgNbO₃ products, and representative EDX spectra with calculated elemental compositions. Supplementary data associated with this article can be found, in the online version, at [doi:10.1016/j.jphotochem.2010.06.006](https://doi.org/10.1016/j.jphotochem.2010.06.006).

References

- (1) Domen, K. *Bulletin of the Chemical Society of Japan* **2000**, *73*, 1307.
- (2) Domen, K. *The Korean journal of chemical engineering* **2001**, *18*, 862.
- (3) Kato, H. *Catalysis today* **2003**, *78*, 561.
- (4) Graetzel, M. E. *Energy Resources through Photochemistry and Catalysis*; Academic Press: New York, NY, 1983.
- (5) Kato, H.; Asakura, K.; Kudo, A. *J. Am. Chem. Soc.* **2003**, *125*, 3082.
- (6) Hyun G. Kim, D. W. H., et. al *Chemical Communications* **1999**, *12*, 1077.
- (7) Kudo, A. *The journal of physical chemistry. B* **2000**, *104*, 571.
- (8) Kim, G. H. *Catalysis Letters* **2003**, *91*, 193.
- (9) Kudo, A.; Nakagawa, S.; Kato, H. *Chemistry letters* **1999**, *11*, 1197.
- (10) Abe, R.; Higashi, M.; Sayama, K.; Abe, Y.; Sugihara, H. *J. Phys. Chem. B* **2006**, *110*, 2219.
- (11) Kutty, T. R. N.; Avudaithai, M. *Catalysis Reviews* **1992**, *34*, 373
- (12) Machida, M.; Yabunaka, J.-i.; Kijima, T. *Chemical Communications* **1999**, *19*, 1939.
- (13) Machida, M., et. al *Journal of Materials Chemistry* **2003**, *13*, 1433.
- (14) Takata, T. *Journal of photochemistry and photobiology. A, Chemistry* **1997**, *106*, 45.
- (15) Domen, K. *Catalysis Letters* **1990**, *4*, 339.
- (16) Shimizu, K.-i.; Tsuji, Y.; Hatamachi, T.; Toda, K.; Kodama, T.; Sato, M.; Kitayama, Y. *Phys. Chem. Chem. Phys* **2004**, *6*, 1064

- (17) Kato, H.; Kobayashi, H.; Kudo, A. *J. Phys. Chem. B* **2002**, *106*, 12441.
- (18) Kohtani, S., Akihiko, Kudo, et. al *Photo/Electrochemistry & Photobiology in the Environment, Energy and Fuel* **2004**, *173*, 173.
- (19) Konta, R., Akihiko Kudo, et. al *Phys. Chem. Chem. Phys* **2003**, *5*, 3061.
- (20) Chiu, C.; Li, C.; Desu, S. B. *Journal of the American Ceramic Society* **1991**, *74*, 38.
- (21) Arendt, R. H. *Journal of Solid State Chemistry* **1973**, *8*, 339.
- (22) Arendt, R. H.; Rosolowski, J. H.; Szymaszek, J. W. *Materials Research Bulletin* **1979**, *14*, 703.
- (23) Hedden, D. B. *Journal of Solid State Chemistry* **1995**, *118*, 419.
- (24) El-Toni, M. A. *Materials letters* **2006**, *60*, 185.
- (25) Kan, Y. *Crystal engineering* **2003**, *38*, 567.
- (26) Lukaszewski, M., A Kania, A Ratuszna *Journal of Crystal Growth* **1980**, *48*, 493.
- (27) Fabry, J., et. al *Acta Crystallographica* **2000**, *C56*, 916.
- (28) Schwartzenbach, D. *Acta Crystallographica* **1989**, *A45*, 63.
- (29) Nakamatsu, H. *J. Chem. Soc., Faraday Trans. 1* **1985**, *82*, 527.
- (30) Arney, D.; Porter, B.; Greve, B.; Maggard, P. A. *Journal of Photochemistry and Photobiology. A, Chemistry* **2008**, *Accepted*.
- (31) Kudo, A. *Chemical Physics Letters* **2000**, *331*, 373.
- (32) Kudo, A. A. *Chemistry letters* **2004**, *33*, 1534.

Table 4.1. Measured BET surface areas, and visible-light (>420 nm) photocatalytic rates of H₂ formation,^a for AgNbO₃ particles prepared using different flux conditions and also by the solid-state method.^{b,c}

<u>Sample</u>	<u>Flux:AgNbO₃</u> <u>molar ratio</u>	<u>Reaction</u> <u>Time (h)</u>	<u>Surface</u> <u>Area (m²/g)</u>	<u>Activity</u> <u>(μmol H₂/g-h)</u>
ANO7	3:1	1	0.65	5.9
ANO4	2:1	1	0.61	1.7
ANO1	1:1	1	0.59	4.9
S.S. Method	-	12	0.55	3.5
ANO8	3:1	2	0.55	3.4
ANO5	2:1	2	0.54	2.5
ANO2	1:1	2	0.46	3.6
ANO9	3:1	10	0.43	2.7
ANO6	2:1	10	0.35	4.0
ANO3	1:1	10	0.24	2.4

^a Photocatalysis conditions: 400W Xe arc-lamp with 420nm cutoff filter, 250mg of AgNbO₃, 20% aqueous methanol solution, and 1 wt% Pt surface cocatalyst.

^b Prepared by the solid-state reaction of Ag₂O and Nb₂O₅ at 900 °C for 12 h.

^c All samples were radiatively cooled to room temperature at the time of reaction termination.

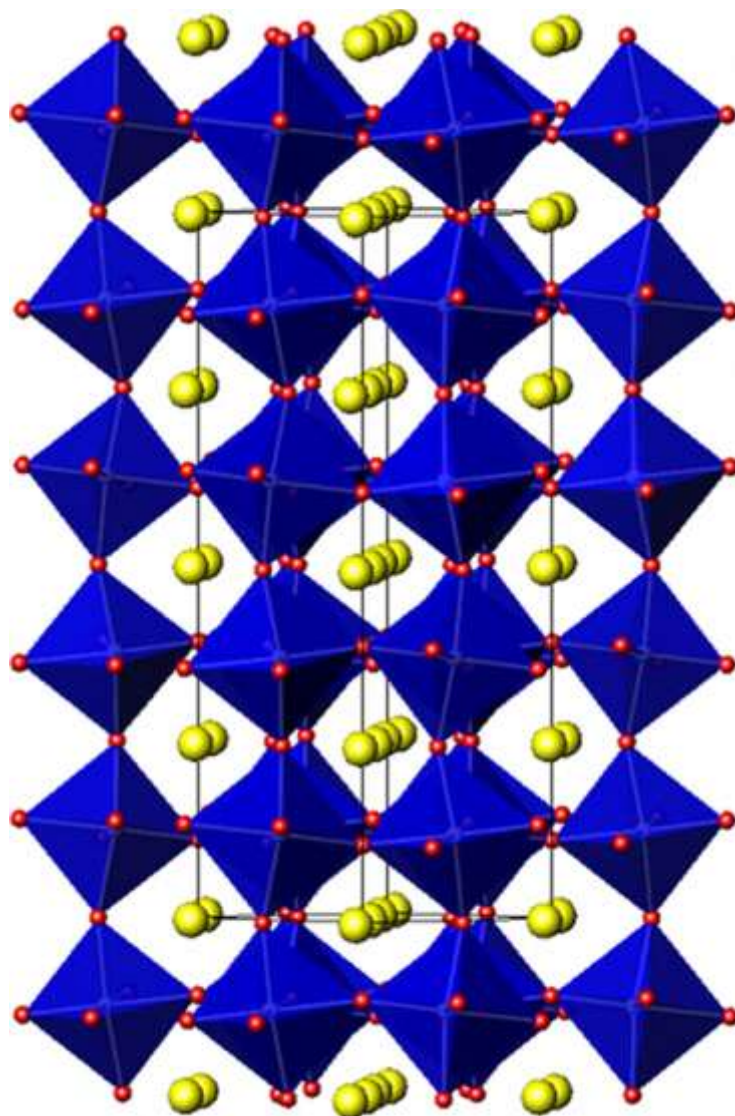


Figure 4.1. Structure of AgNbO₃ with the unit-cell outlined; NbO₆ octahedra are blue, Ag atoms are yellow, and O atoms are shown in red.

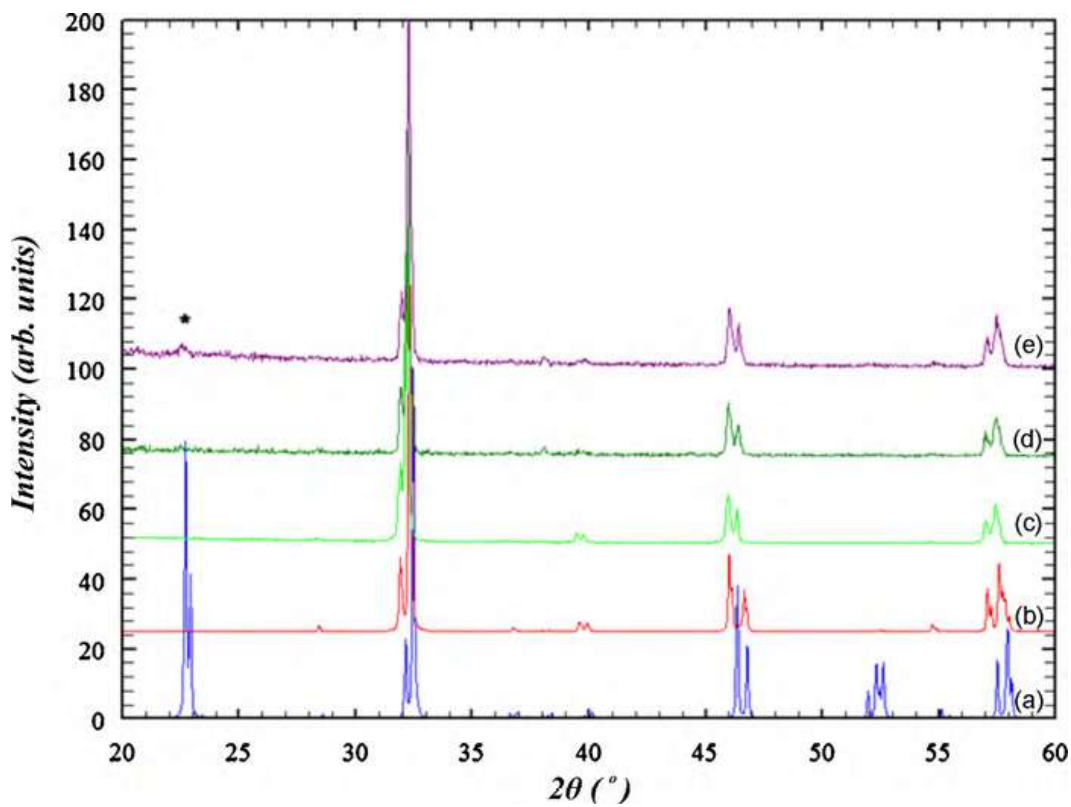


Figure 4.2. Calculated PXRD pattern for (a) NaNbO_3 and (b) AgNbO_3 , and the experimental PXRD data for AgNbO_3 prepared using (c) solid state methods (ANO std.), (d) 1:1 flux at 10h (ANO3), and (e) 3:1 flux at 10h (ANO9).

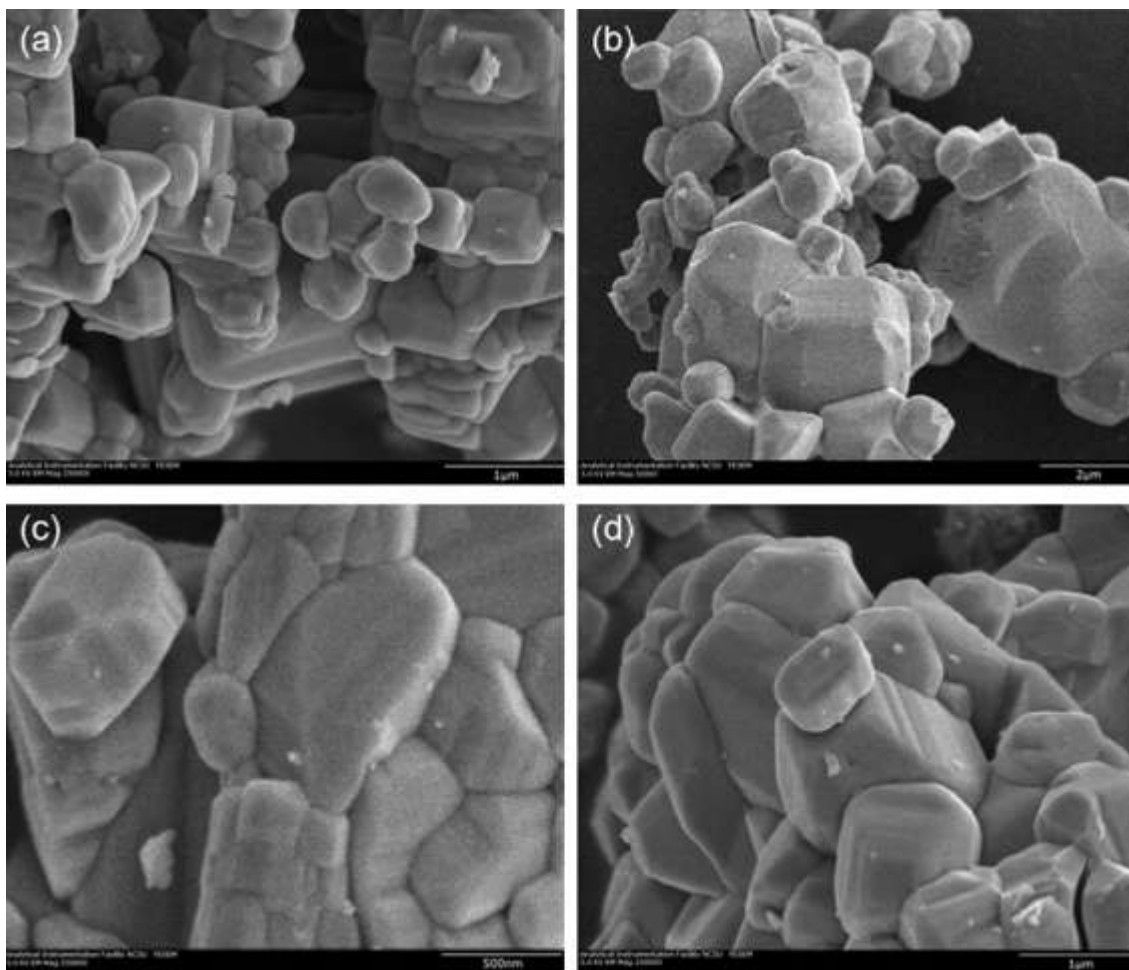


Figure 4.3. Field-emission SEM images of flux-prepared AgNbO_3 particles using (a) 1:1 flux ratio at 1h (ANO1), (b) 1:1 flux ratio at 10h (ANO3), (c) 3:1 flux ratio at 1h (ANO7), and (d) 3:1 flux ratio at 10h (ANO9).

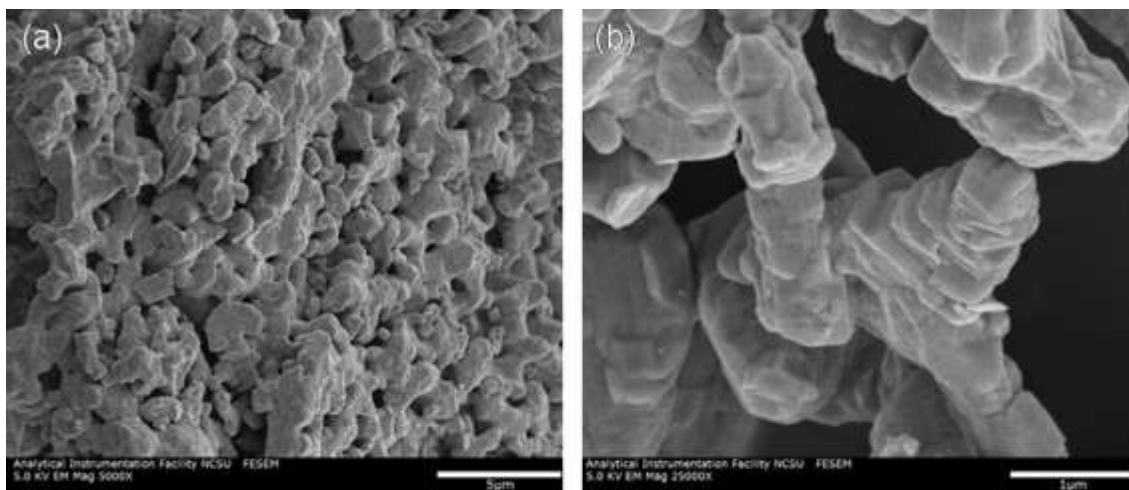


Figure 4.4. Field-emission SEM images of a AgNbO_3 sample prepared by the solid-state method at 900°C for 12h.

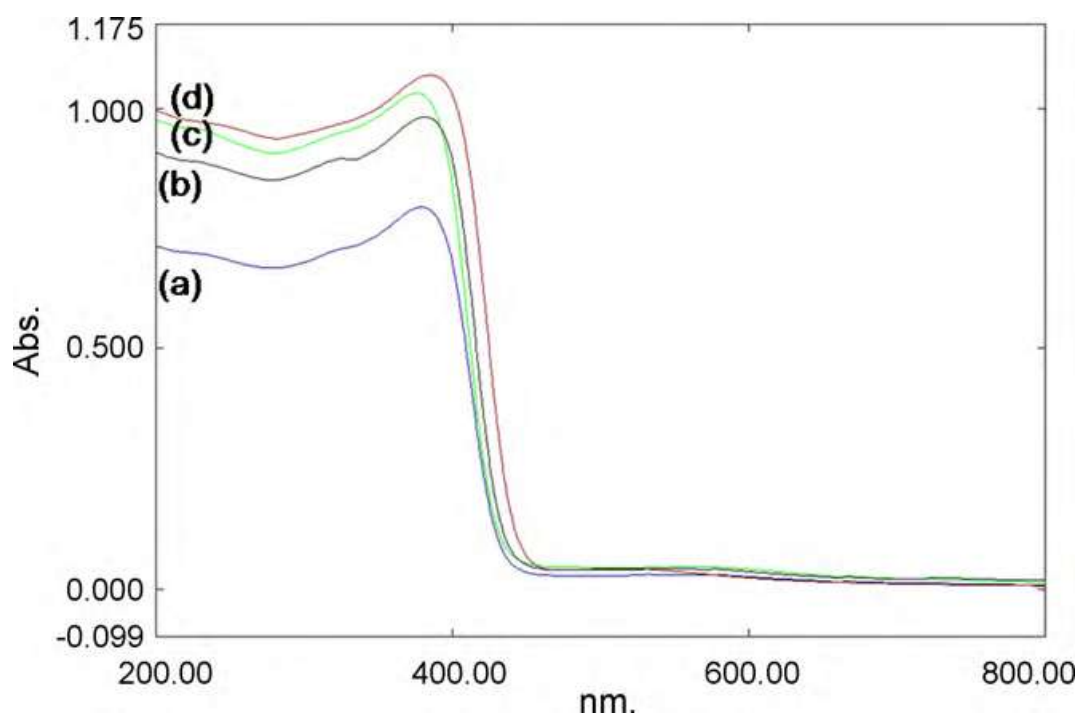


Figure 4.5. Experimental UV-Vis DRS data for flux-prepared AgNbO_3 using (a) 2:1 flux ratio at 10h (ANO6), (b) 1:1 flux ratio at 10h (ANO3), (c) 3:1 flux ratio at 10h (ANO9), and (d) prepared using the solid-state method.

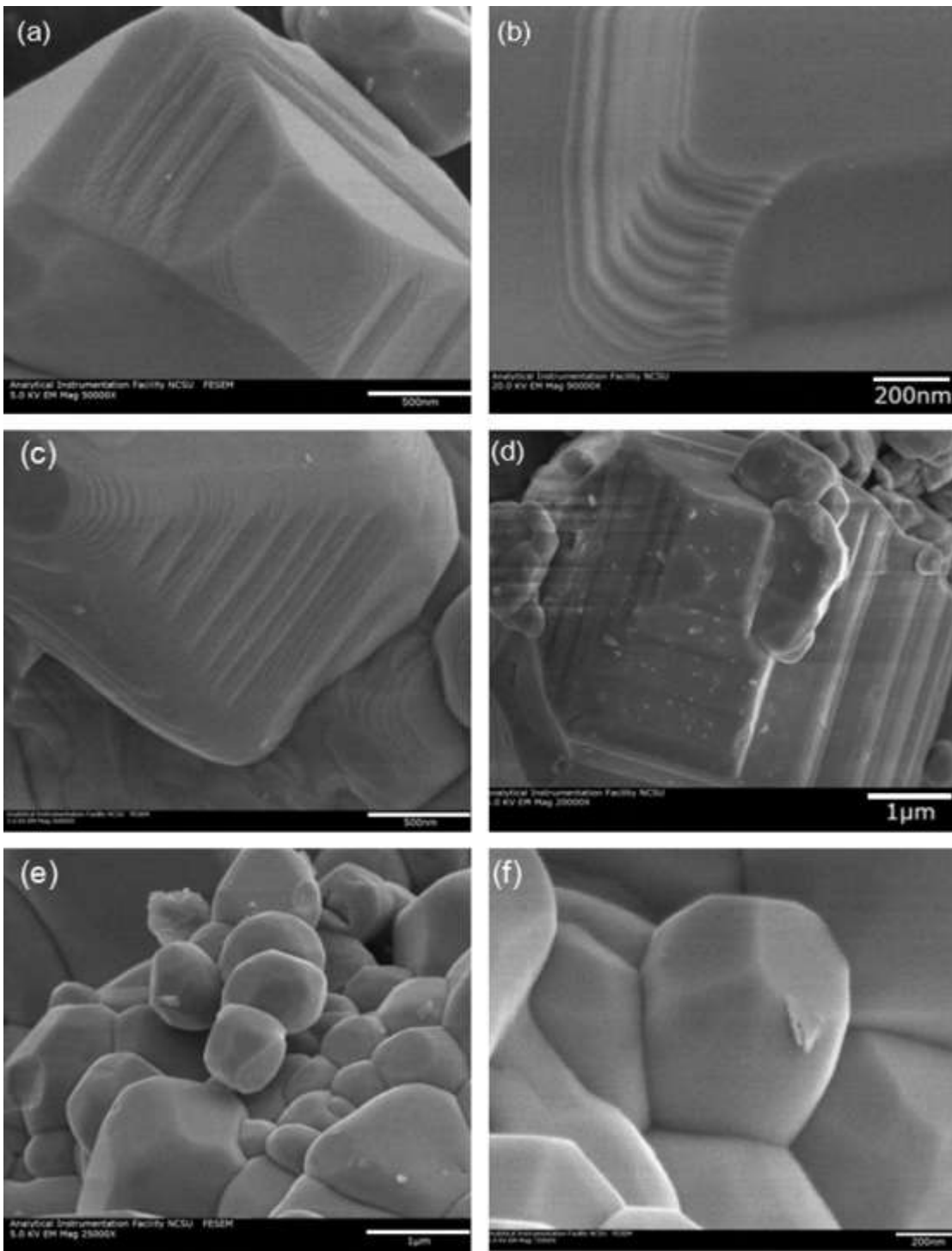


Figure 4.6. High-magnification field-emission SEM images of flux-prepared AgNbO_3 particles using (a, c) 1:1 flux ratio at 10h (ANO3), (b) 1:1 flux at 1h (ANO1) showing $\sim 20\text{nm}$ stepped surface features, (d) 3:1 flux ratio at 1h (ANO7), and (e, f) 2:1 flux ratio at 10h (ANO6) that shows smooth surfaces.

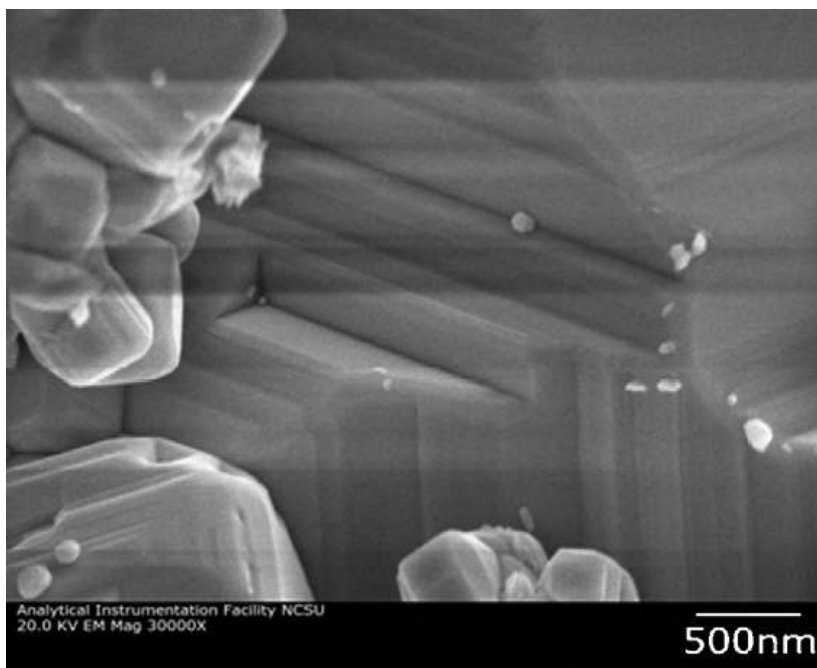


Figure 4.7. Field-emission SEM images of post photocatalysis-tested surfaces of the solid-state prepared AgNbO_3 sample.

Supplementary Information

“Flux Synthesis of AgNbO₃: Effect of Particle Surfaces and Sizes on the Photocatalytic Activity”

*David Arney, Christopher Hardy, Benjamin Greve, and Paul A. Maggard**
Department of Chemistry, North Carolina State University Raleigh,
NC 27695-8204

Table 4.S1. Refined unit-cell parameters for AgNbO₃ samples synthesized by the flux method.^a

Sample ID	<i>a</i> (Å)	<i>b</i> (Å)	<i>c</i> (Å)
ANO1	5.5521(2)	5.6029(1)	15.6416(2)
ANO2	5.5456(2)	5.5985(1)	15.6262(1)
ANO3	5.5418(2)	5.5967(1)	15.6091(1)
ANO4	5.5436(2)	5.5964(1)	15.6173(2)
ANO5	5.5433(2)	5.5962(1)	15.6169(2)
ANO6	5.5401(2)	5.5959(1)	15.6061(2)
ANO7	5.5420(2)	5.5951(1)	15.6136(2)
ANO8	5.5406(2)	5.5946(1)	15.6115(2)
ANO9	5.5382(2)	5.5930(2)	15.6075(2)
AgNbO ₃ std. ^b	5.5478(5)	5.6062(3)	15.6430(4)

^a Unit-cell parameters were refined with the program LATCON [28].

^b Prepared by a solid-state reaction of Ag₂O and Nb₂O₅ at 900° C for 12 h.

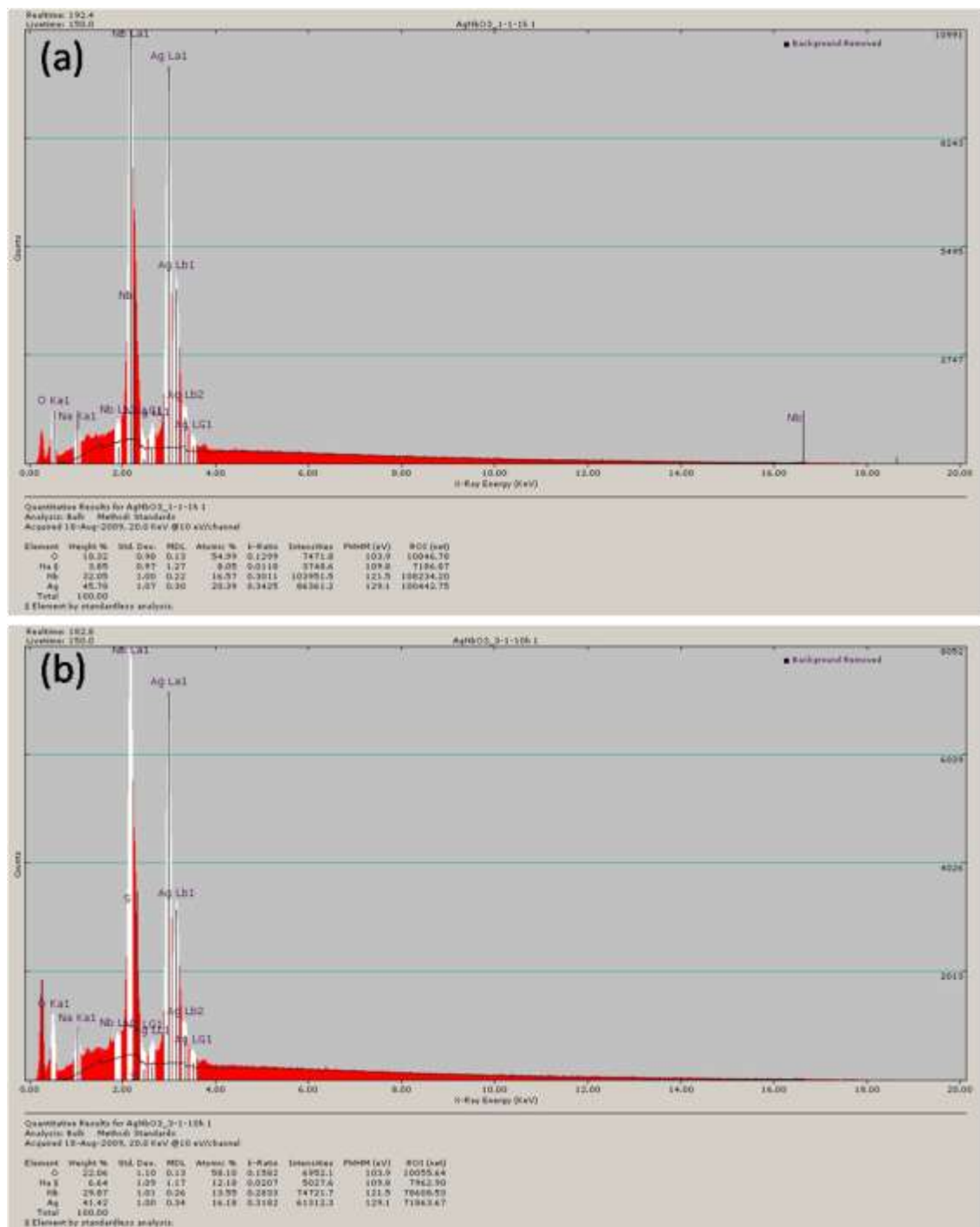


Figure 4.S1. EDX Spectra and calculated elemental compositions of AgNbO_3 samples prepared using a (a) 1:1 flux: AgNbO_3 ratio for 1h (ANO1) and a (b) 3:1 flux: AgNbO_3 for 10h (ANO9).

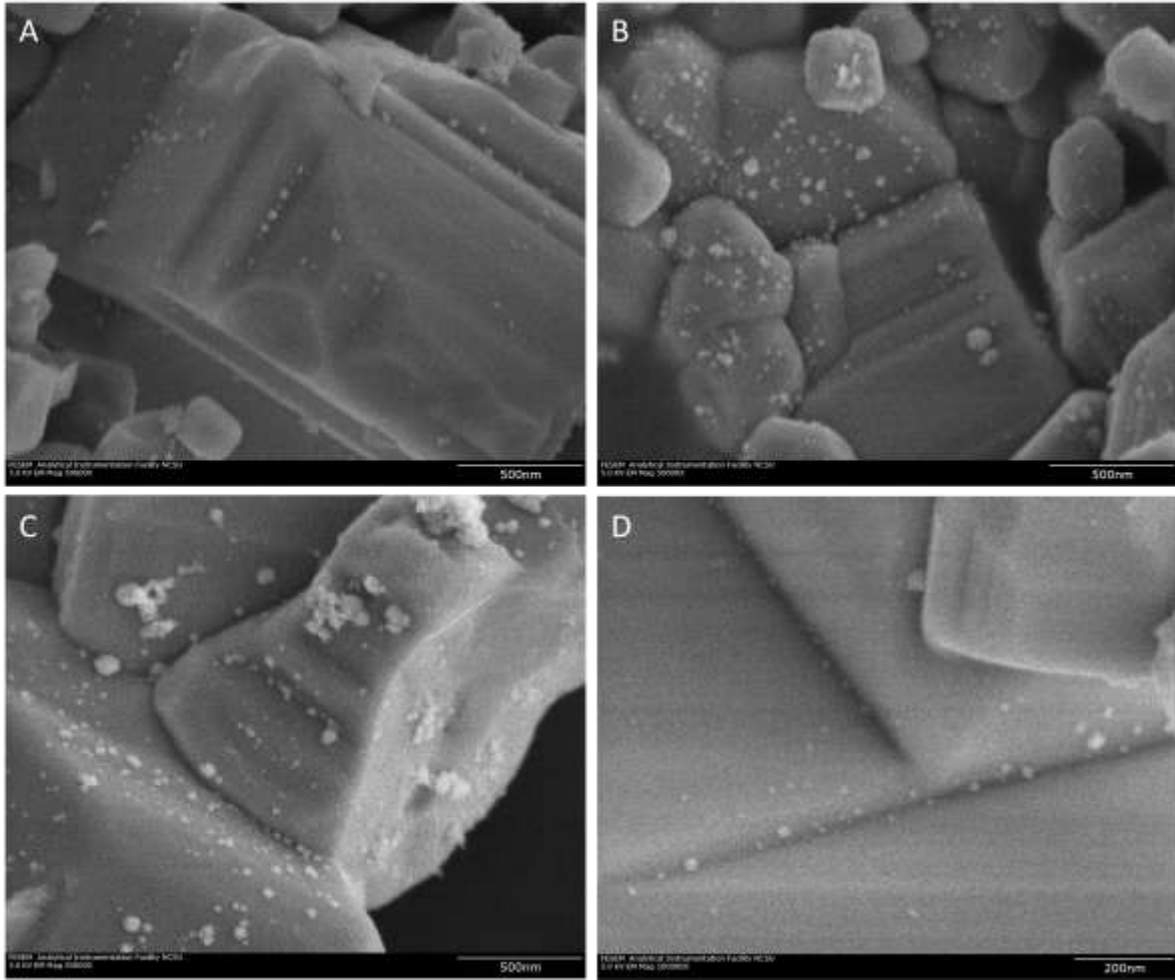


Figure 4.S3. FESEM images of AgNbO_3 prepared from a 3:1 Na_2SO_4 flux heated for 1h after a 1% deposition of a platinum cocatalyst by the photodeposition method. (Data added August 2010).

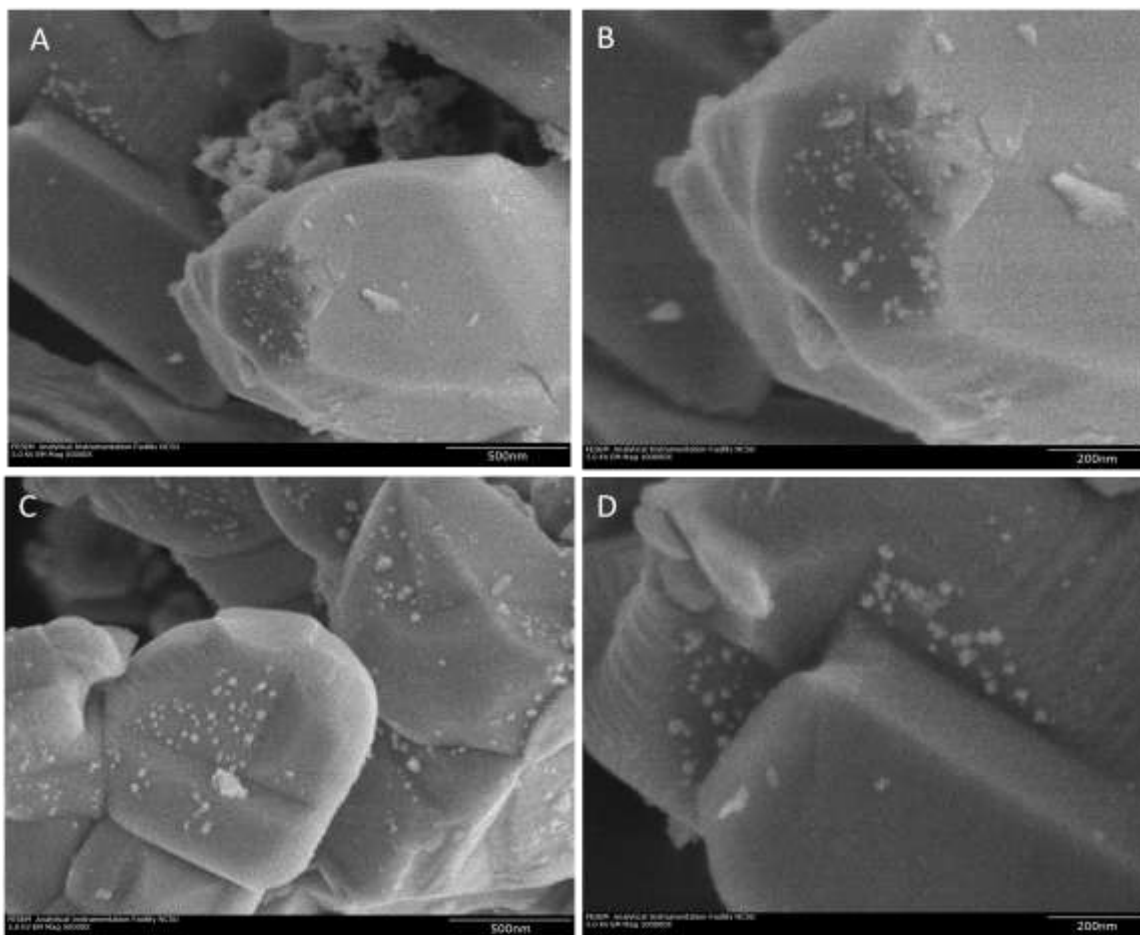


Figure 4.S4. FESEM images of AgNbO_3 prepared by traditional solid state methods after a 1% deposition of a platinum cocatalyst by the photodeposition method. (Data added August 2010).

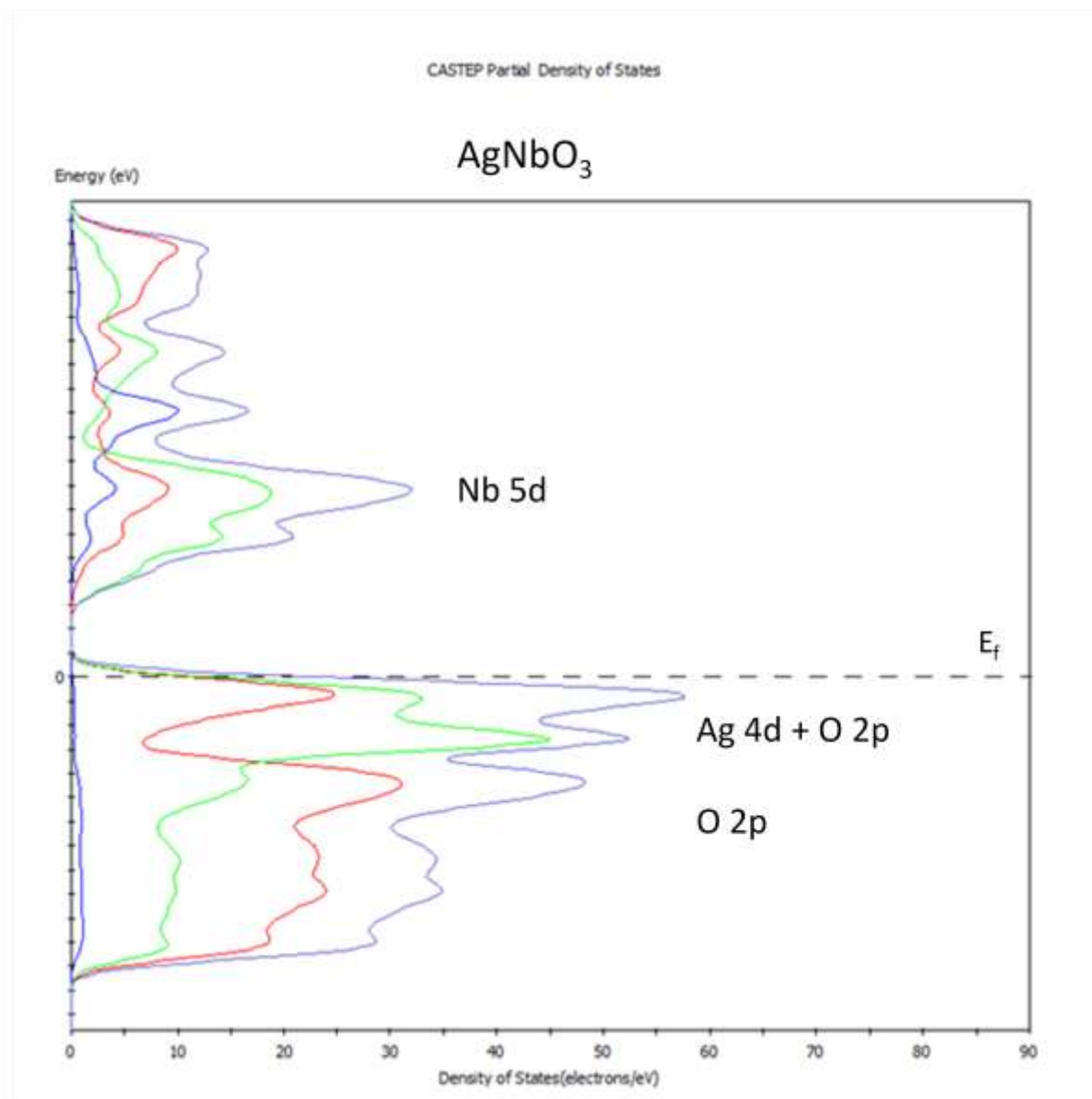


Figure 4.S5. Partial Density of States Calculation for AgNbO₃. The Fermi level has been normalized at zero. Calculation performed with CASTEP using a GGA-PBE functional plane wave ultrasoft pseudopotential method.

CHAPTER 5

Effects of Particle Surface Areas and Microstructures on Photocatalytic H₂ and O₂

Production over PbTiO₃

A paper published in the Journal of the American Ceramics Society

J. Am. Ceram. Soc. **2011** 94, 1483-1489

David Arney, Tylan Watkins, and Paul A. Maggard*

Department of Chemistry, North Carolina State University, Raleigh, NC 27695

Abstract

The visible-light photocatalyst PbTiO₃ was prepared in molten NaCl and PbO fluxes using 0.5:1 – 20:1 flux-to-reactant molar ratios by heating to 1000°C for a duration of 1 h. Yellow-colored powders were obtained in high purity, as confirmed by powder X-ray diffraction and exhibited a bandgap size of ~2.75 eV as determined by UV-Vis diffuse reflectance measurements. Roughly spherical and cubic shaped particles with homogeneous microstructures were observed with sizes ranging from ~100nm – 6,000nm, and surface areas ranging from 0.56 – 2.63 m²/g. The smallest particle-size distributions and highest surface areas were obtained for the 10:1 NaCl flux molar ratio. By comparison solid-state preparations of PbTiO₃ particles exhibit no well-controlled sizes or microstructures. The water-splitting photocatalytic activities of the PbTiO₃ particles were evaluated in visible light ($\lambda > 420$ nm), and yielded maximum rates of 27.4 $\mu\text{mol H}_2\cdot\text{g}^{-1}\cdot\text{h}^{-1}$ for the PbTiO₃ prepared using a 1:1 PbO molar ratio and 183 $\mu\text{mol O}_2\cdot\text{g}^{-1}\cdot\text{h}^{-1}$ for the solid-state prepared sample. The

rates were inversely correlated with the particle surface areas. The relationship between particle morphology and photocatalytic activity provides important insights into understanding the origins of photocatalysis in metal-oxides.

Keywords: Flux Synthesis; PbTiO_3 ; photocatalysis

Introduction

Synthesis of new metal-oxide materials for the photocatalytic production of hydrogen and oxygen from water has had remarkable and rapid growth over the past 25 years.¹⁻⁵ Recently, intense research efforts have been made by several groups to utilize the largest fraction of the solar spectrum and to develop working visible-light active photocatalysts for the overall splitting of water.⁶⁻¹¹ In particular, particle sizes and surface morphologies have been shown to significantly contribute to the performance of the photocatalyst.¹²⁻¹⁵ It has been reported that Pb^{2+} -containing early transition-metal oxides (e.g., Nb, Ta, Ti) can absorb light in the visible range due to their smaller bandgap sizes.^{16,17} This arises because of higher energy Pb 6s orbitals that mix with the O 2p valence band orbitals, and which are still sufficiently below the oxidation potential of H_2O . Among these examples, PbTiO_3 is a recently reported visible-light active photocatalyst and known ferroelectric with a bandgap size of ~ 2.75 eV.¹⁷ However, the preparation of PbTiO_3 in previous studies proceeded via traditional solid-state synthesis, and which provides little control of the particle size and surface characteristics that could significantly affect their photocatalytic activity. As an alternative method, the utilization of molten-salt flux techniques has shown the capability to help better modulate particle sizes and surface features, and which can provide a deeper understanding of how the surfaces influence these reactions.¹⁸⁻²⁰ Also, the use of molten-salt

flux techniques for the preparation of metal oxides can enable shorter reaction times and reduced reaction temperatures.²¹⁻²⁷

Presented herein is an investigation of the visible light photocatalytic properties of ferroelectric PbTiO₃ particles prepared via molten-salt flux methods in order to determine the role of particle size and surface morphology on its photocatalytic activities. The flux synthesis of PbTiO₃ has been previously reported in the literature based on the use of alkali metal salts.^{28,29} However, the research motivation herein was to investigate the photocatalytic activities of flux-prepared PbTiO₃ powders as a function of synthetic conditions and in comparison to their solid-state prepared counterparts. The PbTiO₃ particles were synthesized within molten NaCl and PbO using different flux-to-reactant ratios, followed by an investigation of its effect on the particle sizes and morphologies, as well as their optical properties and photocatalytic rates for H₂ and O₂ formation. The products were characterized by powder X-ray diffraction (PXRD), UV-Vis diffuse reflectance spectroscopy (DRS), BET surface-area analysis, field-emission scanning electron microscopy, and their photocatalytic activities for H₂ and O₂ production.

Experimental

2.1. Synthesis and characterization

The flux synthesis of PbTiO₃ was performed by combining a stoichiometric mixture of PbO (Alfa Aesar, 99.99%) and TiO₂ (Alfa Aesar, Anatase, 99.9%) and grinding it in acetone for 30 min prior to the addition of either the NaCl (m.p. = 801°C) salt flux in flux-to-reactant molar ratios of 1:1, 10:1, and 20:1, or the PbO (m.p. = 888°C) flux in molar ratios of 0.5:1, 1:1, and 2:1. After grinding, the reactant mixtures were then placed inside alumina

crucibles and heated to 1000°C inside a box furnace in air for a reaction time of 1 h. The crucibles were allowed to radiatively cool to room temperature inside the furnace. The resulting powders were washed with hot deionized water to remove the flux, and then washed briefly in 1M HNO₃ to remove excess PbO flux and then dried overnight in an oven at 80°C. Fine homogeneous yellow powders of PbTiO₃ were obtained in high purity, as judged from powder X-ray diffraction. The solid-state method of preparing PbTiO₃ involved grinding, pelletizing, and heating the stoichiometrically-combined PbO and TiO₂ reactants at 1000°C for 48 h, according to the reported procedures.¹⁷

High-resolution Powder X-ray Diffraction (PXRD) data of all products were collected on an INEL diffractometer using CuK α_1 ($\lambda = 1.54056\text{\AA}$) radiation from a sealed-tube X-ray generator (35kV, 30mA) using a curved position sensitive detector (CPS120). Unit cell parameters of the flux-prepared samples were calculated using the LATCON software program.³⁰ Field-emission scanning electron microscopy analyses were performed on a JEOL SEM 6400, and concomitantly the energy dispersive X-ray (EDX) spectra were taken as a check of the elemental compositions. UV-Vis diffuse reflectance spectra (DRS) were collected for all samples on a Shimadzu UV-3600 spectrophotometer equipped with an integrating sphere. BET surface area analyses were performed using a Quantachrome ChemBET Pulsar TPR/TPD.

2.2. Photocatalysis Testing.

The photocatalytic activity for H₂ and O₂ formation were carried out separately using an outer-irradiation type fused-silica reaction cell with a volume of 90 mL and irradiated under both ultraviolet ($\lambda > 300$ nm) and visible ($\lambda > 420$ nm) light energies. For the

photoreduction of H^+ to H_2 , each sample was first loaded with a 1 wt% Pt cocatalyst using a well-known photodeposition method.⁵ Numerous previous studies have shown that platinum islands on a metal oxide surface can function as a kinetic aid for the reduction of H^+ to give H_2 .³¹ Typically, 200 mg of a $PbTiO_3$ sample was mixed with 30mL of an aqueous solution of dihydrogen hexachloroplatinate(IV) ($H_2PtCl_6 \cdot 6H_2O$; Alfa Aesar, 99.95%), and which was then irradiated for 6 h using a 400W Xe arc-lamp with constant stirring using a magnetic stir bar. UV-Vis measurements of the remaining solution confirmed a complete deposition of the platinum cocatalyst. After platinization, the particles were separated via centrifugation, washed with deionized water to remove any remaining Cl^- ions, and then dried overnight in an oven at $80^\circ C$. For the photocatalytic H_2 measurements, 150 mg of the platinized $PbTiO_3$ was then added to the fused-silica reaction vessel and filled with 20% aqueous methanol solution. The added methanol functions as a hole scavenger, thereby generating CO_2 from its photo-oxidation, and which allows the measurement of the H_2 formation rate alone without the typically more difficult concomitant formation of O_2 being necessary and potentially rate limiting.³² The net balanced reaction is: $CH_3OH + H_2O \rightarrow 3 H_2 + CO_2$. For the photooxidation of H_2O to O_2 , each sample was first loaded with a 1 wt% RuO_2 cocatalyst via incipient wetness impregnation, as described before.^{5,33} For photocatalytic O_2 measurements, 150 mg of the loaded $PbTiO_3$ was then added to the fused-silica reaction vessel and filled with a 0.1M $AgNO_3$ solution. The sacrificial Ag^+ is reduced at the $PbTiO_3$ surface to Ag metal under irradiation, which allows the formation of O_2 alone. The net balanced reaction is: $2 AgNO_3 + H_2O \rightarrow 2 Ag_{(s)} + 2 HNO_3 + \frac{1}{2} O_2$. Further details of these photocatalytic measurements have been described previously.²⁰

Results and Discussion

The PbTiO_3 solid crystallizes in a distorted perovskite structure-type in the tetragonal space group $P4mm$ and is a well known ferroelectric.³⁴ The TiO_6 octahedra are condensed via corner sharing while Pb atoms occupy the interstitial sites. The PXRD patterns of the flux products, shown in Figure 5.1, could be fitted and indexed to the reported PbTiO_3 structure, confirming that high purity and good crystallinity could be obtained in only a 1 h reaction time within molten NaCl and PbO fluxes at flux: PbTiO_3 molar ratios of 0.5:1, 1:1, 10:1, and 20:1. Refined unit-cell parameters for all samples were calculated using the LATCON program reporting the following lattice range ($a=3.9018 - 3.9081\text{\AA}$) and ($c=4.134 - 4.154\text{\AA}$).³⁰ The NaCl salt was selected as a flux based on previous successful reports, as well as its low cost and ease of removal after the reaction.²⁹ The PbO flux was chosen owing to its common ion and sufficiently low melting point. The excess loaded PbO flux was easily subsequently removed upon washing with 1M HNO_3 . An EDX analysis was also performed on PbTiO_3 samples in order to confirm the elemental compositions and revealed Pb, Ti, and O in approximately the 1:1:3 molar ratio. There was no significant detection of any Na^+ , indicating the NaCl flux had been removed completely by washing. Measurements of the UV-Vis diffuse reflectance spectra were taken on all PbTiO_3 samples in order to determine their optical bandgap sizes, and are shown for several selected samples in Figure 5.2. In all cases, the bandgap size was calculated to be within a range of $\sim 2.72 - 2.78$ eV based on the onset of absorption, and which was found to be consistent with previous reports.¹⁷

Field-emission SEM images were taken on several PbTiO_3 samples in order to evaluate their particle sizes and morphologies. Figure 5.3 shows PbTiO_3 particles prepared

using a 1:1 NaCl flux (3a and b) and a 10:1 NaCl flux (3c and d). Both samples reveal small, roughly spherical-like particles that fuse into larger aggregates. A distribution of particle sizes was observed, with the edge dimensions of the particles ranging from ~100 – 250 nm for the 1:1 NaCl flux-prepared samples and ~75 – 180 nm for the 10:1 NaCl flux-prepared samples. An estimation of the average particle sizes was made based on size measurements of ~20 randomly selected particles that were observed in different regions of the sample. These measurements for the 1:1 NaCl flux prepared samples yield average sizes of ~170 nm while those prepared with a 10:1 NaCl flux yielded an average size of ~130 nm. The FESEM images of the PbO flux-prepared samples are shown in Figure 5.4 and reveal a contrasting morphology, with particles forming large rectangular and cube-like structures with sizes ranging from ~1,000 – 10,000 nm. Figure 5.4b shows at higher magnification the particle surfaces exhibit small domains with 90° step edges. For comparison, images were also taken of PbTiO₃ samples prepared by the traditional solid-state method, shown in Figure 5.5. The solid state products were observed to be small poly-faceted particles with little distinctly well-defined morphology and rougher surface features compared to those prepared using the NaCl flux. The average size of the particles was estimated to be ~400 nm.

The FESEM images were also taken for selected samples that were photodeposited with 1% (wt.) platinum cocatalyst. Upon irradiation of light with energy greater than the bandgap of PbTiO₃, nanosized Pt particles can be photodeposited onto the surface of the semiconductor particles. The locations of the photodeposited Pt particles can serve as a probe to understand where the most photocatalytically active surfaces of the particles occur. The 20:1 NaCl flux-prepared PbTiO₃ is shown in Figure 5.6 both before (a and b) and after (c and

d) the platinum photodeposition. The platinum particles deposit onto the surface as approximately 15 nm islands, and are in general uniformly distributed among the different surfaces of the spherical particles. The deposition of Pt onto the surface of PbTiO_3 prepared using a 1:1 NaCl flux is shown in Figure 5.7, and reveals small Pt islands deposited in a similar fashion to those observed for the samples prepared in a 20:1 NaCl flux. For comparison, the platinized solid-state sample is shown in 5.7b. Although Pt nano-islands were found in several areas of the particles' surfaces, particularly high concentrations of Pt deposits were observed along edges, grooves, and rough areas of the particle. It has been shown that platinum will preferentially photodeposit onto the most active sites of a metal oxide photocatalyst.^{35,36} It is likely that these areas of the PbTiO_3 particles are the most active surface sites, and therefore received the highest density of Pt deposits. The NaCl flux-prepared samples were roughly spherical with few surface features, and resulted in a rather uniform distribution of Pt deposition over the particles' surfaces.

Surface area measurements were performed on several powdered PbTiO_3 samples and their average values are listed in Table 5.1. For the NaCl-flux samples the surface area generally increased upon increasing the amount of flux used in the reaction. This trend is consistent with the observed particle sizes from the FESEM images. The samples with the highest average surface area of $2.65 \text{ m}^2\cdot\text{g}^{-1}$ were the 10:1 NaCl flux-prepared particles (PBO2). The 20:1 NaCl flux samples (PBO3) yielded an average of $2.36 \text{ m}^2\cdot\text{g}^{-1}$, which indicates that the particle size modulation by the flux had reached a maximum limit. For the PbO flux reactions, the surface area varied from $0.56 \text{ m}^2\cdot\text{g}^{-1}$ for the 0.5:1 PbO flux (PBO4) to $1.08 \text{ m}^2\cdot\text{g}^{-1}$ for the 1:1 PbO flux (PBO5) to $0.39 \text{ m}^2\cdot\text{g}^{-1}$ for the 2:1 PbO flux (PBO6), which

suggests that use of PbO as a flux is less effective at yielding small particle sizes as compared to the NaCl flux, which showed a more linear correlation. For comparison, the PbTiO₃ products prepared by the solid-state method (PBO std.) exhibited a surface area of 0.46 m²·g⁻¹, and which is lower in surface area than any samples prepared using the NaCl flux, but comparable to the PbTiO₃ samples prepared using the smallest amount of PbO flux (PBO4).

The PbTiO₃ particles prepared by solid-state methods have previously been shown to both oxidize water to O₂ and to reduce water to H₂ using sacrificial reagents under visible irradiation.¹⁷ To observe the photocatalytic water-splitting reactions, irradiated photons of bandgap or greater energies must excite electrons in a semiconductor to create electron/hole pairs, which can then both oxidize and reduce water into O₂ and H₂, respectively. In these experiments, AgNO₃ and CH₃OH were employed as sacrificial reagents to observe both half reactions separately. The flux syntheses of different particle sizes and morphologies should impact the rates of these reactions. The photocatalytic rates of H₂ and O₂ production for the flux-prepared PbTiO₃ products are given in Table 5.1. The rate of O₂ formation decreased over time due to metallic silver being deposited onto the surface of the particles and effectively passivating the surface from further reaction. Therefore, the rate of reaction was regarded as the initial activity rate.³⁷ The rates of H₂ formation under visible irradiation were very low compared to the rates observed for O₂. Therefore, the H₂ producing reactions were carried out under ultraviolet irradiation (>300nm), while the O₂ producing reactions were performed under visible irradiation (>420nm). An aqueous solution of 20% MeOH with no added catalyst yielded no production of H₂ under UV irradiation, thereby showing that all the

H₂ gas produced in the reactions are from the activity of the PbTiO₃ catalysts and not from any possible methanol photolysis. In general for the NaCl flux-prepared reactions, the rates of O₂ and H₂ evolution decreased with increasing surface area and smaller particle sizes, which were obtained by increasing the amount of flux used during synthesis. The highest observed rate of O₂ from the NaCl flux prepared samples was 155.8 μmol O₂·g⁻¹·h⁻¹ for the PbTiO₃ particles prepared from the 1:1 NaCl flux, while for H₂ production the sample from the 20:1 NaCl flux evolved at the highest rate of 25.3 μmol H₂·g⁻¹·h⁻¹. The 10:1 NaCl flux sample, which also had the highest observed surface area, recorded the lowest rates for both O₂ and H₂ production, yielding 81.5 μmol O₂·g⁻¹·h⁻¹ and 2.8 μmol H₂·g⁻¹·h⁻¹, respectively. In all NaCl-prepared samples, the activity was observed for at least 24 h. For the PbO flux-prepared samples, the observed photocatalytic activities were quite similar, with the 1:1 PbO flux sample showing slightly higher rates of activity for both O₂ and H₂ production. When compared to the NaCl flux samples, the PbO flux-prepared particles yielded higher rates of activity in all cases, suggesting that activity is not dependent upon having a large surface area or small particle sizes. For comparison, the photocatalytic rates of O₂ and H₂ evolution of the solid-state prepared PbTiO₃ were 183.1 μmol O₂·g⁻¹·h⁻¹ and 19.9 μmol O₂·g⁻¹·h⁻¹, respectively. These rates were higher for all NaCl flux-prepared samples while at the same time exhibiting lower surface area and larger particle sizes from SEM observations. The activity was similar, however, to the observed rates for both PbO flux-prepared samples (PBO4 and PBO5), which had similar surface area measurements. This is most likely due to the solid state and PbO flux-prepared samples having more exposed active sites available for photocatalytic O₂ and H₂ evolution.

In general, particle size has been shown to have a significant impact on the photocatalytic activity, with the smaller particle sizes generally exhibiting higher photocatalytic rates.^{19,38} However, this behavior is in contrast to our observed rates for PbTiO₃. The SEM images of the PbO flux-prepared samples show small nano-sized features at the surface of the particles that are not observed on any images taken of the NaCl flux-prepared samples. Similarly, the SEM images of the solid-state prepared samples show rough-edged particles and grooves that when photodeposited with a Pt cocatalyst received a higher concentration of Pt islands than in other areas of the particle. The NaCl flux-prepared particles were the smallest particles observed, but their surface features are quite smooth with relatively few observable surface features and showed no preferential Pt deposition sites. The photocatalytic rates of PbTiO₃ particles with these small nano-sized features and edges were the highest observed, while samples that did not exhibit these features (i.e. the NaCl flux-prepared samples) were less active. Platinum deposition has previously been shown to preferentially deposit onto the {110} surface of TiO₂ particles, indicating that specific exposed faces aid in electron/hole separation during the photocatalytic reaction.³⁹ Also, several studies have shown that the domain dipolarization in ferroelectric materials can more efficiently separate charge carriers and reduce recombination, thereby increasing photocatalytic activity.⁴⁰⁻⁴³ Given that the ferroelectric polarization is diminished in small nano-sized particles, this effect may explain the decreased activity observed in the smallest PbTiO₃ particles.²⁹ It has also been reported in the photocatalytic perovskite, NaTaO₃, that La-doping yields nano-stepped surface features that dramatically increase photocatalytic activity by creating separate surface sites for the formation of O₂ and H₂ and also help to

inhibit recombination.^{10,44} It is also highly probable that a combination of the larger particle sizes and the nano-features and edges observed in PbTiO₃ lead to further enhancements in its photocatalytic activities.

Conclusions

The visibly-active PbTiO₃ can be prepared in either a NaCl or PbO flux, yielding high purities and homogeneous microstructures that range in size from ~ 100 – 10,000 nm, with the highest surface areas obtained for the 10:1 NaCl flux-prepared samples. Optical characterization revealed bandgap sizes of the PbTiO₃ products in the range of ~ 2.72 – 2.78 eV, which produced visible-light photocatalytic O₂ rates of 81.5 – 180.7 μmol O₂·g⁻¹·h⁻¹ and ultraviolet photocatalytic H₂ rates of 2.8 – 27.4 μmol H₂·g⁻¹·h⁻¹ in sacrificial AgNO₃ and MeOH solutions, respectively. Higher rates were correlated with the formation of surface nano-features and observable edges and grooves on the PbO flux-prepared particles. By comparison, the PbTiO₃ sample prepared by the solid-state method also exhibited several rough edges, yet little well-defined particle morphology. Thus, the results demonstrate the value of flux synthetic methods in tuning particle sizes and surface microstructures in order to probe the origins of photocatalytic activity on the surfaces of metal-oxide particles.

Acknowledgments.

Financial support of this research is acknowledged from the Chemical Sciences, Geosciences and Biosciences Division, Office of Basic Energy Sciences, Office of Science, U.S. Department of Energy (DE-FG02-07ER15914).

References

- (1) Fujishima, A.; Honda, K. *Nature* **1972**, *238*, 37.
- (2) Domen, K.; Kondo, J.; Hara, M.; Takata, T. *Bulletin of the Chemical Society of Japan* **2000**, *73*, 1307.
- (3) Domen, K.; Hara, M.; Kondo, J.; Takata, T.; Kudo, A.; Kobayashi, H.; Inoue, Y. *The Korean journal of chemical engineering* **2001**, *18*, 862.
- (4) Hwang, D. W.; Kim, H. G.; Lee, J. S.; Kim, J.; Li, W.; Oh, S. H. *J. Phys. Chem. B* **2005**, *109*, 2093.
- (5) Kato, H.; Asakura, K.; Kudo, A. *J. Am. Chem. Soc.* **2003**, *125*, 3082.
- (6) Hwang, D. W.; Kim, G. H.; Jang, J. S.; Bae, S. W.; Ji, S. M.; Lee, J. S. *Catalysis today* **2004**, *93*, 845.
- (7) Kato, H.; Kobayashi, H.; Kudo, A. *J. Phys. Chem. B* **2002**, *106*, 12441.
- (8) Kohtani, S.; Yamamoto, N.; Kitajima, K.; Kudo, A.; Kato, H.; Tokomura, K.; Hayakawa, K.; Nakagaki, R. *Photo/Electrochemistry & Photobiology in the Environment, Energy and Fuel* **2004**, *173*, 173.
- (9) Konta, R.; Kato, H.; Kobayashi, H.; Kudo, A. *Phys. Chem. Chem. Phys* **2003**, *5*, 3061.
- (10) Kudo, A.; Kato, H.; Tsuji, I. *Chemistry letters* **2004**, *33*, 1534.
- (11) Maeda, K.; Teramura, K.; Lu, D.; Saito, N.; Inoue, Y.; Domen, K. *J. Phys. Chem. C* **2007**, *111*, 7554.
- (12) Zhang, C.; Zhu, Y. *Chemistry of Materials* **2005**, *17*, 3537.
- (13) Yoshimura, J.; Ebina, Y.; Kondo, J.; Domen, K.; Tanaka, A. *J. Phys. Chem.* **1993**, *97*, 1970.

- (14) Takata, T.; Shinohara, K.; Tanaka, A.; Hara, M.; Kondo, J.; Domen, K. *Journal of photochemistry and photobiology. A, Chemistry* **1997**, *106*, 45.
- (15) Inoue, Y.; Asai, Y.; Sato, K. *J. Chem. Soc., Faraday Trans.* **1994**, *90*, 797.
- (16) Kim, H. G.; Hwang, D. W.; Lee, J. S. *Journal of the American Chemical Society* **2004**, *126*, 8912.
- (17) Kim, H. G.; Becker, O. S.; Jang, J. S.; Ji, S. M.; Borse, P. H.; Lee, J. S. *J. Solid State Chem.* **2006**, *179*, 1214.
- (18) Porob, D. G.; Maggard, P. A. *Journal of Solid State Chemistry* **2006**, *179*, 1727.
- (19) Arney, D., Porter, Brittany; Greve, Benjamin; Maggard, P.A. *Journal of photochemistry and photobiology. A, Chemistry* **2008**, *199*, 230.
- (20) Arney, D., Hardy, Christopher; Greve, Benjamin; Maggard, Paul A. *Journal of photochemistry and photobiology. A, Chemistry* **2010**, *In Press*.
- (21) Chiu, C.; Li, C.; Desu, S. B. *Journal of the American Ceramic Society* **1991**, *74*, 38.
- (22) Arendt, R. H. *Journal of Solid State Chemistry* **1973**, *8*, 339.
- (23) Arendt, R. H.; Rosolowski, J. H.; Szymaszek, J. W. *Materials Research Bulletin* **1979**, *14*, 703.
- (24) Hedden, D. B.; Torardi, C.; Zegarski, W. *Journal of Solid State Chemistry* **1995**, *118*, 419.
- (25) El-Toni, M. A.; Yin, S.; Sato, T. *Materials letters* **2006**, *60*, 185.
- (26) Kan, Y.; Jin, X.; Wang, P.; Li, Y.; Cheng, Y.-B.; Yan, D. *Materials Research Bulletin* **2003**, *38*, 567.

- (27) Porob, D. G.; Maggard, P. A. *Materials Research Bulletin* **2006**, *41*, 1513.
- (28) Aboujalil, A.; Deloume, J.-P.; Chassagneux, F.; Scharff, J.-P.; Durand, B. *J. Mater. Chem.* **1998**, *8*, 1601.
- (29) Cai, Z.; Xing, X.; Yu, R.; Sun, X.; Liu, G. *Inorg Chem* **2007**, *46*, 7423.
- (30) Schwarzenbach, D. *Acta Crystallogr., Sect. A: Found. Crystallogr.* **1989**, *A45*, 63.
- (31) Nakamatsu, H.; Kawai, T.; Koreeda, A.; Kawai, S. *J. Chem. Soc., Faraday Trans. 1: Physical Chemistry in Condensed Phases* **1986**, *82*, 527.
- (32) Graetzel, M. E. *Energy Resources through Photochemistry and Catalysis*; Academic Press: New York, NY, 1983.
- (33) Zou, Z.; Arakawa, H. *Journal of photochemistry and photobiology. A, Chemistry* **2003**, *158*, 145.
- (34) Glazer, A. M.; Mabud, S. A. *Acta Crystallogr., Sect. B: Structural Crystallography and Crystal Chemistry* **1978**, *B34*, 1065.
- (35) Matsumoto, Y.; Ida, S.; Inoue, T. *J. Phys. Chem. C* **2008**, *112*, 11614.
- (36) Compton, O. C.; Carroll, E. C.; Kim, J. Y.; Larsen, D. S.; Osterloh, F. E. *J. Phys. Chem. C* **2007**, *111*, 14589.
- (37) Kudo, A.; Omori, K.; Kato, H. *Journal of the American Chemical Society* **1999**, *121*, 11459.
- (38) Kudo, A.; Miseki, Y. *Chemical Society Reviews* **2009**, *38*, 253.
- (39) Ohno, T.; Sarukawa, K.; Matsumura, M. *New J. Chem.* **2002**, *26*, 1167.
- (40) Giocondi, J. L.; Rohrer, G. S. *J. Phys. Chem. B* **2001**, *105*, 8275.

- (41) Burbure, N. V.; Salvador, P. A.; Rohrer, G. S. *J. Am. Ceram. Soc.* **2006**, *89*, 2943.
- (42) Giocondi, J. L.; Rohrer, G. S. *Chem. Mater.* **2001**, *13*, 241.
- (43) Inoue, Y. *Energy Environ. Sci.* **2009**, *2*, 364.
- (44) Kudo, A.; Kato, H. *Chemical Physics Letters* **2000**, *331*, 373.

Table 5.1. Measured photocatalytic rates of O₂ and H₂ formation for flux-prepared PbTiO₃ and also by the solid state method.

<u>Sample</u>	<u>Flux:AgNbO₃</u> <u>Ratio</u>	<u>Cocatalyst</u> <u>(1% wt.)</u>	<u>Wavelength</u> <u>(nm)</u>	<u>Surface</u> <u>Area</u> <u>(m²-g⁻¹)</u>	<u>Activity</u> <u>(μmol</u> <u>O₂/g-h)</u>	<u>Activity</u> <u>(μmol</u> <u>H₂/g-h)</u>
PbTiO ₃ std ^a	-	RuO ₂	>420	0.46	183.1	-
		Pt	>300			19.9
PBO1	1:1 NaCl	RuO ₂	>420	1.43	155.8	-
		Pt	>300			9.1
PBO2	10:1 NaCl	RuO ₂	>420	2.63	81.5	-
		Pt	>300			2.8
PBO3	20:1 NaCl	RuO ₂	>420	2.36	143.4	-
		Pt	>300			25.3
PBO4	0.5:1 PbO	RuO ₂	>420	0.56	172.3	-
		Pt	>300			27.0
PBO5	1:1 PbO	RuO ₂	>420	1.08	180.7	-
		Pt	>300			27.4

^a Prepared by solid state reaction of PbO and TiO₂ reactants at 1000 C for 48 h.

Testing Conditions: Outer irradiation 1000 W high-pressure Xe arc-lamp, 150 mg of PbTiO₃, 20% MeOH_(aq) or 0.08M AgNO_{3(aq)}, and 1 wt% Pt or RuO₂ surface cocatalyst.

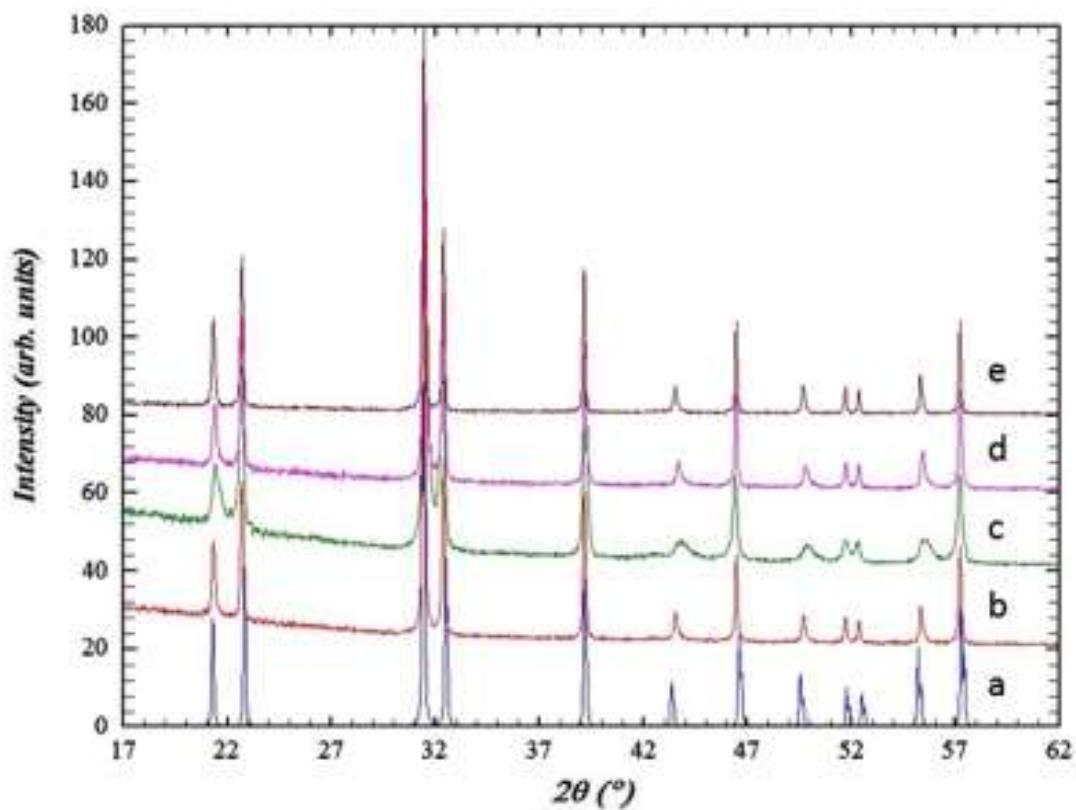


Figure 5.1. The XRD Pattern of the PbTiO_3 products. (a) Calculated theoretical PbTiO_3 pattern, (b) solid state method (c) 1:1 NaCl Flux heated for 1 h, (d) 10:1 NaCl flux heated for 1 h, (e) 2:1 PbO flux heated for 1 h.

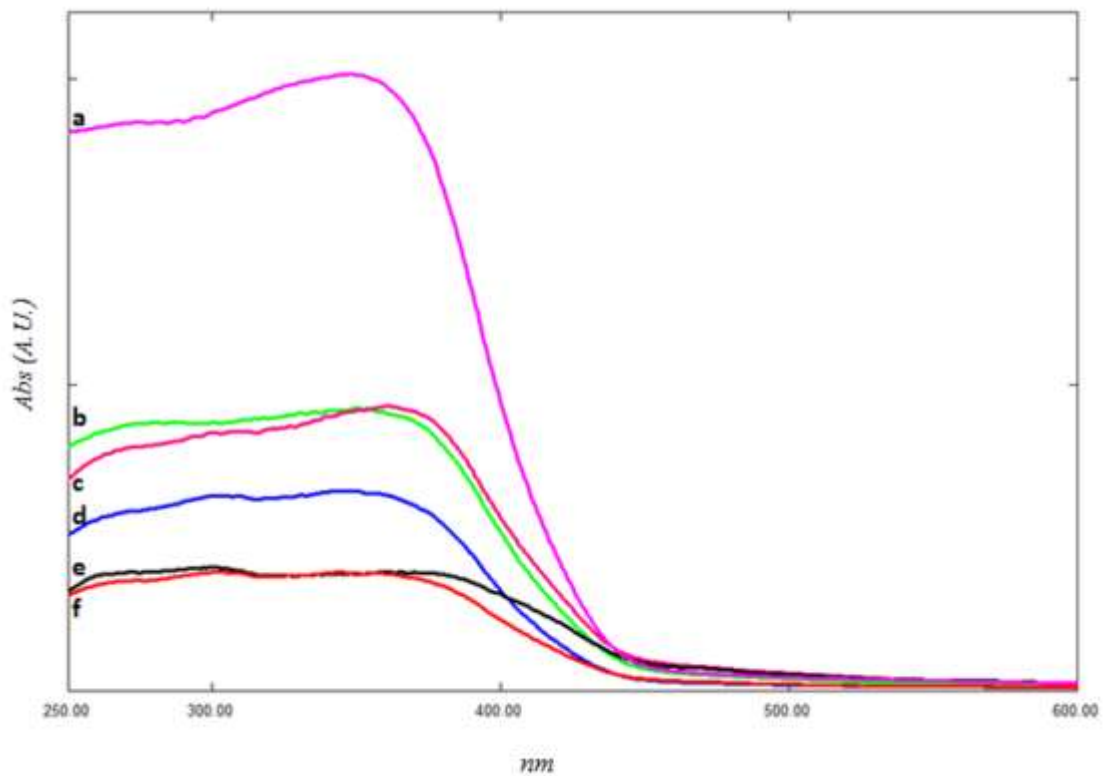


Figure 5.2. UV-Vis Diffuse Reflectance Spectra of PbTiO_3 powders prepared via (a) Solid-State Methods, (b) 1:1 NaCl (PBO1), (c) 0.5:1 PbO (PBO4), (d) 1:1 PbO (PBO5), (e) 20:1 NaCl (PBO3), and (f) 10:1 NaCl (PBO2). Reflectance has been converted to absorbance by the Kubelka-Munk method.

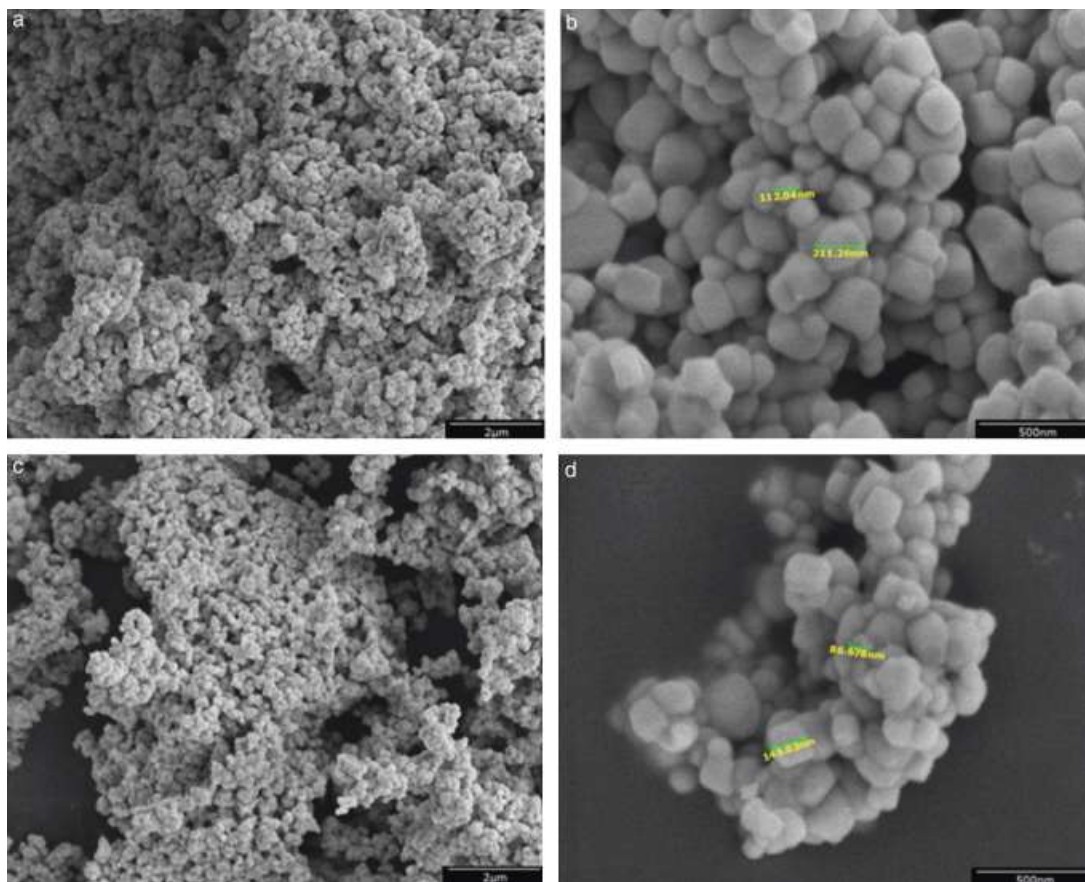


Figure 5.3. FESEM Images of (a,b) PBO1 and (c,d) PBO2 prepared at 1000°C for 1h using a NaCl molten flux in flux:PbTiO₃ ratios of (a,b) 1:1 and (c,d) 10:1

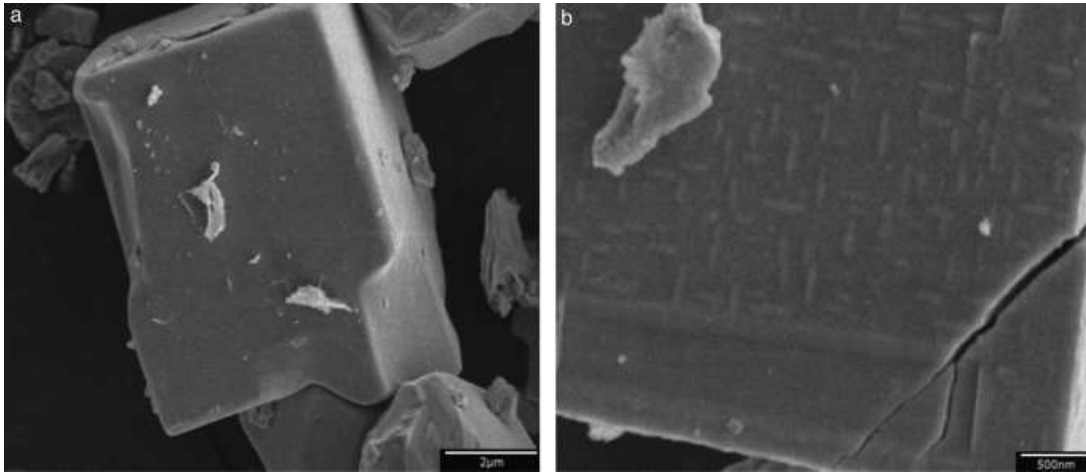


Figure 5.4. FESEM Images of PBO6 prepared at 1000°C for 1h in a PbO molten flux with a flux:PbTiO₃ molar ratio of 2:1.

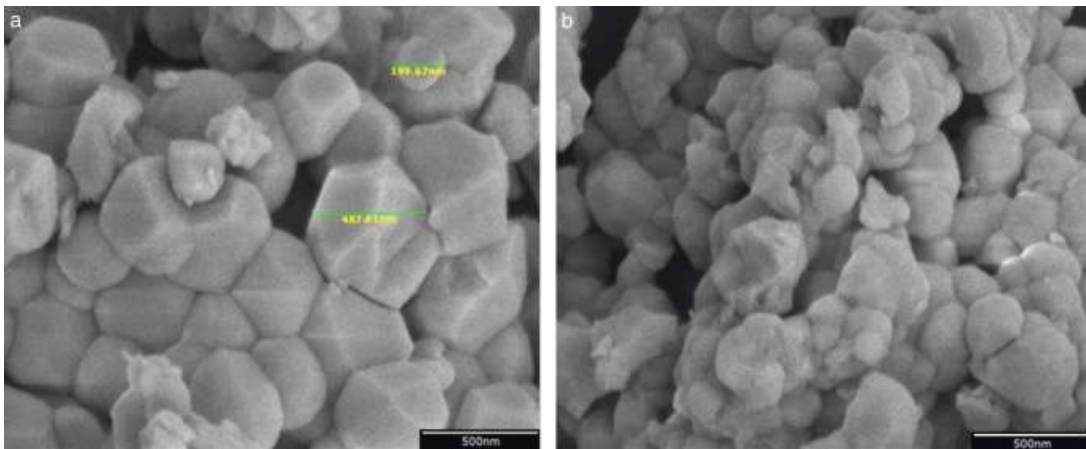


Figure 5.5. FESEM Images of the solid-state PbTiO₃ prepared at 1000°C for 48h.

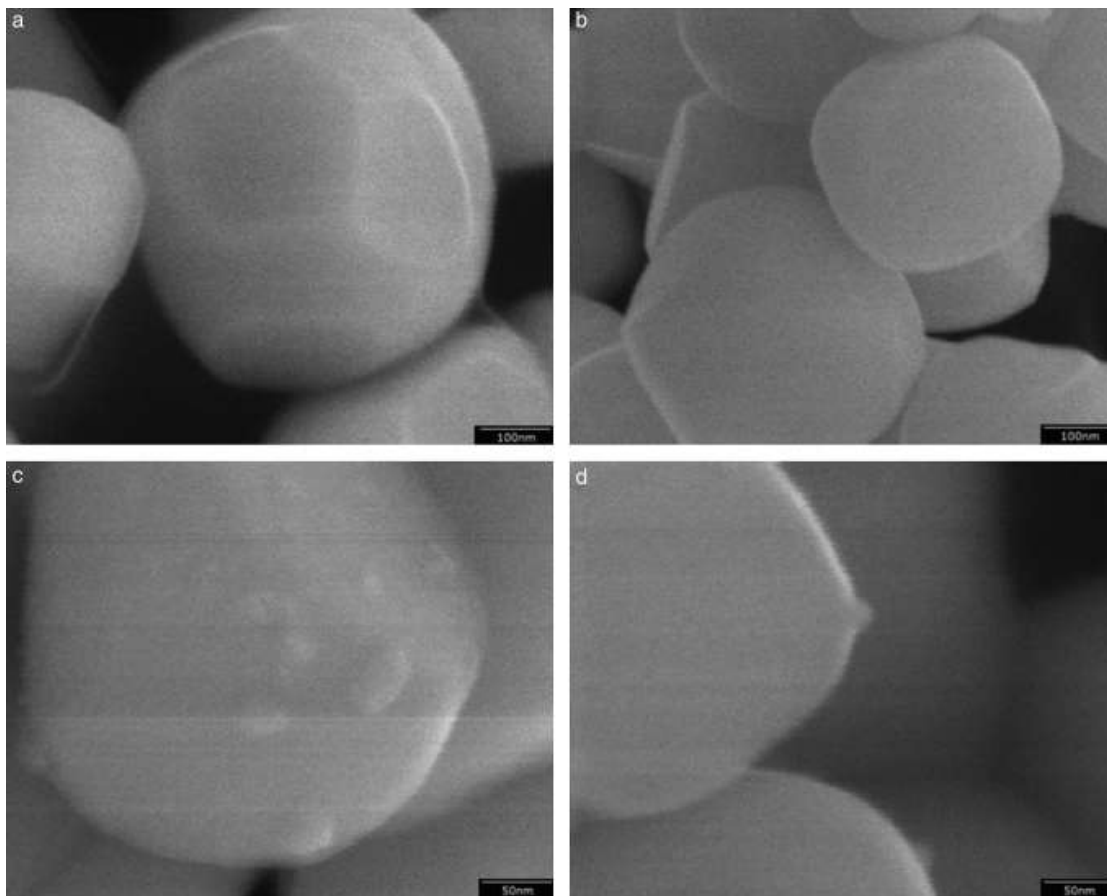


Figure 5.6. FESEM Images of PBO₃ prepared in a 20:1 NaCl flux showing (a and b) bare particles before platinum photodeposition and (c and d) with a 1% wt. Pt photodeposited cocatalyst.

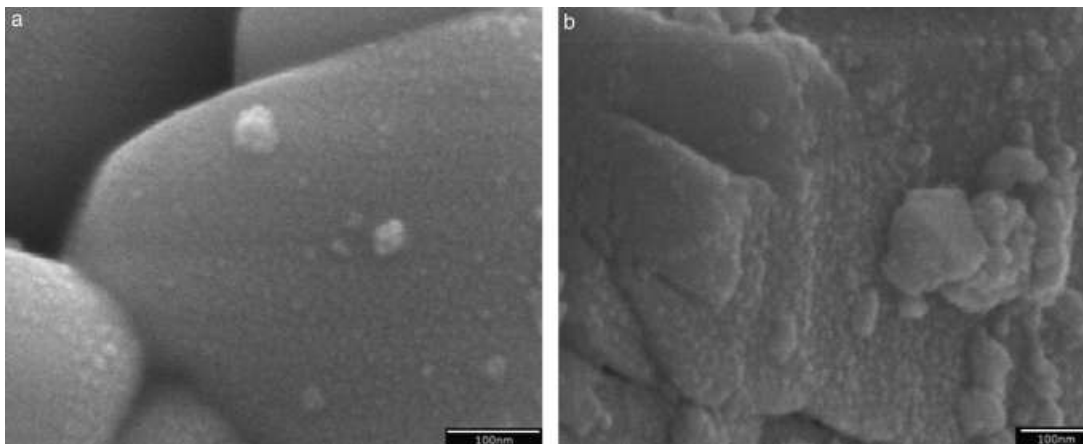


Figure 5.7. FESEM Images of platinized PbTiO_3 prepared (a) using a 1:1 NaCl Flux (PBO1) and (b) by traditional solid state methods (PBO std.).

Supplementary Information

Effects of Particle Surface Areas and Microstructures on Photocatalytic H₂ and O₂ Production over PbTiO₃

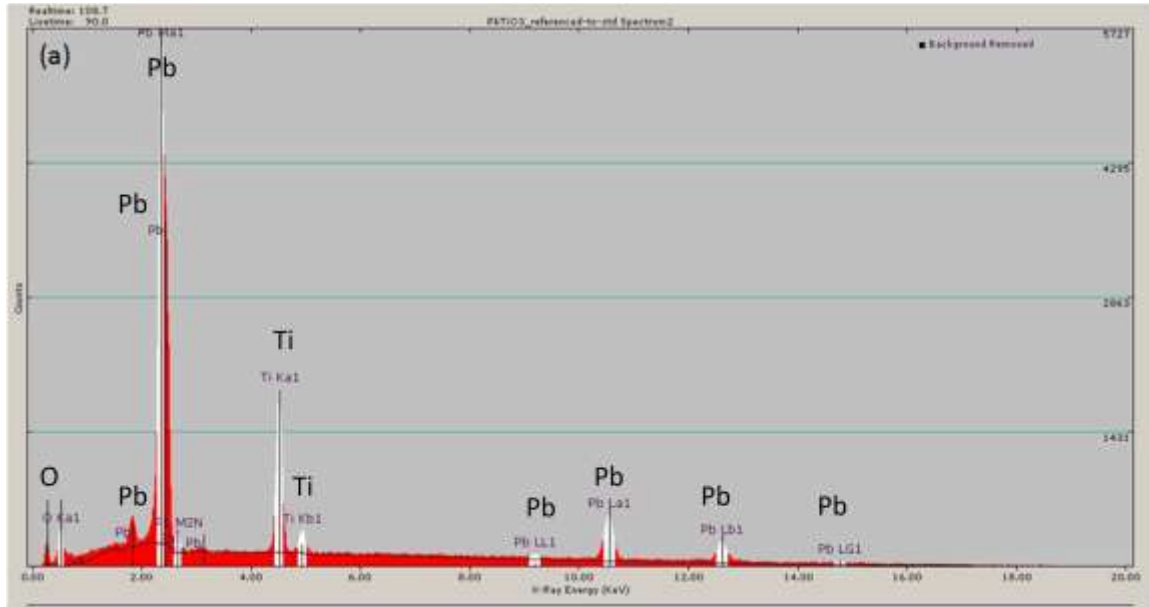
*David Arney, Tylan Watkins, and Paul A. Maggard**
Department of Chemistry, North Carolina State University Raleigh,
NC 27695-8204

Table 5.S1. Refined cell parameters^a for PbTiO₃, synthesized by the flux method.

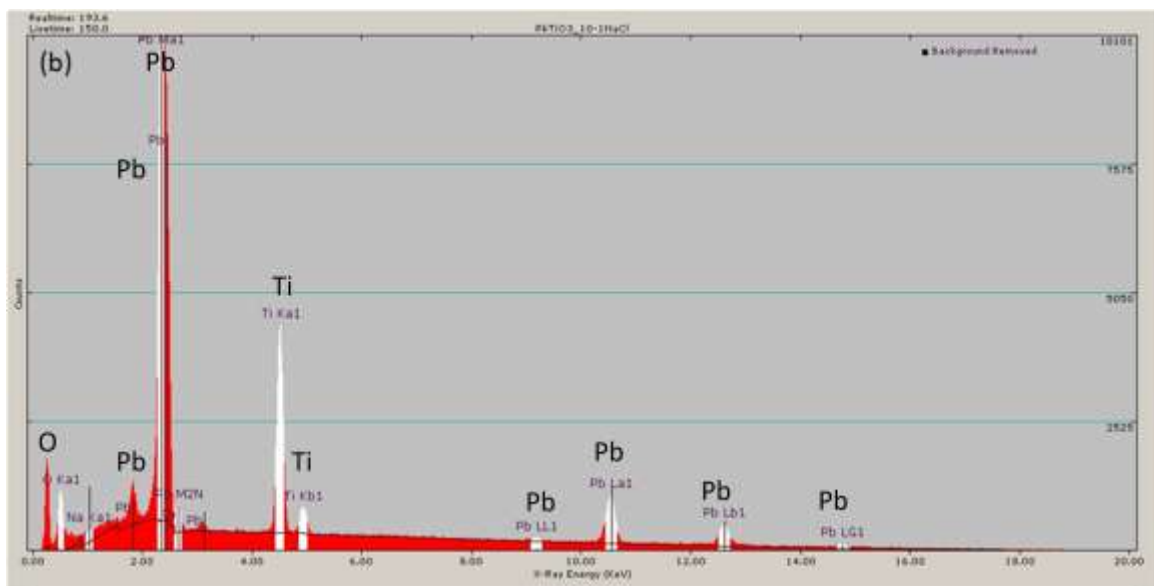
<u>Sample Name</u>	<u><i>a</i> (Å)</u>	<u><i>b</i> (Å)</u>	<u><i>c</i> (Å)</u>
PBO1	3.908(1)	3.908(1)	4.134(1)
PBO2	3.9051(9)	3.9051(9)	4.141(1)
PBO3	3.906(1)	3.906(1)	4.142(1)
PBO4	3.903(1)	3.903(1)	4.154(2)
PBO5	3.9018(8)	3.9018(8)	4.151(1)
PBO6	3.9041(9)	3.9041(9)	4.154(1)
PBO std.	3.904(1)	3.904(1)	4.152(1)

^a Unit cell parameters were refined using the program LATCON³⁰

Figure 5.S1. EDX Spectra showing the elemental composition of PbTiO_3 prepared using (a) solid state methods (PBO std.) and (b) 10:1 NaCl flux (PBO2).



Element	Weight %	Std. Dev.	MDL	Atomic %	k-ratio	Intensities	FWHM (eV)	ROI (net)
O	16.8	1.07	0.16	61.64	0.1496	2356.1	103.9	3202.56
Ti	15.69	0.81	0.91	19.23	0.1137	17760.1	142.5	19083.77
Pb	67.51	1.66	0.33	19.13	0.6299	48018.8	123.4	58008.12
Total	100							



Element	Weight %	Std. Dev.	MDL	Atomic %	k-ratio	Intensities	FWHM (eV)	ROI (net)
O	18.95	1.01	0.1	64.01	0.1795	6563.1	103.9	9454.69
Na?	0.84	0.31	0.88	1.99	0.0029	635.4	109.2	2509.54
Ti	15.1	0.75	0.56	17.03	0.1172	42490	142.5	45199.98
Pb	65.11	1.49	0.19	16.98	0.6463	114381.2	123.4	134462.53
Total	100							

? This element is statistically insignificant

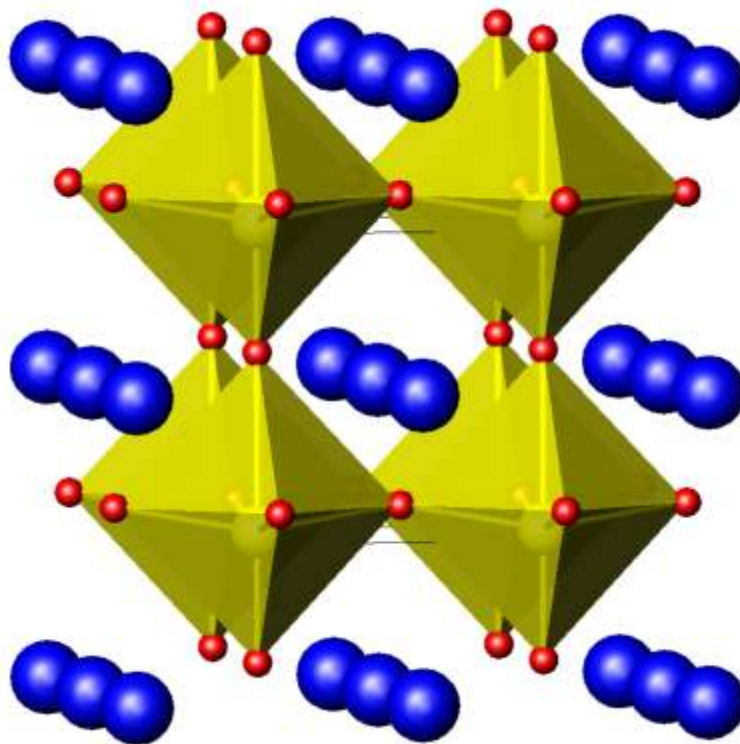


Figure 5.S2. Structure of PbTiO_3 , classic perovskite. TiO_6 octahedra are shaded in yellow, while Pb^{2+} ions fill the interstitial sites.

CHAPTER 6

Selective Pt Deposition and Photocatalysis of MLaNb₂O₇ (M=Rb, Ag) Prepared by Flux Synthesis and Ion-Exchange

A paper submitted to the *Journal of Energy and Environmental Science*

David Arney and Paul A. Maggard*

Department of Chemistry, North Carolina State University, Raleigh, NC 27695

Abstract

The ($n = 2$) layered Dion-Jacobsen phase perovskite AgLaNb₂O₇ was prepared from a AgNO₃ ion-exchange reaction using RbLaNb₂O₇. The RbLaNb₂O₇ was prepared from a RbCl flux with tunable RbCl:RbLaNb₂O₇ molar ratios from 1:1 – 10:1 and heating times ranging from 1h – 24h at a temperature of 1100°C. Grayish-colored powders were characterized by powder X-ray diffraction and the samples exhibited a bandgap size of 2.98 eV as determined from UV-vis diffuse reflectance measurements. Round-flat platelets with homogeneous microstructures were observed with sizes ranging from ~ 1.0 – 6.0 μm and thicknesses ~ 300 nm. Surface area measurements of the samples showed a range of 2.0 – 3.8 m² g⁻¹, with the highest surface area obtained for the AgLaNb₂O₇ sample prepared starting from a 5:1 RbCl:RbLaNb₂O₇ flux product. By comparison, the solid-state prepared samples exhibited no well-controlled particle sizes or microstructures. The photocatalytic activity for H₂ production was evaluated in aqueous methanol and yielded maximum rates of 2,102 μmol H₂·g⁻¹·h⁻¹ under UV irradiation and 20 μmol H₂·g⁻¹·h⁻¹ under visible irradiation for the AgLaNb₂O₇ sample prepared from a 1:1 RbCl:RbLaNb₂O₇ precursor. AgLaNb₂O₇ samples prepared from a solid-state precursor yielded maximum rates of 842 μmol H₂·g⁻¹·h⁻¹ and 20 μmol H₂·g⁻¹·h⁻¹ under UV and visible irradiation, respectively. These rates were

inversely correlated with particle surface area. The apparent quantum yield of the $\text{AgLaNb}_2\text{O}_7$ photocatalyst was $\sim 0.94\%$ at 350 nm. An FESEM study of the particle surface after photodeposited platinum islands were added to the bare $\text{AgLaNb}_2\text{O}_7$ particles revealed a large increase in 'active' surface area when compared to their $\text{RbLaNb}_2\text{O}_7$ counterparts, providing important insights into understanding the origins of photocatalysis in these metal oxide particles.

Keywords: Flux Synthesis; $\text{AgLaNb}_2\text{O}_7$; photocatalysis

Introduction

Development of new and efficient photocatalytic metal-oxide materials to convert solar energy into renewable fuels has recently become a rapidly expanding focus of research since the discovery of photocatalysis over an n-doped TiO_2 photoelectrode under ultraviolet light, first reported by Honda and Fujishima in 1972.¹⁻⁴ Among the numerous explored photocatalysts, layered materials have shown much promise in exhibiting some of the highest photocatalytic rates and quantum efficiencies for H_2 production from H_2O , including $\text{La}_2\text{Ti}_2\text{O}_7$, $\text{Sr}_2\text{Ta}_2\text{O}_7$, $\text{La}_4\text{CaTi}_5\text{O}_{16}$, $\text{HfCa}_2\text{Nb}_3\text{O}_{10}$, and $\text{Rb}_4\text{Nb}_6\text{O}_{17}$.⁵⁻¹³ Additionally, more recent efforts have been aimed towards utilizing the largest fraction of the solar spectrum in the development of efficient visible-light active photocatalysts for the overall splitting of water.¹⁴⁻¹⁶ It has been shown that Ag^+ -containing early transition-metal oxides can absorb light extending into visible wavelengths as a result of their higher energy valence bands that derives from filled Ag 4d orbitals, and which is still sufficiently below the $(\text{O}_2/\text{H}_2\text{O})$ oxidation potential.^{15,17-19} The targeted preparation of a layered photocatalytic metal oxide containing Ag^+ could potentially provide both the high quantum efficiencies and visible

light-absorption properties that are necessary for the next generation of photocatalysts. $\text{RbLaNb}_2\text{O}_7$ is an $n=2$ layered Dion-Jacobsen perovskite that is both a highly active UV photocatalyst and capable of undergoing low temperature ion-exchange with AgNO_3 to form $\text{AgLaNb}_2\text{O}_7$.²⁰⁻²⁵ This has motivated our research efforts to study its visible-light photocatalytic properties, and to the authors' best knowledge has not yet been examined. The synthesis of the $\text{RbLaNb}_2\text{O}_7$ analog has been reported only by high temperature solid-state methods, which provides little control over the particle sizes and surface features of the metal-oxide particle where the photon-initiated oxidation and reduction reactions occur (i.e. the active sites of the reaction).^{21,22} By contrast, utilization of molten-salt flux synthesis enables optimization of photocatalytic properties through greater control of particle sizes and morphologies. For example, the synthesis of $\text{La}_2\text{Ti}_2\text{O}_7$ particles using a $\text{Na}_2\text{SO}_4/\text{K}_2\text{SO}_4$ eutectic flux previously enabled smaller particle sizes in a reaction time of 1h, and that led to photocatalytic hydrogen evolution rates nearly two times greater than when prepared by solid-state techniques that involved multiple grindings and heatings and a reaction time of 50h.⁵ In addition to an ability to enable shorter reaction times and reduced reaction temperatures, investigations of the particle surface features and microstructures from the use of flux-synthesis have also helped probe a deeper understanding of the origins of photocatalytic activity on the surfaces of several bulk and layered metal-oxide catalysts.^{5,14,17,26-32} Thus, it is of considerable utility to investigate the incorporation of these methods in order to gain greater particle size control and investigate the photocatalytic activity of $\text{AgLaNb}_2\text{O}_7$.

Presented herein is an investigation of the flux synthesis and photocatalytic properties of $\text{AgLaNb}_2\text{O}_7$ prepared from a molten AgNO_3 ion-exchange reaction starting from $\text{RbLaNb}_2\text{O}_7$. The latter oxide was synthesized using a RbCl flux with independently tuned reaction times and flux-to-reactant ratios in order to examine the effects of varied particle size and morphologies. The particle sizes and shapes were not significantly affected during the ion-exchange reactions, thus retaining good control of the $\text{AgLaNb}_2\text{O}_7$ particle sizes and morphologies. The products were characterized by powder X-ray diffraction (PXRD), UV-Vis diffuse reflectance spectroscopy (DRS), BET surface area analysis, field emission scanning electron microscopy (FESEM), energy dispersive spectroscopy (EDS), and by measuring the ultraviolet and visible light photocatalytic activities for H_2 production from an aqueous methanol solution.

Experimental Details

2.1 Synthesis and Characterization

$\text{AgLaNb}_2\text{O}_7$ was prepared by a low temperature ion-exchange reaction using flux-prepared $\text{RbLaNb}_2\text{O}_7$ and AgNO_3 . The flux synthesis of $\text{RbLaNb}_2\text{O}_7$ was performed by combining a stoichiometric mixture of reagent-grade Rb_2CO_3 , (Alfa Aesar, 99%) La_2O_3 , (Alfa Aesar, 99.9%, preheated and dried at 900°C) and Nb_2O_5 (Alfa Aesar, 99.9985%) in a mortar and pestle and grinding well for 30 minutes prior to the addition of a RbCl (Alfa Aesar, 99.8%, M.P. = 718°C) flux in flux-to-reactant molar ratios of 1:1, 5:1, and 10:1. After grinding, the reactant mixtures were placed inside alumina crucibles and heated to 1100°C inside box furnaces with heating times of 1h, 6h, and 24h. The products were then allowed to radiatively cool to room temperature inside the box furnaces. The resulting powders were

then washed with hot DI water to remove the flux, and dried overnight at 80°C. The ion-exchange reaction was then carried out by mixing the ground RbLaNb₂O₇ powders with AgNO₃ in a 1:4 molar ratio (RbLaNb₂O₇:AgNO₃) and heating to 250°C in alumina crucibles inside a box furnace for 24h. Fine homogeneous grayish-colored powders of AgLaNb₂O₇ were obtained in high purity, as judged by powder X-ray diffraction patterns. AgLaNb₂O₇ was also prepared starting from a RbLaNb₂O₇ product made by solid-state techniques, which involved grinding, pelletizing, and heating a stoichiometric mixture of Rb₂CO₃ (20% excess for volatilization), La₂O₃ (preheated) and Nb₂O₅ at 1100°C for two days, according to the reported literature procedures.²¹

High-resolution Powder X-ray Diffraction (PXRD) data of all products were collected on an INEL diffractometer using CuK α_1 ($\lambda = 1.54056\text{\AA}$) radiation from a sealed-tube X-ray generator (35kV, 30mA) using a curved position sensitive detector (CPS120). Unit-cell parameters of the flux-prepared samples were calculated using the LATCON software program.³³ Field-emission scanning electron microscopy analyses were performed on a JEOL SEM 6400, and concomitantly the energy dispersive X-ray (EDX) spectra were taken as a check of the elemental compositions. UV-Vis diffuse reflectance spectra (DRS) were collected for all samples on a Shimadzu UV-3600 spectrophotometer equipped with an integrating sphere. BET surface area analyses were performed using a Quantachrome ChemBET Pulsar TPR/TPD.

2.2 Photocatalysis Testing

The photocatalytic activity of the AgLaNb₂O₇ products for H₂ formation was measured using an outer-irradiation type fused-silica reaction cell with a volume of 90 mL

and irradiated under both ultraviolet light ($\lambda > 230$ nm) and visible light ($\lambda > 400$ nm). First, each sample was loaded with a 1 wt% Pt cocatalyst using the well-known photochemical deposition method.³⁴ Numerous previous studies have shown that platinum islands on a metal oxide surface can function as a kinetic aid for the reduction of H^+ to give H_2 .³⁵ Typically, 200 mg of a $M\text{LaNb}_2\text{O}_7$ ($M = \text{Rb}, \text{Ag}$) sample was mixed with 30mL of an aqueous solution of dihydrogen hexachloroplatinate(IV) ($\text{H}_2\text{PtCl}_6 \cdot 6\text{H}_2\text{O}$; Alfa Aesar, 99.95%), and which was then irradiated for 2 h using a 400W Xe arc-lamp with constant stirring using a magnetic stir bar. A few mL of MeOH was added to each vessel prior to the reaction to aid in the Pt deposition. UV-Vis measurements of the remaining solution confirmed a complete deposition of the platinum cocatalyst. After platinization, the particles were separated via centrifugation, washed with deionized water to remove any remaining Cl^- ions, and then dried overnight in an oven at 80°C . For the photocatalytic H_2 measurements, 50 mg of the platinized $M\text{LaNb}_2\text{O}_7$ was then added to the fused-silica reaction vessel and filled with 20% aqueous methanol solution. The added methanol functions as a hole scavenger, thereby generating CO_2 from its photo-oxidation, and which allows the measurement of the H_2 formation rate alone without the typically more difficult concomitant formation of O_2 being necessary and potentially rate limiting.² The net balanced reaction is: $\text{CH}_3\text{OH} + \text{H}_2\text{O} \rightarrow 3 \text{H}_2 + \text{CO}_2$. The $M\text{LaNb}_2\text{O}_7$ particles were first stirred in the dark for ~ 20 – 30 min, in order to remove any trapped gases on the particles' surfaces. Next, the reaction cell was irradiated under constant stirring for 6 h using an external 1000 W Xe arc-lamp equipped with an IR water filter and cooled using an external fan. The outlet of the photoreaction vessel was connected to a small horizontal quartz tube that trapped the evolved

gases, and contained a moveable liquid bubble that allowed a volumetric determination of the amount of evolved gases at a constant pressure. The MLaNb_2O_7 samples exhibited the formation of copious amounts of gases that rose to the top of the reaction cell, and that was observed to be consistent with the movement of the liquid bubble. The progress of the photocatalytic reactions was marked every hour and used to calculate the amount of gases generated in $\mu\text{mol H}_2\cdot\text{g}^{-1}\cdot\text{h}^{-1}$. The trapped gases were manually injected into a gas chromatograph (SRI MG #2; helium ionization and thermal conductivity detectors) in order to confirm the generated gases as H_2 and CO_2 . The Apparent Quantum Yield (AQY) was measured using a reaction cell containing 50 mg of the suspended platinized catalyst and 75 mL of a 20% $\text{MeOH}_{(\text{aq})}$ solution irradiated using the 400W Xe Arc Lamp equipped with an IR filter and 350 nm bandpass filter (Newport Oriel).

$$\text{AQY (\%)} = \{[\text{number of reacted electrons}] / [\text{number of incident photons}]\} \times 100^{34,36}$$

The number of reacted electrons was determined from the volume of evolved H_2 . The number of incident photons was determined by ferrioxalate actinometry.³⁷

Results and Discussion

$\text{AgLaNb}_2\text{O}_7$ is a Dion-Jacobsen layered ($n=2$) perovskite crystallizing in the tetragonal crystal system with space group $I4_1/acd$. The variable n corresponds to the thickness of the perovskite layers, while the interlayer structure is composed of Ag and O atoms, shown in Figure 6.1. $\text{AgLaNb}_2\text{O}_7$ is a metastable phase that cannot be prepared directly in a single-step solid-state synthesis. It must be formed first from $\text{RbLaNb}_2\text{O}_7$ (space

group Imma) which has been prepared by both solid-state and flux-synthetic techniques. For the $\text{RbLaNb}_2\text{O}_7$ compound, RbCl was chosen as a flux. Using a common Rb cation impedes ion-competition during synthesis, has a relatively low melting point (718°C), and is easily removed with hot water after reaction. Pure-phase white-colored powders were formed in as little as 1h using a 10:1 $\text{RbCl}:\text{RbLaNb}_2\text{O}_7$ flux ratio. Attempts at using a lower reaction temperature resulted in the formation of RbNbO_3 impurities. The AgNO_3 ion-exchange reaction yielded homogeneous grayish powders that were washed with hot water to remove any remaining nitrate flux. Figure 6.2 shows the PXRD patterns of the $\text{AgLaNb}_2\text{O}_7$ products, and the inset shows PXRD patterns of the precursor $\text{RbLaNb}_2\text{O}_7$ phase. All of the samples were shown to be in high purity and good crystallinity, and no evidence of any remaining Ag metal, AgNO_3 or RbCl flux are present in the patterns. Refined lattice parameters of both $\text{AgLaNb}_2\text{O}_7$ and $\text{RbLaNb}_2\text{O}_7$ were calculated for all samples using the LATCON software program, they can be found in the supporting information.³³ EDX analyses were also performed on both compounds in order to confirm elemental compositions, and which are provided in the Supporting Information. The spectra revealed Rb, Ag, La, and Nb to be in their approximate stoichiometric molar ratios. There was no significant detection of any N or Cl, indicating the RbCl and AgNO_3 fluxes had been removed completely by the washing procedure.

FESEM was employed in order to evaluate the size and shape of the flux-prepared $\text{RbLaNb}_2\text{O}_7$ particles and the resultant ion-exchanged $\text{AgLaNb}_2\text{O}_7$ products. Figure 6.3 (a and b) shows FESEM images of the solid-state preparation of $\text{RbLaNb}_2\text{O}_7$ (6.3a) and after ion-exchange to form $\text{AgLaNb}_2\text{O}_7$ (6.3b) while Figures 6.3c and 6.3d show the 1:1 RbCl flux

prepared $\text{RbLaNb}_2\text{O}_7$ and its Ag-exchange analog, respectively. It should be noted that the overall shapes and sizes of the particles remain generally unchanged after the ion-exchange reactions, i.e. on going from $\text{RbLaNb}_2\text{O}_7$ to $\text{AgLaNb}_2\text{O}_7$. The solid-state preparation appeared largely to be aggregate clumps of the layered perovskite material with no well defined particle size or morphology, while the 1:1 RbCl flux samples revealed only slightly more individual and well-faceted platelet particles ranging in size from $\sim 1.0 - 3.5 \mu\text{m}$. As the flux-to-reactant ratio of $\text{RbCl}:\text{RbLaNb}_2\text{O}_7$ increased, the aggregate particles were not observed, and smooth flat platelets with fewer defects were quite well defined and larger in size, ranging from $\sim 1.0 - 6.0 \mu\text{m}$ and with plate thicknesses of $\sim 300 \text{ nm}$, as shown in Figures 6.4a and 6.4b. Nanostep edges of $\sim 20 - 100 \text{ nm}$ in height were also observed along the edges of the platelet particles, relative to the layered crystal growth of the particles. $\text{AgLaNb}_2\text{O}_7$ products prepared through ion-exchange from the 10:1 flux-prepared $\text{RbLaNb}_2\text{O}_7$ are shown in Figures 6.4c and 6.4d and do appear similar in both platelet size and thickness, as well as overall general morphology and shape.

The location of the deposited platinum cocatalyst plays a significant role in improving the photocatalytic activity of a metal-oxide catalyst. It is well known that a Pt salt will undergo a reduction to Pt^0 metal during the photodeposition reaction, and therefore will deposit at or near sites of higher electron density and higher reactivity.^{38,39} Observing where the largest amounts of platinum are being deposited could help reveal the most active surface sites of the particles at the metal oxide surface. Several FESEM images of $\text{RbLaNb}_2\text{O}_7$ and $\text{AgLaNb}_2\text{O}_7$ were taken after the photochemical deposition of a 5 wt. % platinum cocatalyst onto their surfaces. Typically, before a photocatalysis reaction, a 1 wt. % platinum cocatalyst

is deposited onto the particles' surfaces to enhance its overall photocatalytic performance. The deposition of 5 wt. % Pt cocatalyst achieves a greater number of platinum islands which are larger in size and are more clearly observable in the FESEM images. Figure 6.5 displays an EDX spot-analysis showing spectral images taken of both a platinum island (Spectrum 1) and a bare $\text{RbLaNb}_2\text{O}_7$ surface (Spectrum 2), and confirms the deposited nano-islands are platinum. For example, elemental composition of the region in spectrum 1 contains a significantly higher amount of platinum metal compared to the region scanned in spectrum 2. Large-area elemental composition EDX scans also confirmed complete platinum deposition onto the surface of the metal-oxide particles in the intended 5% amount, verifying complete deposition of platinum from the photodeposition procedure. FESEM images of the 10:1 RbCl flux-prepared $\text{RbLaNb}_2\text{O}_7$ particles after a 5% wt. platinum photochemical reduction are shown in Figure 6.6. Although small platinum islands are present over the entire surface of the platelet particles, the highest concentrations and largest islands were easily observed near and along edges, steps, and particle defects, and this trend was consistent for all $\text{RbLaNb}_2\text{O}_7$ particles. Figures 6.6(c and d) show a ring-pattern of deposited platinum islands along a surface edge of the particle where new layers of crystal growth have started. This strong preferential platinum deposition is also indicative of anisotropy regarding the electron migration pathway within the layered particle during photo-excitation. FESEM data from a 5 wt. % platinum deposition onto the surface of $\text{AgLaNb}_2\text{O}_7$ particles reveal contrasting images and can be seen in Figure 6.7. Platinum islands were observed along all surfaces of the particles, with no clear or defined preferential deposition locations, as was shown previously with $\text{RbLaNb}_2\text{O}_7$. This trend was consistent over all $\text{AgLaNb}_2\text{O}_7$ particle

surfaces. The ion-exchange reaction removed Rb^+ atoms between the perovskite layers and replaced them with Ag^+ atoms, and which resulted in the creation of a $\text{Ag } 4d^{10}$ filled band that enabled the absorption of visible light and Ag-to-Nb metal-to-metal charge transfer (MMCT) through an oxygen bridging ligand. Thus, the newly formed $\text{Ag } 4d$ valence band enabled electrons to now migrate orthogonally between the perovskite layers, thereby resulting in a greater number of platinum island deposits on all surfaces of the particle, and which was not previously observed in $\text{RbLaNb}_2\text{O}_7$. In regards to the active surface area of the layered photocatalyst, this potentially could have dramatic results in increasing its overall photocatalytic performance.

Measurements of the UV-Vis Diffuse Reflectance Spectra (DRS) were taken on flux-synthesized $\text{RbLaNb}_2\text{O}_7$ and $\text{AgLaNb}_2\text{O}_7$ samples in order to determine their optical bandgap sizes, and are shown in Figure 6.8. The reflectance has been converted to absorbance using the Kubelka-Munk function. The optical bandgap sizes were calculated from the onset of absorption using the well-known formula $E_g \text{ (eV)} = 1240 / \lambda_g \text{ (nm)}$, where $\lambda_g \text{ (nm)}$ is extrapolated from the linear rise in the absorption. $\text{RbLaNb}_2\text{O}_7$ has an optical bandgap of ~ 3.3 eV based on the onset of absorption, and is in good agreement with previous reports.^{20,25} The bandgap of $\text{AgLaNb}_2\text{O}_7$ was measured to be 2.98 eV based on the onset of absorption, indicating a red-shift of the band edge by approximately 0.3 eV caused by the newly incorporated $\text{Ag } 4d$ orbitals, and which is now capable of absorbing a small region of visible light.

To drive the photocatalytic water-splitting reaction, incident photons of energies greater or equal to the bandgap must excite electrons across the bandgap in a semiconductor

to create electron/hole pairs, which can then both oxidize and reduce water into O_2 and H_2 , respectively. In these experiments methanol was employed as a sacrificial reductant to observe the H_2 half reaction separately, without the more difficult water oxidation step. Shown in Figure 6.9 is the time course evolution of H_2 for the $AgLaNb_2O_7$ products under UV irradiation prepared from several $RbLaNb_2O_7$ samples, including by solid-state methods. The UV and visible-light (>400 nm) photocatalytic rates, along with surface area measurements of all $RbLaNb_2O_7$ and $AgLaNb_2O_7$ products are listed in Table 6.1. As a control experiment, an aqueous solution of 20% MeOH with no added catalyst yielded no production of H_2 under UV or visible light irradiation, thereby showing that all the H_2 gas produced in the reactions are from the activity of the $RbLaNb_2O_7$ and $AgLaNb_2O_7$ catalysts and not from any possible methanol photolysis. In general for the $RbLaNb_2O_7$ reactions, the rates of H_2 formation were greater with increasing amounts of flux used in their syntheses reactions, which causes a modest increase in surface area and smaller particle sizes. Activity was observed in all cases under UV irradiation. The highest observed rate of H_2 production in $RbLaNb_2O_7$ was $373 \mu\text{mol } H_2 \cdot \text{g}^{-1} \cdot \text{h}^{-1}$ for the 5:1 RbCl flux ratio heated for 24h ($RbLaNb_2O_7$ D) with a surface area of $1.9 \text{ m}^2 \text{ g}^{-1}$, while the lowest H_2 rate observed was $69 \mu\text{mol } H_2 \cdot \text{g}^{-1} \cdot \text{h}^{-1}$ for the 1:1 RbCl flux ratio heated for 6h ($RbLaNb_2O_7$ A) and had a surface area of $0.64 \text{ m}^2 \text{ g}^{-1}$. For comparison, the photocatalytic rate of H_2 production for the solid-state prepared sample ($RbLaNb_2O_7$ std.) was $274 \mu\text{mol } H_2 \cdot \text{g}^{-1} \cdot \text{h}^{-1}$ and was the second-highest rate observed for all $RbLaNb_2O_7$ samples and had a surface area of $1.2 \text{ m}^2 \text{ g}^{-1}$. As expected, $RbLaNb_2O_7$ was found to be inactive for visible-light photocatalysis, due to its large UV-bandgap size. For the $AgLaNb_2O_7$ photocatalytic reactions, all H_2 activities were first measured under UV-

irradiation and then tested under visible-light irradiation using a 400 nm cutoff filter. Under UV-irradiation, the $\text{AgLaNb}_2\text{O}_7$ samples outperformed their $\text{RbLaNb}_2\text{O}_7$ counterparts by a factor of at least three or greater in all cases. The overall rates of photocatalysis for the $\text{AgLaNb}_2\text{O}_7$ samples decreased with increasing surface area, in contrast with $\text{RbLaNb}_2\text{O}_7$. The highest observed UV rate was $2,102 \mu\text{mol H}_2 \cdot \text{g}^{-1} \cdot \text{h}^{-1}$ for $\text{AgLaNb}_2\text{O}_7$ (A), and had a surface area of $2.0 \text{ m}^2 \text{ g}^{-1}$. This rate was >30 times greater than its $\text{RbLaNb}_2\text{O}_7$ (A) counterpart. The lowest rate was $1,457 \mu\text{mol H}_2 \cdot \text{g}^{-1} \cdot \text{h}^{-1}$ for the $\text{AgLaNb}_2\text{O}_7$ (D) sample, and had a surface area of $3.8 \text{ m}^2 \text{ g}^{-1}$. The Apparent Quantum Yield was examined for the most active sample, $\text{AgLaNb}_2\text{O}_7$ (A), and was found to be 0.94% at 350 nm. The solid-state prepared $\text{AgLaNb}_2\text{O}_7$ std. sample exhibited the lowest activity across the $\text{AgLaNb}_2\text{O}_7$ samples and had a photocatalytic rate of $842 \mu\text{mol H}_2 \cdot \text{g}^{-1} \cdot \text{h}^{-1}$ and a surface area of $3.8 \text{ m}^2 \text{ g}^{-1}$. This was equal to the measured surface area of $\text{AgLaNb}_2\text{O}_7$ (D), yet showed a much lower rate of activity. This suggests that particle size and surface area are not the only factors that contribute to photocatalytic activity. This group has shown previously that particle shape and morphology, including exposed active sites, nanosteped microfeatures and defects also play a key role in determining the overall photocatalytic rate.^{5,14,17,26} It is likely that these contributing factors are also present in $\text{AgLaNb}_2\text{O}_7$. For the visible-light irradiation reactions, all $\text{AgLaNb}_2\text{O}_7$ samples were found to be active for H_2 production, although the rates were narrower in range and considerably lower in activity, as was expected given their absorption edge near 415nm. The highest recorded visible rate was $20 \mu\text{mol H}_2 \cdot \text{g}^{-1} \cdot \text{h}^{-1}$ for $\text{AgLaNb}_2\text{O}_7$ (A), and which also had the highest observed rate under UV irradiation. The solid-state prepared $\text{AgLaNb}_2\text{O}_7$ also obtained a rate of $20 \mu\text{mol H}_2 \cdot \text{g}^{-1} \cdot \text{h}^{-1}$ and the lowest observed

photocatalytic rate was approximately $2 \mu\text{mol H}_2 \cdot \text{g}^{-1} \cdot \text{h}^{-1}$ for $\text{AgLaNb}_2\text{O}_7$ (C). It is likely that with the small possible wavelength absorption range from the combination of the cutoff filter and the absorption band edge (400 – 415 nm), the rates of activity are going to be minimal as were seen in the data, and a clear correlation between particle surface area and photoactivity would be better suited for the higher rates observed in the UV photocatalytic H_2 data. From the FESEM images and the UV-Vis diffuse reflectance data, the two largest contributing factors to the increased activity observed in the ion-exchanged $\text{AgLaNb}_2\text{O}_7$ is a result of the inserted Ag 4d bands that shift the bandgap to allow a greater absorption of light, and the increased active surface area of the particles, as was observed from the FESEM images of the platinum photodeposition images. These results help to illustrate the utility of flux-synthesis techniques towards the optimization of photocatalytic activity in metal-oxides, as well as to demonstrate the advantages of using ion-exchange to visibly sensitize existing active UV photocatalysts.

Conclusions

The visibly-active layered photocatalyst $\text{AgLaNb}_2\text{O}_7$ can be prepared from an ion-exchange reaction with AgNO_3 and a $\text{RbLaNb}_2\text{O}_7$ precursor. The latter is synthesized using a RbCl flux, and yields high purities and homogeneous platelet microstructures that range in size from $\sim 1.0 - 6.0 \mu\text{m}$ and $\sim 300 \text{ nm}$ in thickness. Optical characterization revealed a bandgap size of 2.98 eV, and represented a red shift of $\sim 0.3 \text{ eV}$ from its $\text{RbLaNb}_2\text{O}_7$ precursor. Photocatalytic rates of H_2 production were observed in the range of $1,457 - 2,102 \mu\text{mol H}_2 \cdot \text{g}^{-1} \cdot \text{h}^{-1}$ under UV irradiation and $\sim 2 - 20 \mu\text{mol H}_2 \cdot \text{g}^{-1} \cdot \text{h}^{-1}$ under visible-light irradiation. The apparent quantum yield of $\text{AgLaNb}_2\text{O}_7$ was found to be 0.94% at 350 nm. Rates under UV irradiation showed an increase of up to >30 times greater activity than when

compared to their $\text{RbLaNb}_2\text{O}_7$ precursors. Higher rates were correlated with the reduced bandgap size from the inserted Ag 4d orbitals, and an increase in nanostep features and active surface area, as judged from platinum deposits onto the bare particle surface in FESEM images. By comparison, $\text{AgLaNb}_2\text{O}_7$ samples prepared from a solid state $\text{RbLaNb}_2\text{O}_7$ showed little well defined particle morphology and also exhibited a reduced photocatalytic activity of $842 \mu\text{mol H}_2 \cdot \text{g}^{-1} \cdot \text{h}^{-1}$. Thus, the results demonstrate the value of utilizing flux-synthesis techniques in tuning the particle sizes and surface microstructures in order to probe the origins of photocatalytic activity on the surfaces of metal-oxide particles.

Acknowledgements

Financial support of this research is acknowledged from the Chemical Sciences, Geosciences and Biosciences Division, Office of Basic Energy Sciences, Office of Science, U.S. Department of Energy (DE-FG02-07ER15914).

References

- (1) Fujishima, A.; Honda, K. *Nature* 1972, 238, 37.
- (2) Graetzel, M. E. *Energy Resources through Photochemistry and Catalysis*; Academic Press: New York, NY, 1983.
- (3) Domen, K.; Kondo, J.; Hara, M.; Takata, T. *Bull. Chem. Soc. Japan* 2000, 73, 1307.
- (4) Osterloh, F. E. *Chem. Mater.* 2008, 20, 35.
- (5) Arney, D., Porter, Brittany; Greve, Benjamin; Maggard, P.A. *J. Photochem. Photobiol., A*, 2008, 199, 230.
- (6) Hwang, D. W. *J. Catalysis* 2000, 193, 40.
- (7) Hwang, D. W.; Kim, G. H.; Jang, J. S.; Bae, S. W.; Ji, S. M.; Lee, J. S. *Catalysis today* 2004, 93, 845.
- (8) Hwang, D. W.; Kim, H. G.; Lee, J. S.; Kim, J.; Li, W.; Oh, S. H. *J. Phys. Chem. B* 2005, 109, 2093.
- (9) Hwang, D. W.; Lee, J. S.; Li, W.; Oh, S. H. *J. Phys. Chem. B* 2003, 107, 4963.
- (10) Kudo, A. *J. Phys. Chem. B* 2000, 104, 571.
- (11) Kato, H.; Kudo, A. *J. Photochem. Photobiol., A* 2001, 145, 129.
- (12) Hyun G. Kim, D. W. H., et. al *Chem. Comm.* 1999, 12, 1077.
- (13) Sayama, K.; Arakawa, H.; Domen, K. *Catal. Today* 1996, 28, 175.
- (14) Arney, D.; Watkins, T.; Maggard, P. A. *J. Am. Ceram. Soc.* 2011, 94, 1483.
- (15) Kudo, A.; Kato, H.; Tsuji, I. *Chem. Lett.* 2004, 33, 1534.
- (16) Maeda, K.; Teramura, K.; Lu, D.; Saito, N.; Inoue, Y.; Domen, K. *J. Phys. Chem. C* 2007, 111, 7554.

- (17) Arney, D., Hardy, Christopher; Greve, Benjamin; Maggard, Paul A. *J. Photochem. Photobiol. A*, 2010, *In Press*.
- (18) Kato, H.; Kobayashi, H.; Kudo, A. *J. Phys. Chem. B* 2002, *106*, 12441.
- (19) Konta, R.; Kato, H.; Kobayashi, H.; Kudo, A. *Phys. Chem. Chem. Phys* 2003, *5*, 3061.
- (20) Maeda, K.; Mallouk, T. E. *J. Mater. Chem.* 2009, *19*, 4813.
- (21) Gopalakrishnan, J.; Bhat, V.; Raveau, B. *Mater. Res. Bull.* 1987, *22*, 413.
- (22) Hermann, A. T.; Wiley, J. B. *Mater. Res. Bull.* 2009, *44*, 1046.
- (23) Sato, M.; Watanabe, J.; Uematsu, K. *J. Solid State Chem.* 1993, *107*, 460.
- (24) Porob, D. G.; Maggard, P. A. *Chem. Mater.* 2007, *19*, 970.
- (25) Domen, K.; Ebina, Y.; Sekine, T.; Tanaka, A.; Kondo, J.; Hirose, C. *Catal. Today* 1993, *16*, 479.
- (26) Joshi, U. A.; Palasyuk, A.; Arney, D.; Maggard, P. A. *J. Phys. Chem. Lett.* 2010, *1*, 2719.
- (27) Chiu, C.; Li, C.; Desu, S. B. *J. Am. Ceram. Soc.* 1991, *74*, 38.
- (28) Arendt, R. H. *J. Solid State Chem.* 1973, *8*, 339.
- (29) El-Toni, M. A.; Yin, S.; Sato, T. *Mater. Lett.* 2006, *60*, 185.
- (30) Kan, Y.; Jin, X.; Wang, P.; Li, Y.; Cheng, Y.-B.; Yan, D. *Mater. Res. Bull* 2003, *38*, 567.
- (31) Porob, D. G.; Maggard, P. A. *Mater. Res. Bull.* 2006, *41*, 1513.
- (32) Porob, D. G.; Maggard, P. A. *J. Solid State Chem.* 2006, *179*, 1727.
- (33) Schwarzenbach, D. *Acta Crystallogr., Sect. A: Found. Crystallogr.* 1989, *A45*, 63.

- (34) Kato, H.; Asakura, K.; Kudo, A. *J. Am. Chem. Soc.* 2003, *125*, 3082.
- (35) Nakamatsu, H.; Kawai, T.; Koreeda, A.; Kawai, S. *J. Chem. Soc., Faraday Trans. 1: Physical Chemistry in Condensed Phases* 1986, *82*, 527.
- (36) Kudo, A.; Miseki, Y. *Chem. Soc. Rev.* 2009, *38*, 253.
- (37) Hatchard, C. G.; Parker, C. A. *Proc. R. Soc. London, Ser. A* 1956, *235*, 518.
- (38) Kraeutler, B.; Bard, A. J. *J. Am. Chem. Soc.* 1978, *100*, 4317.
- (39) Ohtani, B.; Iwai, K.; Nishimoto, S.-i.; Sato, S. *J. Phys. Chem. B* 1997, *101*, 3349.

Table 6.1. Measured photocatalytic rates of H₂ formation for flux-prepared RbLaNb₂O₇ and AgLaNb₂O₇ under UV and visible light irradiation (>400 nm).

<u>Sample</u>	<u>RbCl:RbLaNb₂O₇</u> <u>Flux Ratio</u>	<u>Reaction</u> <u>Time (h)</u>	<u>Surface</u> <u>Area (m²/g)</u>	<u>UV</u> <u>Activity</u> <u>(μmol H₂/g-h)</u>	<u>Visible Activity</u> <u>(>400nm)</u> <u>(μmol H₂/g-h)</u>
RbLaNb ₂ O ₇ Std.	Solid State	50	1.2	274	-
AgLaNb ₂ O ₇ Std.	-	-	3.8	842	20
RbLaNb ₂ O ₇ A	1:1	6	0.64	69	-
AgLaNb ₂ O ₇ A	-	-	2.0	2102	20
RbLaNb ₂ O ₇ B	1:1	24	0.71	79	-
AgLaNb ₂ O ₇ B	-	-	2.3	1583	10
RbLaNb ₂ O ₇ C	5:1	6	3.9	111	-
AgLaNb ₂ O ₇ C	-	-	3.8	1528	~2
RbLaNb ₂ O ₇ D	5:1	24	1.9	373	-
AgLaNb ₂ O ₇ D	-	-	2.7	1806	~9
RbLaNb ₂ O ₇ E	10:1	1	3.9	112	-
AgLaNb ₂ O ₇ E	-	-	3.7	1457	15

Testing Conditions: Outer irradiation 1000 W high-pressure Xe arc-lamp, 50 mg of MLaNb₂O₇ (M = Rb, Ag), 20% MeOH_(aq) and 1 wt% Pt surface cocatalyst.

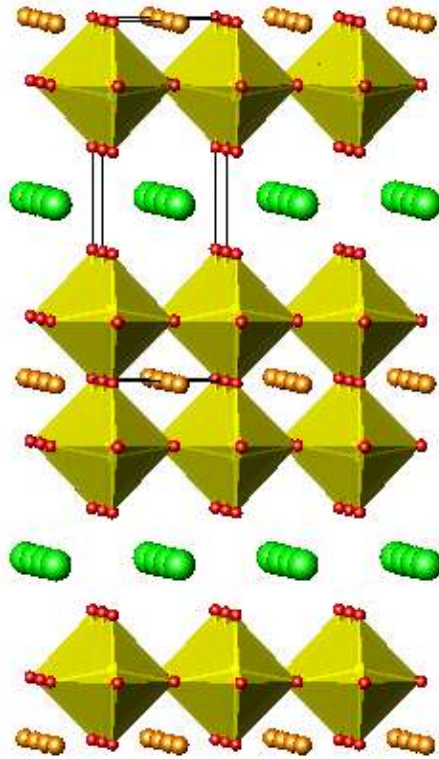


Figure 6.1. Structure of $\text{AgLaNb}_2\text{O}_7$ with outlined unit cell. NbO_6 octahedra are colored in yellow, La atoms are gold colored, and Ag atoms are green colored. Space Group $I4_1/acd$.

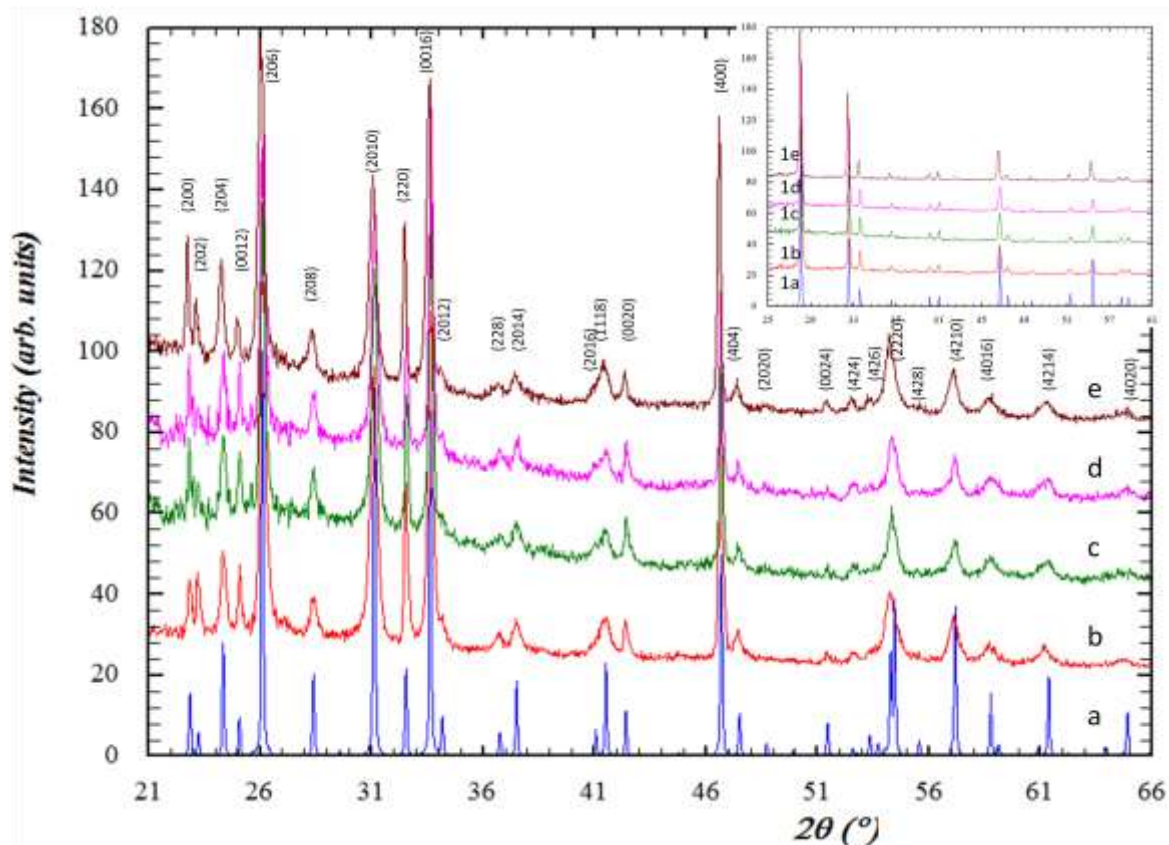


Figure 6.2. The powder X-ray diffraction (PXRD) patterns of the $\text{AgLaNb}_2\text{O}_7$ products. (a) calculated theoretical $\text{AgLaNb}_2\text{O}_7$ pattern, and $\text{AgLaNb}_2\text{O}_7$ patterns prepared from (b) solid state methods, (c) 1:1 RbCl flux heated for 6h, (d) 1:1 RbCl flux heated for 24h, (e) 10:1 RbCl Flux heated for 1h. Inset shows calculated $\text{RbLaNb}_2\text{O}_7$ patterns (1a) along with each corresponding prepared $\text{RbLaNb}_2\text{O}_7$ pattern (b) solid state methods, (c) 1:1 RbCl flux heated for 6h, (d) 1:1 RbCl flux heated for 24h, (e) 10:1 RbCl flux heated for 24h.

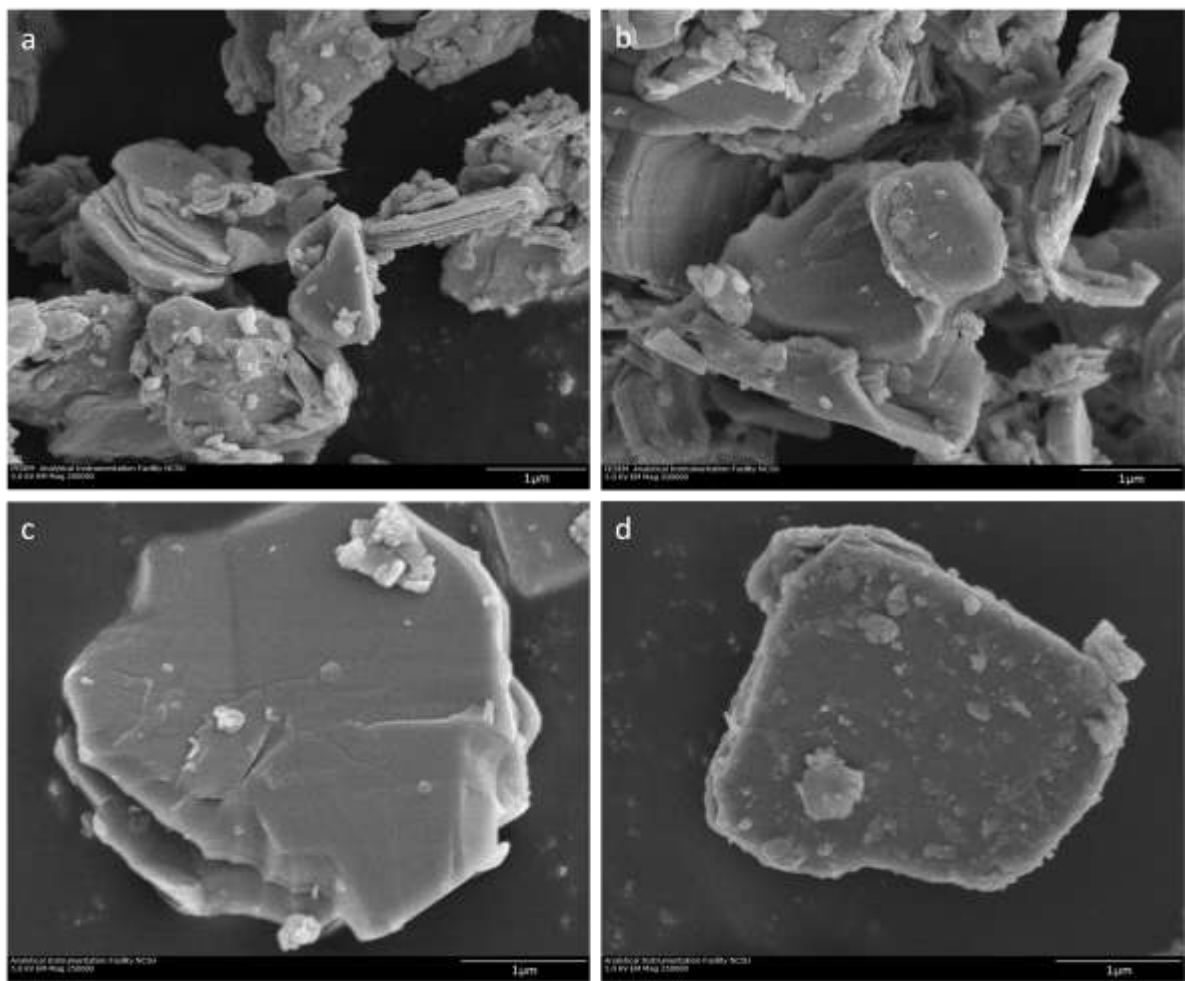


Figure 6.3. FESEM Images of (a) RbLaNb₂O₇ prepared from solid state methods and (b) AgLaNb₂O₇ after ion-exchange, and (c) RbLaNb₂O₇ prepared with a 1:1 RbCl flux and (d) AgLaNb₂O₇ after exchange (d).

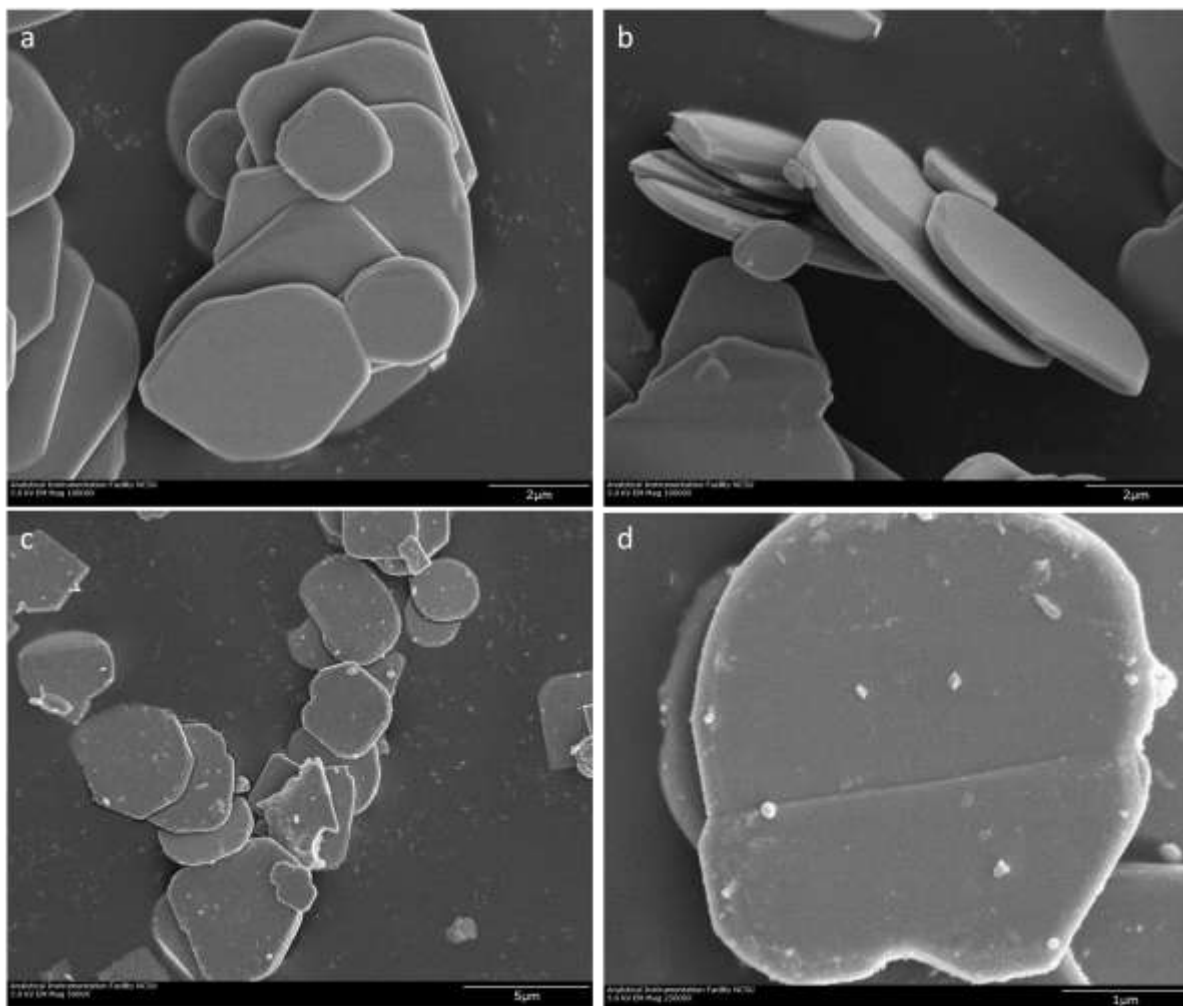


Figure 6.4. FESEM Images of (a and b) RbLaNb₂O₇ prepared using a 10:1 RbCl flux and (c and d) AgLaNb₂O₇ after the ion-exchange reaction.

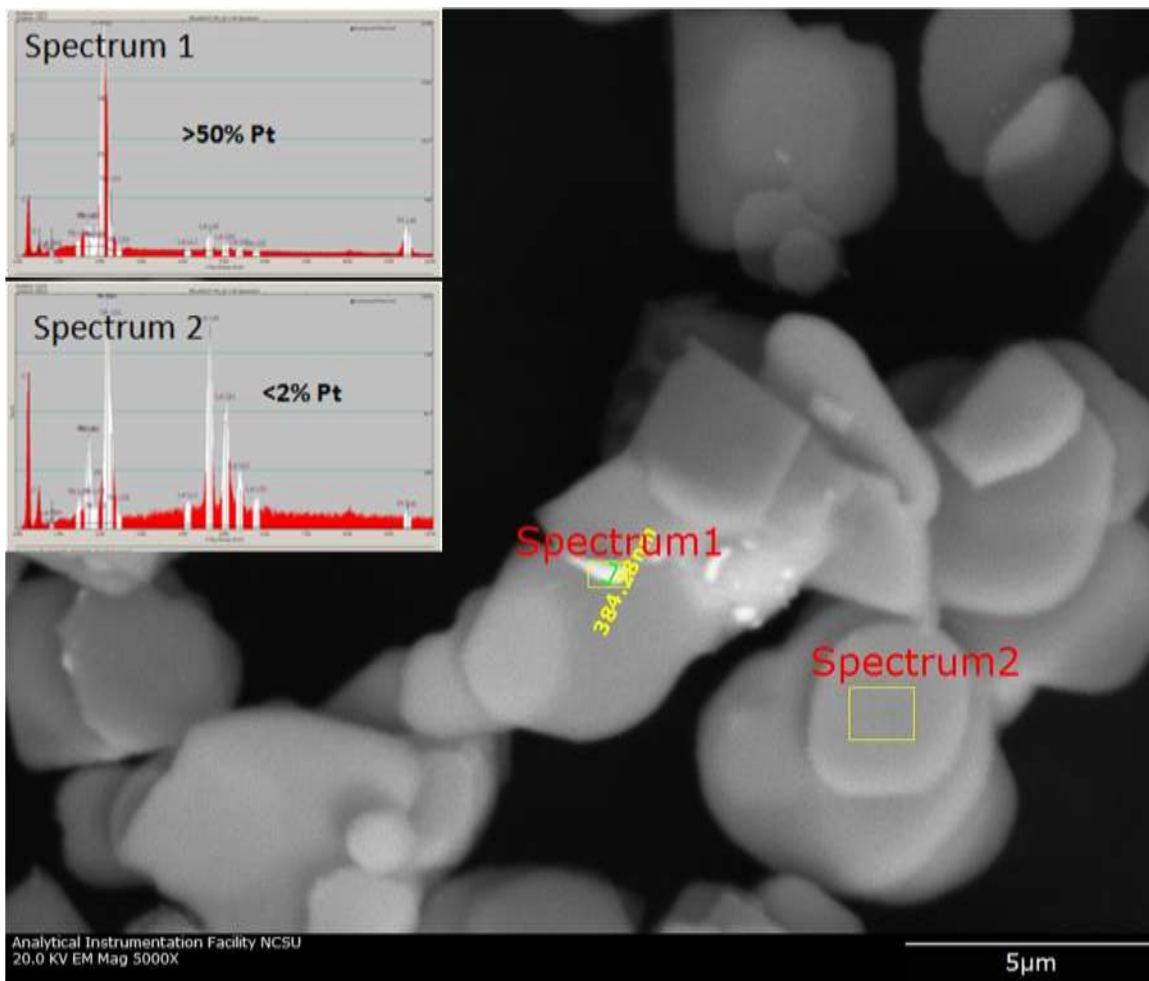


Figure 6.5. SEM Image and EDX spectra (Inset) showing elemental composition of platinum island (Spectrum 1) and bare $\text{RbLaNb}_2\text{O}_7$ surface (Spectrum 2).

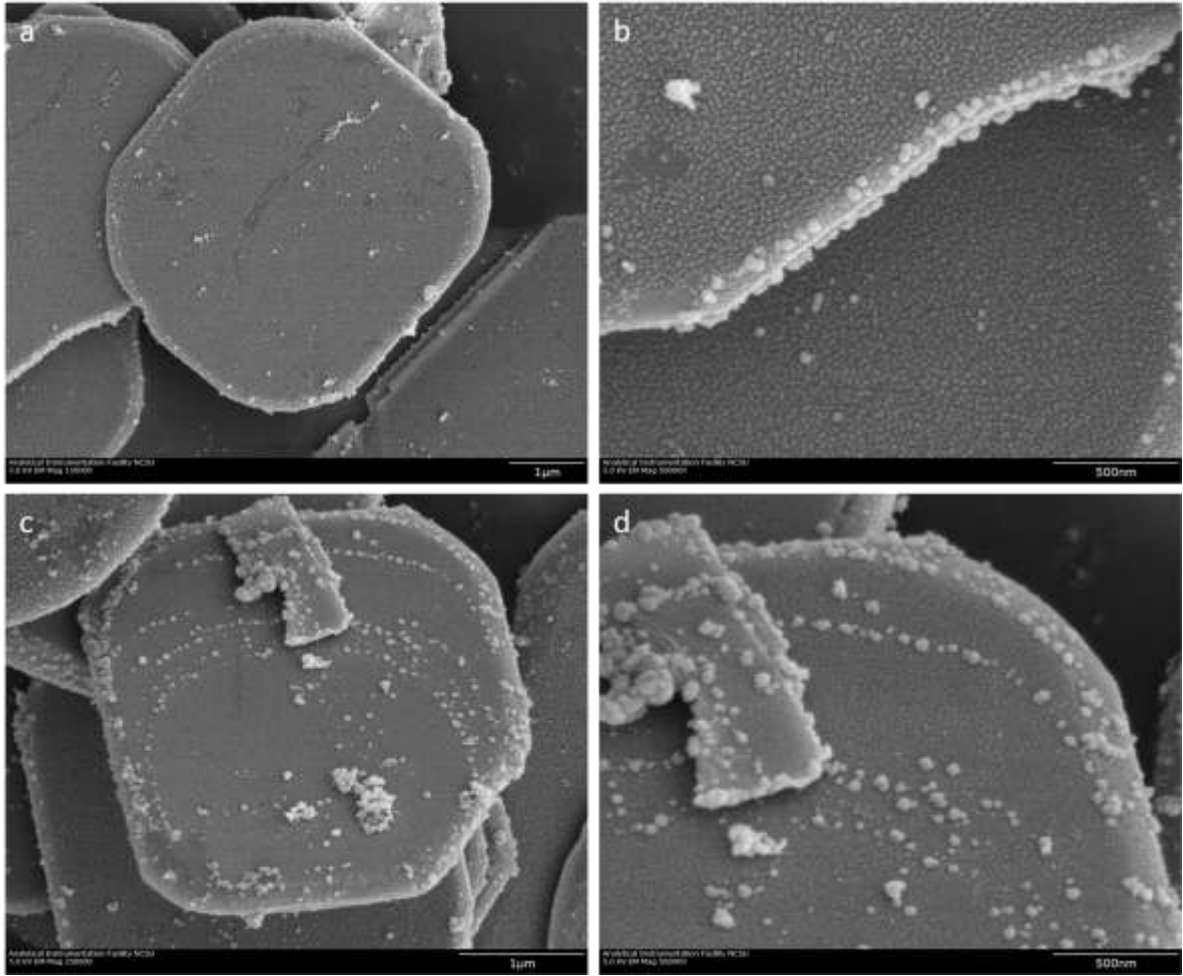


Figure 6.6. FESEM Images of a 5% wt. platinum photodeposition on the surface of flux-prepared $\text{RbLaNb}_2\text{O}_7$.

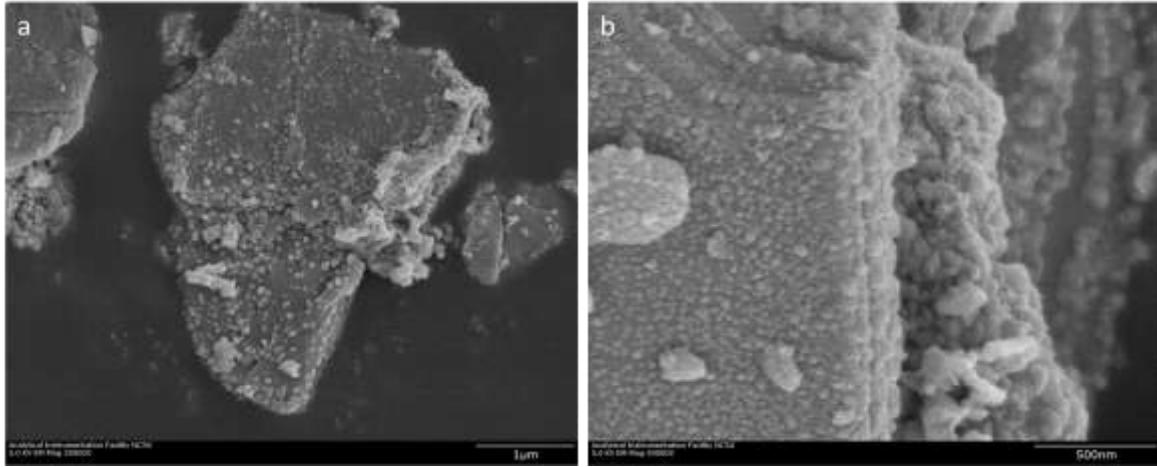


Figure 6.7. FESEM Images of a 5% wt. platinum photodeposition on the surface of flux-prepared $\text{AgLaNb}_2\text{O}_7$.

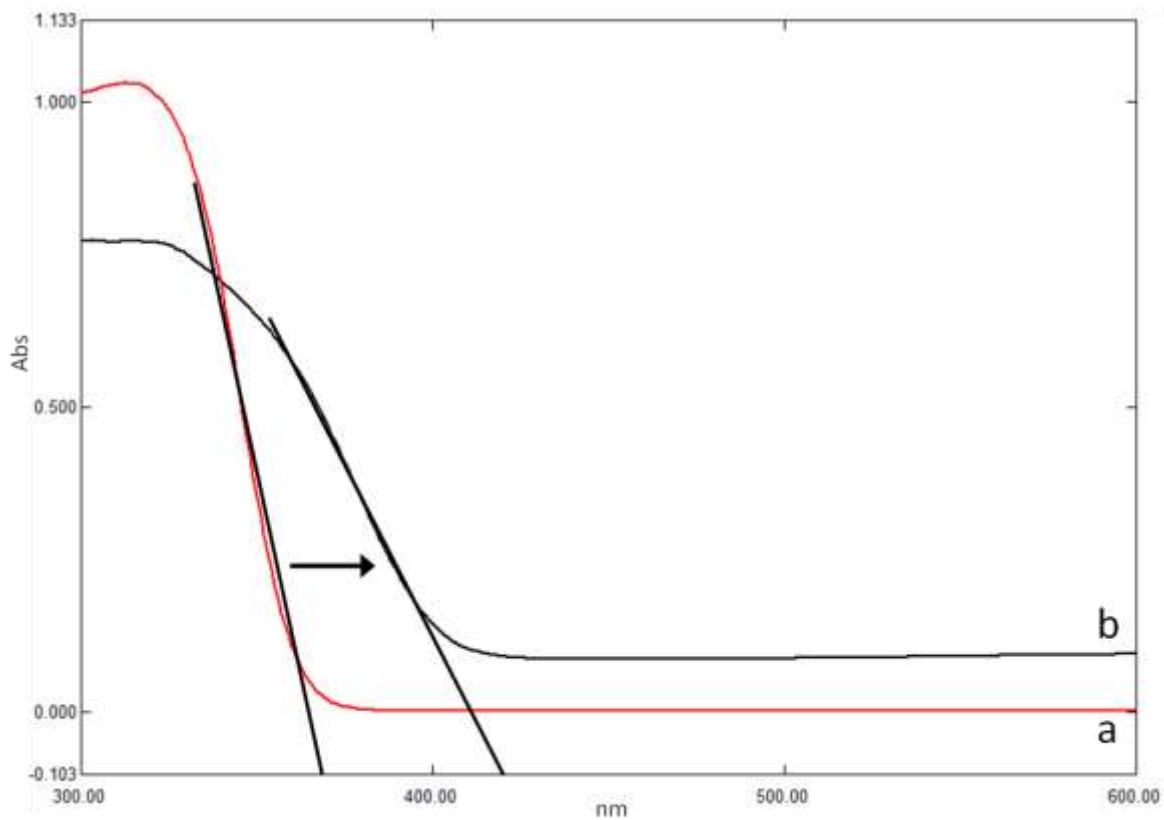


Figure 6.8. UV-Vis Diffuse Reflectance Spectra of (a) $\text{RbLaNb}_2\text{O}_7$ and (b) $\text{AgLaNb}_2\text{O}_7$ after the ion-exchange reaction. Reflectance has been converted to absorbance by the Kubelka-Munk method.

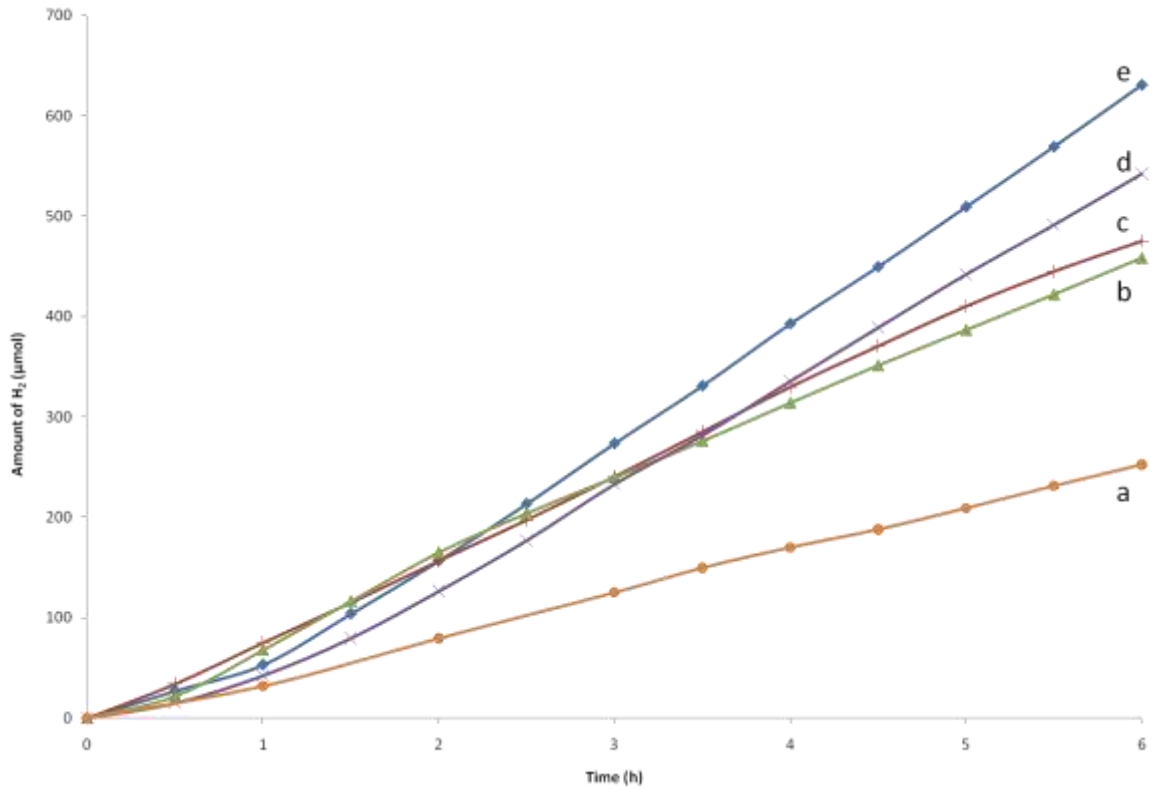


Figure 6.9. Photocatalytic formation of hydrogen versus time for AgLaNb₂O₇ prepared by (a) solid state methods, (b) 5:1 RbCl flux heated for 6h, (c) 1:1 RbCl flux heated for 24h, (d) 5:1 RbCl flux heated for 24h, (e) 1:1 RbCl flux heated for 6h.

Supporting Information

“Visible Photocatalytic Activity On Platinum Photodeposited AgLaNb₂O₇ Prepared by Flux Synthesis and Ion-Exchange”

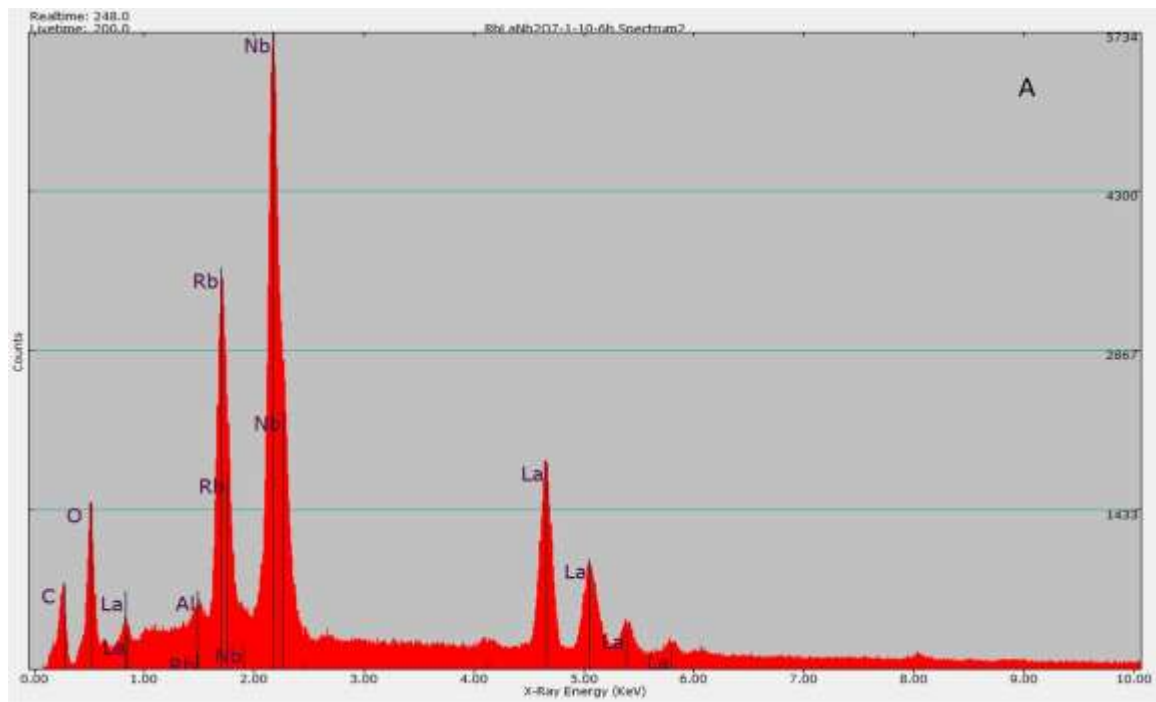
David Arney and Paul A. Maggard*

Table 6.S1. Refined cell parameters^a for RbLaNb₂O₇ and AgLaNb₂O₇ after ion-exchange.

<u>Sample Name</u>	<u><i>a</i> (Å)</u>	<u><i>b</i> (Å)</u>	<u><i>c</i> (Å)</u>
RbLaNb ₂ O ₇ Std.	5.4785(8)	22.4261(2)	5.1576(3)
RbLaNb ₂ O ₇ A	5.4763(8)	22.4042(2)	5.1602(3)
RbLaNb ₂ O ₇ B	5.4748(8)	22.4061(3)	5.1543(4)
RbLaNb ₂ O ₇ C	5.4946(9)	22.4385(3)	5.1788(4)
RbLaNb ₂ O ₇ D	5.4775(9)	22.4077(3)	5.1595(4)
RbLaNb ₂ O ₇ E	5.4801(8)	22.4076(3)	5.1591(4)
AgLaNb ₂ O ₇ Std.	7.7778(7)	7.7778(7)	42.5447(1)
AgLaNb ₂ O ₇ A	7.7803(2)	7.7803(2)	42.5692(4)
AgLaNb ₂ O ₇ B	7.7801(3)	7.7801(3)	42.5687(5)
AgLaNb ₂ O ₇ C	7.7923(4)	7.7923(4)	42.7652(6)
AgLaNb ₂ O ₇ E	7.7924(5)	7.7924(5)	42.7218(8)

^a Unit cell parameters were refined using the program LATCON³⁴

Figure 6.S1. EDX Spectra showing the elemental composition of flux-prepared RbLaNb₂O₇.



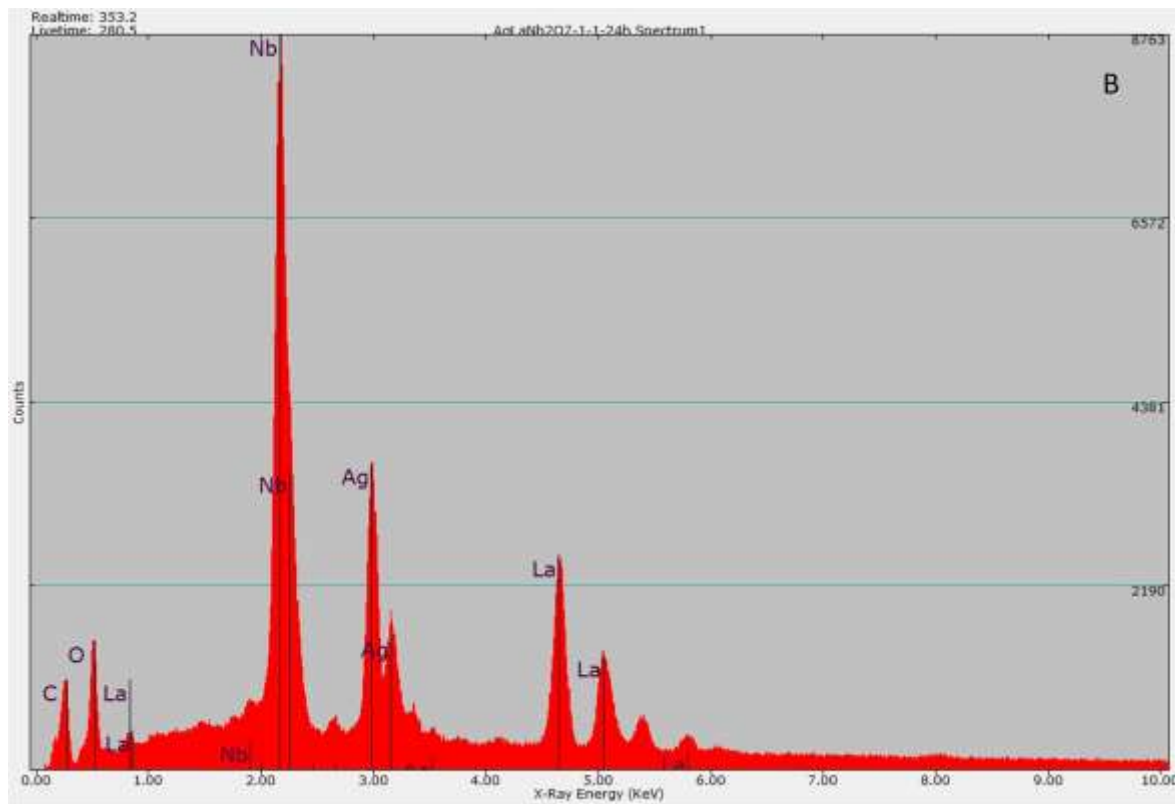
Quantitative Results for RbLaNb₂O₇ Spectrum 1

Analysis: Bulk Method: Standardless

Acquired 08-Mar-2011, 20.0 KeV @10 eV/channel

Element	Weight %	Std. Dev.	Atomic %	FWHM (eV)	ROI (net)
Oxygen	12.6	0.76	47.24	103.9	7063.71
Rubidium	21.89	0.97	15.35	116.9	26600.58
Niobium	42.75	1.04	27.59	121.5	52287.62
Lanthanum	22.76	1.02	9.82	143.7	22058.64
Total	100				

Figure 6.S2. EDX Spectra showing the elemental composition of flux-prepared $\text{AgLaNb}_2\text{O}_7$.



Quantitative Results for $\text{AgLaNb}_2\text{O}_7$ Spectrum2

Analysis: Bulk Method: Standardless
 Acquired 09-Mar-2011, 20.0 KeV @ 10
 eV/channel

Element	Weight %	Std. Dev.	Atomic %	FWHM (eV)	ROI (net)
Niobium	49.79	1.21	56.45	121.5	56371.22
Silver	25.08	1.05	24.49	129.1	23247.57
Lanthanum	25.13	1.09	19.06	143.7	17193.62
Total	100				

CHAPTER 7

CONCLUSIONS

Developing photocatalytic metal-oxides for the generation of hydrogen from solar energy and water is a rapidly expanding field for renewable energy research.¹⁻⁴ Incident photons of energy equal to the bandgap size or greater can excite electrons from the valence band to the conduction band and catalytically drive the (H₂O/H₂) and (O₂/H₂O) redox reactions at the metal-oxide's surface. Common examples include TiO₂ and NaTaO₃, which are among the most extensively studied photocatalysts to date.⁵⁻⁷ However, these metal-oxides have been limited in their ability to absorb light only at ultraviolet wavelengths, and which comprise a narrow region of the entire solar spectrum. Incorporation of metals such as Ag⁺ and Pb²⁺ into these metal-oxides has been shown to reduce the overall bandgap by typically 0.3 – 0.5 eV and allow absorption of light into the visible region. This is because the introduction of filled Ag d¹⁰ and Pb s² valence orbitals that raises the valence band to higher energy levels. A few investigated examples are AgTaO₃, AgNbO₃, and PbTiO₃.⁸⁻¹¹ These metal-oxides were shown to have reduced bandgaps as compared to their UV-active metal-oxide counterparts (NaTaO₃, TiO₂), and in the case of AgNbO₃ and PbTiO₃, to photocatalytically produce H₂ in a methanol solution under visible light.

Further, the syntheses of photocatalyst metal-oxides have been generally limited to traditional solid-state methods, and therefore lack control of particle sizes and shapes that can potentially influence the overall rates of the water-splitting reactions. The use of a flux, or molten-salt, during the synthesis reaction has been shown to enable shorter reaction times, reduced reaction temperatures, and maintain better of control particle sizes and

morphologies. These investigations have been primarily focused on using such techniques towards the optimization of photocatalytic activity of several metal-oxide photocatalysts. For example, the use of flux-synthesis in $\text{La}_2\text{Ti}_2\text{O}_7$ demonstrated that photocatalytic rates could be doubled as compared to their solid-state prepared counterparts as a result of higher surface areas and more exposed particle edges, and where it is believed that the water-splitting photoreaction takes place.¹² Additionally, a flux can be used for preparing metal-oxides that are otherwise quite difficult or not possible to synthesize by solid-state methods, as was the case for $\text{Na}_2\text{Ca}_2\text{Nb}_4\text{O}_{13}$, which was shown to be a highly-active layered UV photocatalyst. By varying the type of flux used during synthesis, contrasting particle morphologies can be obtained that also affect the photocatalytic activity. SEM analysis of $\text{Na}_2\text{Ca}_2\text{Nb}_4\text{O}_{13}$ particles revealed flat platelet structures when prepared using a Na_2SO_4 flux, and thin aggregate rods when prepared using a NaCl flux, the latter having higher surface areas and photocatalytic activities of nearly four times greater than their platelet-structured counterparts. Variation of particle morphologies using different fluxes was further demonstrated during the investigation of PbTiO_3 , where small round spherical particles were observed from a NaCl flux, and larger cubic-shaped particles were observed from an excess PbO flux.¹⁰ Interestingly, the larger cubic particles with lower surface areas yielded higher photocatalytic rates, owing to the presence of nanostep features, defects, and edges that contribute to the higher rates. These results reveal a strong starting point in incorporating alternative synthetic methods such as a molten flux in the preparation of metal-oxide photocatalysts.

A 'rational design' approach to visible-light sensitization of metal-oxides was further investigated using the ion-exchangeable layered perovskite $\text{RbLaNb}_2\text{O}_7$. Previous research

showed promising bandgap-tuning capabilities by replacing the Rb^+ atoms in $\text{RbLaTa}_2\text{O}_7$ with $[\text{CuCl}]^+$ layers that caused a red shift in the bandgap size owing to the presence of Cu^{2+} atoms.¹³ This work was expanded upon by exchanging the interlayer Rb atoms with Ag^+ in a molten AgNO_3 flux and investigating its visible-light photocatalytic properties. The exchange reaction reduced the overall bandgap size by ~ 0.3 eV, and enabled visible-light absorption. The investigation of particle size control by flux synthesis was concomitantly studied through the RbCl flux preparation of $\text{RbLaNb}_2\text{O}_7$, and which revealed contrastingly different particle sizes and features as the reactions were performed by both solid-state methods and with increasing amounts of flux used during synthesis. The photocatalytic activities of the $\text{AgLaNb}_2\text{O}_7$ and its Rb analog revealed not only that overall H_2 activity increased after the ion-exchange, but that the activities from the flux methods outperformed their solid-state counterparts in all $\text{AgLaNb}_2\text{O}_7$ cases.

The deposition of a platinum cocatalyst onto the surface of a metal-oxide photocatalyst plays a key role in improving the overall photocatalytic production of H_2 . The effects of differing platinum deposition methods were investigated in $\text{Na}_2\text{Ca}_2\text{Nb}_4\text{O}_{13}$. Both the photochemical deposition (PCD) and the incipient wetness impregnation (IWI) methods were employed, and then their rates of activities were compared. In all cases, the PCD method outperformed its IWI method counterparts by $\sim 30\%$. Microscopy data revealed preferential deposition of platinum onto edges, steps, and defects from the PCD method, but no preferred deposition from the IWI method. The increased activity was suggested to have been because of an increased presence of platinum in areas of higher electron concentration. The investigation of electron migration pathways within layered perovskite photocatalysts

was further investigated in ALaM_2O_7 ($A = \text{Rb}, \text{Ag}$), and again through a platinum cocatalyst deposition study. SEM images of platinized $\text{RbLaNb}_2\text{O}_7$ sample revealed preferential deposition along edges, steps, and grooves that indicated areas of greater electron concentration. This phenomenon suggested that the electron migration pathways within the particles were anisotropic and were generally confined to within their own perovskite layers. Upon Ag-exchange, though, platinum deposition was observed on all surfaces of the particle, suggesting that the creation of a Ag d^{10} filled band enabled Ag-to-Nb metal-to-metal charge transfer (MMCT) through an oxygen bridging ligand, and electrons could now migrate orthogonally between the perovskite layers. The dramatic increase in photocatalytic activity, which was up to nearly 30 times greater than the $\text{RbLaNb}_2\text{O}_7$ analogs, suggested an increase in overall ‘active’ surface area, i.e., an increase of surface sites that promoted catalytic reduction of H_2O . The results from this investigation support a successful, yet simple method for visible-light sensitization using already existing layered ion-exchangeable photocatalysts.

There are several factors that must be considered for the development of an efficient photocatalyst. This work has probed the effects of particle shape and morphology on their photocatalytic activity, the use of a d^0/d^{10} band strategy to enable visible absorption of light while still maintaining the appropriate energy positions to allow for the splitting of water, and a study of the migration of charge carriers to active sites through platinum deposition studies. Other factors include efficient separation of charge carriers to prevent recombination centers (a significant problem among d^0/d^9 metal photocatalysts), long term catalytic stability and high turnover rates, and interfacial electron transfer.⁶ It is expected that new visible-light

photocatalysts will be able to meet such requirements, although new materials that meet all of these fundamental needs are currently unknown. Several other materials have recently been discovered and shown to be capable of undergoing visible-light photocatalytic activity, and a few examples are listed in Table 7.1. For the challenge of discovering even more efficient photocatalysts, the use of metal-oxides containing Ag^+ and Pb^{2+} , as well as others such as Sn^{2+} , Sb^{2+} , and Cu^{1+} , that are relatively unknown as water splitting photocatalysts, should be employed. Currently, research towards new Cu^+ -containing photocatalytic metal-oxides is underway in this group, and the use of ion-exchangeable materials to incorporate Cu^+ into their structures and reduce the overall bandgap size should be the focus of much more future research.¹⁴⁻¹⁶

References

- (1) Domen, K.; Kondo, J.; Hara, M.; Takata, T. *Bull. Chem. Soc. Japan* **2000**, *73*, 1307.
- (2) Domen, K.; Hara, M.; Kondo, J.; Takata, T.; Kudo, A.; Kobayashi, H.; Inoue, Y. *Korean J. Chem. Eng.* **2001**, *18*, 862.
- (3) Kato, H. *Catalysis today* **2003**, *78*, 561.
- (4) Graetzel, M. E. *Energy Resources through Photochemistry and Catalysis*; Academic Press: New York, NY, 1983.
- (5) Fujishima, A.; Honda, K. *Nature* **1972**, *238*, 37.
- (6) Kato, H.; Asakura, K.; Kudo, A. *J. Am. Chem. Soc.* **2003**, *125*, 3082.
- (7) Porob, D. G.; Maggard, P. A. *J. Solid State Chem.* **2006**, *179*, 1727.
- (8) Kato, H.; Kobayashi, H.; Kudo, A. *J. Phys. Chem. B* **2002**, *106*, 12441.
- (9) Arney, D., Hardy, Christopher; Greve, Benjamin; Maggard, Paul A. *J. Photochem. Photobiol.. A, Chem.* **2010**, *214*, 54-60.
- (10) Arney, D.; Watkins, T.; Maggard, P. A. *J. Am. Ceram. Soc.* **2011**, *94*, 1483.
- (11) Kim, H. G.; Becker, O. S.; Jang, J. S.; Ji, S. M.; Borse, P. H.; Lee, J. S. *J. Solid State Chem.* **2006**, *179*, 1214.
- (12) Arney, D., Porter, Brittany; Greve, Benjamin; Maggard, P.A. *J. Photochem. Photobiol.. A, Chem.* **2008**, *199*, 230.
- (13) Porob, D. G.; Maggard, P. A. *Chem. Mater.* **2007**, *19*, 970.
- (14) Joshi, U. A.; Palasyuk, A.; Arney, D.; Maggard, P. A. *J. Phys. Chem. Lett.* **2010**, *1*, 2719.

- (15) Palasyuk, O.; Palasyuk, A.; Maggard, P. A. *Inorg. Chem. (Washington, DC, U. S.)* **2010**, *49*, 10571.
- (16) Palasyuk, O.; Palasyuk, A.; Maggard, P. A. *J. Solid State Chem.* **2010**, *183*, 814.
- (17) Kudo, A.; Miseki, Y. *Chem. Soc. Rev.* **2009**, *38*, 253.
- (18) Wang, D.; Tang, J.; Zou, Z.; Ye, J. *Chem. Mater.* **2005**, *17*, 5177.
- (19) Shimodaira, Y.; Kato, H.; Kobayashi, H.; Kudo, A. *Bull. Chem. Soc. Jpn.* **2007**, *80*, 885.
- (20) Yoshimura, J.; Ebina, Y.; Kondo, J.; Domen, K.; Tanaka, A. *J. Phys. Chem.* **1993**, *97*, 1970.
- (21) Kim, H. G.; Hwang, D. W.; Lee, J. S. *J. Am. Chem. Soc.* **2004**, *126*, 8912.
- (22) Liu, H.; Nakamura, R.; Nakato, Y. *ChemPhysChem* **2005**, *6*, 2499.
- (23) Hosogi, Y.; Tanabe, K.; Kato, H.; Kobayashi, H.; Kudo, A. *Chem. Lett.* **2004**, *33*, 28.
- (24) Hosogi, Y.; Kato, H.; Kudo, A. *Chem. Lett.* **2006**, *35*, 578.
- (25) Hosogi, Y.; Kato, H.; Kudo, A. *J. Mater. Chem.* **2008**, *18*, 647.

Table 7.1. Visibly-active metal oxide photocatalysts for H₂ or O₂ evolution in the presence of sacrificial reagents under visible-light irradiation. Adapted from reference 17.

<u>Photocatalyst</u>	<u>Bandgap (eV)</u>	<u>μmol H₂ h⁻¹</u>	<u>μmol O₂ h⁻¹</u>	<u>Reference</u>
WO ₃	2.8	-	65	4
Zn ₃ V ₂ O ₈	2.92	-	10.2	18
PbMoO ₄ :Cr	2.26	-	71.5	19
RbPb ₂ Nb ₂ O ₉	2.5	4	1.1	20
PbBi ₂ Nb ₂ O ₉	2.88	3.2	520	21
PbTiO ₃	2.75	27.4	183	10
BiCu ₂ VO ₆	2.1	-	2.3	22
SnNb ₂ O ₆	2.3	14.4	62.8	23,24
AgNbO ₃	2.86	5.9	37	8,9
AgLi _{1/3} Sn _{2/3} O ₂	2.7	-	53	25